NON-ISOTHERMAL LASER TREATMENT OF Fe-Si-B METALLIC GLASS

Sameehan Shrikant Joshi, B.Tech., M.Sc. (Engg.)

Dissertation Prepared for the Degree of

DOCTOR OF PHILOSOPHY

UNIVERSITY OF NORTH TEXAS

December 2017

APPROVED:

Narendra B. Dahotre, Major Professor
Rajarshi Banerjee, Committee Member
Jincheng Du, Committee Member
Sundeep Mukherjee, Committee Member
Marcus L. Young, Committee Member
Andrey A. Voevodin, Chair of the Department of
Materials Science and Engineering
Costas Tsatsoulis, Dean of the
College of Engineering
Victor Prybutok, Dean of the
Toulouse Graduate School

Joshi, Sameehan Shrikant. *Non-Isothermal Laser Treatment of Fe-Si-B Metallic Glass.* Doctor of Philosophy (Materials Science and Engineering), December 2017, 112 pp., 8 tables, 46 figures, 176 numbered references.

Metallic glasses possess attractive properties, such as high strength, good corrosion resistance, and superior soft magnetic performance. They also serve as precursors for synthesizing nanocrystalline materials. In addition, a new class of composites having crystalline phases embedded in amorphous matrix is evolving based on selective crystallization of metallic glasses. Therefore, crystallization of metallic glasses and its effects on properties has been a subject of interest. Previous investigations from our research group related to laser assisted crystallization of Fe-Si-B metallic glass (an excellent soft magnetic material by itself) showed a further improvement in soft magnetic performance. However, a fundamental understanding of crystallization and mechanical performance of laser treated metallic glass was essential from application point of view. In light of this, the current work employed an integrated experimental and computational approach to understand crystallization and its effects on tensile behavior of laser treated Fe-Si-B metallic glass. The time temperature cycles during laser treatments were predicted using a finite element thermal model. Structural changes in laser treated Fe-Si-B metallic glass including crystallization and phase evolution were investigated with the aid of X-ray diffraction, differential scanning calorimetry, resistivity measurements, and transmission electron microscopy. The mechanical behavior was evaluated by uniaxial tensile tests with an Instron$^{\text{TM}}$ universal testing machine. Fracture surfaces of the metallic glass were observed using scanning electron microscopy and site specific transmission electron microscopy.

Fe-Si-B metallic glass samples treated with lower laser fluence (<0.49 J/mm^2) underwent structural relaxation while higher laser flounces led to partial crystallization. The crystallization temperature experienced an upward shift due to rapid heating rates of the order of 10^4 K/s during laser treatments. The heating cycle was followed by termination of laser upon treatment attainment of peak temperature and rapid cooling of the similar order. Such dynamic effects resulted in premature arrest of the crystallite growth leading to formation of fine crystallites/grain (~32 nm) of α-(Fe,Si) as the major component and Fe_2B as the minor component. The structural relaxation, crystallization fractions of 5.6–8.6 Vol% with α-(Fe,Si) as the main component, and crystallite/grain size of the order of 12 nm obtained in laser fluence range of 0.39-0.49 J/mm^2 had minimal/no influence on tensile behavior of the laser treated Fe-Si-B metallic glass foils. An increase in laser fluence led to progressive increase in crystallization fractions with considerable amounts of Fe_2B (2-6 Vol%) and increase in grain size to ~30 nm. Such a microstructural evolution severely reduced the strength of Fe-Si-B metallic glass. Moreover, there was a transition in fracture surface morphology of laser treated Fe-Si-B metallic glass from vein pattern to chevron pattern. Tensile loading lacked any marked influence on the crystallization behavior of as-cast and structurally relaxed laser-treated metallic glass foils. However, a significant crystallite/grain growth/coarsening of the order of two and half times was observed in the fractured region compared to the region around it for the laser-treated partially crystallized metallic glass foils. The simultaneous effects of stress generation and temperature rise during tensile loading were considered to play a key role in crystallite/grain growth/coarsening.

ACKNOWLEDGMENTS

As I reach the final phases of writing this dissertation, I am thinking about my tenure as a PhD student and prior times. This moment reminds me that there are many people who directly or indirectly helped me to stay motivated and move ahead in my research work. I know that a page of written note here won't be enough to thank the people who have always supported me but this written note will help me to cherish these moments in years to come.

I would like to first of all thank my advisor Dr. Narendra B. Dahotre. The years have built a strong relationship between us. His training and philosophy have shaped myself and my thinking. He and his wife are like local guardians and parents to me and my wife. Words are not enough to thank Dr. Dahotre.

I gratefully acknowledge Dr. Banerjee, who is like my co-advisor and an excellent teacher. Collaborations with him also provided me a valuable opportunity to work and interact with Dr. Srikumar Banerjee, a great Indian scientist. I want to thank Dr. Mukherjee, Dr. Young, and Dr. Du; my committee members for their guidance. I want to acknowledge Dr. Collins, Iman, and Peyman for their help with FIB/TEM. I thank Dr. Srini, Dr. Scharf, Dr. Shepherd, and all the MTSE faculty for their excellent courses. I want to acknowledge Dr. Voevodin for his guidance and encouragement. I want to thank Craig, David(s), and Saul for their help in the experiments. I want to thank Ashley and Lisa for their support and help. I acknowledge Dr. Subodh and Dr. Seshan; my IISc advisors during M.Sc.(Engg.). I want to acknowledge National Science Foundation for the financial support.

I want to thank current and past members of the lab (especially Shravana, Anna, Thomas, Ravi, and Dios). I wish to thank my friends (Tushar, Nilesh, Sumeet, Aniket, Sanghita, Jitendra, Urmila, Matt, Aditya(s), Parul, Sushant, Dr. Sandeep Kulkarni, Anup, Shantanu, Satish, Adwait, Adarsh, Lalitha, Karan, and Chetan to name a few). I express my gratitude to all my family members. I want to thank my grandmother for always being an inspiration. I wish to thank my brother and his family. I want to thank my parents (who are teachers themselves) for their motivation, support, and love. Last but not the least, I wish to thank my wife Dr. Ritu. Her constant support and love always help me cruise ahead!

TABLE OF CONTENTS

Page

ACKNOWLEDGMENTS iii

LIST OF TABLES vii

LIST OF FIGURES viii

CHAPTER 1 INTRODUCTION 1
- 1.1. Brief Background 1
- 1.2. Objectives of Present Work 2
- 1.3. Organization of Thesis 2

CHAPTER 2 LITERATURE REVIEW 5
- 2.1. Metallic Glasses 5
- 2.2. Effects of Thermal Energy on Metallic Glasses 9
  - 2.2.1. Structural Relaxation 9
  - 2.2.2. Crystallization 11
- 2.3. Mechanical Behavior of Metallic Glasses 18
  - 2.3.1. Formation of Shear Bands 18
  - 2.3.2. Dependence of Response to Load on Crystallizations and Loading Directions 19
  - 2.3.3. Temperature Rise in Shear Bands and Fracture Behavior 22
- 2.4. Brief Overview of Material and Processing Method Under Consideration 25

CHAPTER 3 EXPERIMENTAL AND COMPUTATIONAL PROCEDURES 28
- 3.1. Material 28
- 3.2. Laser Thermal Treatments 28
- 3.3. Identification/Characterization of Crystallization and Phase Evolution 31
  - 3.3.1. X-ray Analysis 31
  - 3.3.2. Calorimetric Analyses 31

3.3.3. Resistivity Measurements 31
3.3.4. Electron Microscopy 32
3.4. Computational Model 32
3.5. Tensile Testing 36
3.6. Optimization 37
3.7. Fractography 38
3.7.1. Observations of Fracture Surface Morphology 39
3.7.2. Site Specific Transmission Electron Microscopy 39

CHAPTER 4 RESULTS AND DISCUSSION 41
4.1. Effects of Laser Thermal Treatment on Crystallization of Fe-Si-B Metallic Glass 41
4.1.1. Observations of Crystallite and Phase Evolution 41
4.1.2. Computational Predictions of Thermal Effects 48
4.1.3. Influence of Thermokinetic Effects during Laser Treatments on Crystallization 48
4.2. Tensile Behavior and Process Optimization of Laser treated Fe-Si-B Metallic Glass 56
4.2.1. Observations of Stress Strain Behavior 56
4.2.2. Localized Structural Changes during Laser Thermal Treatments 57
4.2.3. Statistical Process Optimization to realize Structure-Tensile Property Relationship 59
4.2.4. Microstructure Evolution and its Effects on Tensile Behavior 64
4.3. Effects of Tensile Loading on Crystallization of Laser Treated Fe-Si-B Metallic Glass 73
4.3.1. Fracture Behavior 74
4.3.1.1. Microscopic Features of Fractured Region 76
4.3.1.1.1 Surface morphology 76
4.3.1.1.2 Structural Changes Evolved upon Tensile Loading 78

4.3.2. Thermomechanical Effects Induced during Tensile Loading 79

CHAPTER 5 CONCLUDING REMARKS 88

5.1. Structural Changes and Phase Evolution 88

5.2. Tensile Behavior 89

5.3. Effect of Loading on Crystallization 90

CHAPTER 6 FUTURE SUGGESTIONS 91

APPENDIX LIST OF PUBLICATIONS 94

REFERENCES 97

LIST OF TABLES

Page

Table 2.1. Summary from the Previous Work of Magnetic Properties of Fe-Si-B Metallic Glass in Various Conditions [1] 26

Table 3.1. Laser Processing Parameters Employed during Crystallization Studies 30

Table 3.2. Laser Processing Parameters Employed during Tensile Behavior Studies 31

Table 3.3. Thermophysical and Processing Parameters Employed in FE Model 35

Table 4.1. Fraction of Crystallization from DSC Analysis 46

Table 4.2. Microstructure Development and Tensile Properties of Laser Treated Fe-Si-B Metallic Glass 73

Table 4.3. Summary of Microstructure and Tensile Behavior of Laser Treated Fe-Si-B Metallic Glass Foils Selected for Investigating Effects of Loading on Crystallization. 74

Table 4.4. Estimated Localized Strain and Activation Energy of Crystallite/Grain Growth 85

LIST OF FIGURES

Page

Figure 2.1. Electron diffraction patterns belonging to (a) nano crystalline Fe-Si-B alloy showing crystalline rings and (b) the corresponding amorphous counterpart. 7

Figure 2.2. Variation in specific volume as a function of temperature in case of glass and crystal formation. 7

Figure 2.3. Strength versus elastic limit of glassy alloys compared to other structural materials [2]. 8

Figure 2.4. Time line of evolution of thickness of metallic glasses of various compositions [2]. 9

Figure 2.5. Process of structural relaxation illustrated by a schematic of a variation in property that is density of a metallic glass as a function of relaxation temperature. The dotted line represents "ideal" glass with lowest possible energy [3]. 11

Figure 2.6. A typical non-isothermal DSC curve obtained during crystallization of metallic glass. The heating rate used is indicated along with glass transition temperature (T_g), crystallization temperature (T_x), and melting temperature (T_m) [4]. 12

Figure 2.7. Heating rate dependence of crystallization commencement temperature shown in case of $Pd_{76}Y_9Si_{15}$ metallic glass as an example [5]. 13

Figure 2.8. Fracture toughness as a function of Young's modulus for various structural materials. The metallic glass composites are highlighted with an arrow [6]. 15

Figure 2.9. Graphs illustrating grain growth characteristics of nano crystalline Fe at various temperatures during isothermal furnace annealing [7]. 16

Figure 2.10. Formation of shear transition zones on application of stress within a metallic glass [8]. 20

Figure 2.11. Surface markings caused by shear bands, observed on the tensile side of a bent wire (diam. 100 mm) of a $[(Fe_{50}Co_{50})_{75}B_{20}Si_5]_{96}Nb_4$ (in at.%) metallic glass [9]. 20

Figure 2.12. Schematic illustrating differences in tensile stress strain behavior of amorphous and crystalline materials along with the key microstructural differences leading to different deformation mechanisms. The composite has been constructed from references [10–15]. 21

Figure 2.13. Melting of tin coating on the Zr-based metallic glass upon fracture [16]. This is one of the first experimental evidences about temperature rise during fracture of a metallic glass. 24

Figure 2.14. Set of figures illustrating (a) formation of shear offset during propagation of shear band in the cross-section of the sample [17] and (b) appearance of vein pattern on the fracture surface of the metallic glass [18]. 24

Figure 2.15. (a) Instability of the fluid meniscus in the crack tip [19] (b) Illustration of the catastrophic fracture process [20]. Where $\frac{d\sigma_N}{dz}$ is the pressure gradient with respect to normal stress σ_N and R is the radius of curvature of the meniscus. 25

Figure 3.1. Schematic of the Fe-Si-B metallic glass foil used in the current work. Features such as region subjected to laser thermal treatment and griping areas during mechanical tests have also been shown. 29

Figure 3.2. Schematic of setup during laser thermal treatments of Fe-Si-B metallic glass. 30

Figure 3.3. Schematic of geometry of model used in current study. 33

Figure 3.4. Differential scanning calorimetry curve showing heat of crystallization for as cast Fe-Si-B metallic glass foil. 36

Figure 3.5. Flow diagram for experimental procedures and subsequent statistical optimization study. 38

Figure 3.6. Set of micrographs showing (a) the regions for FIB lift out for a tensile

fractured laser treated Fe-Si-B metallic glass, high magnification view showing (b) FIB lift-out region at the fractured region within the laser track, and (c) FIB lift-out region away from the fracture. 40

Figure 4.1. XRD patterns of Fe-Si-B metallic glass foil samples subjected to various laser energy inputs indicating crystallization. 43

Figure 4.2. Variation of crystallite size with laser fluence, beam residence time, peak temperatures reached and scanning speed. 44

Figure 4.3. DSC curves for Fe-Si-B metallic glass foils treated with various laser flunces. They indicate two crystallization events and reduction in area under the curve for those with progressive crystallization. 45

Figure 4.4. TEM micrograph of laser processed Fe-Si-B metallic glass foil showing (a) bright field image revealing nano grains and (b) the corresponding diffraction pattern indicating evolution of α-(Fe,Si) and Fe_2B. 47

Figure 4.5. Temperature as a function of time for various laser processing conditions as predicted by the thermal model. 49

Figure 4.6. Heating and cooling rates predicted by thermal model during various laser scanning speeds. 50

Figure 4.7. Variation in (a) onset of crystallization temperature in laser treatment T_{laser}, arrest temperature T_{arrest}, and (b) peak temperature T_{peak} with laser beam scanning speed. 51

Figure 4.8. Schematic of time-temperature curve illustrating concept of arrest temperature, time of growth Δt, and dynamic nature of laser processing. 54

Figure 4.9. Dynamic nature of process reflected in variation of time of growth (Δt) and difference between peak and arrest temperatures (ΔT) with scanning speed. 55

Figure 4.10. Representative engineering stress-strain curves are depicted for Fe-Si-B metallic glass foils treated with single laser track at the center of gage length. 57

Figure 4.11. Variation in the resistivity of laser treated Fe-Si-B metallic glass foils as a function of laser fluence. 60

Figure 4.12. A possible structural evolution as a function of laser fluence for laser treated Fe-Si-B metallic glass. 60

Figure 4.13. Set of plots showing predicted vs actual values for and (a) UTS/fracture strength and (b) electrical resistivity and externally studentized values versus predicted values by the function showing a random scatter for (c) UTS/fracture strength and (d) electrical resistivity. 61

Figure 4.14. Behavior of desirability as a function of laser fluence. 64

Figure 4.15. XRD patterns of Fe-Si-B metallic glass foils subjected to various laser energy inputs investigated during this study on tensile behavior. 66

Figure 4.16. TEM micrographs and their corresponding SAD pattern in the inset for a) 0.42 J/mm^2 revealing amorphous structure, b) 0.49 J/mm^2, c) 0.61 J/mm^2 and d) 0.71 J/mm^2 laser fluences clearly showing the presence of nanocrystals and the phases formed as a result of crystallization. 68

Figure 4.17. DSC curves for Fe-Si-B metallic glass foils treated with various laser flunces investigated during study on tensile behavior. 70

Figure 4.18. Normalized UTS/fracture strength values for the Fe-Si-B foils as a function of laser fluence. 72

Figure 4.19. Set of images showing trail of waves in different length scales. Image on the left is a photo of trails/pattern created by a boat and a surfer traveling on water surface. Correspondingly, image on the right shows the pattern created by crack traveling within metallic glass during fracture. 75

Figure 4.20. SEM fractographs recorded at the operating voltage of 15 keV using Everhart-Thornley secondary electron detector showing fracture surface of (a) as-cast foil revealing a vein pattern and (b) 0.42 J/mm^2 (500mm/s), (c) 0.49 J/mm^2 (430 mm/s), and (d) 0.71 J/mm^2 (300 mm/s) laser treated metallic glass foils revealing a variation in fracture surface morphology. 77

Figure 4.21. Set of TEM micrographs and the SAD patterns in the inset showing microstructures of (a) - (b) as-cast Fe-Si-B metallic glass foil, (c) -(d) Structurally relaxed laser treated Fe-Si-B metallic glass foil, and (e) - (h) partially crystallized laser treated Fe-Si-B metallic glass foils. The images on the left column represent the microstructure from the location away from the fractured surface, whereas images on the right column correspond to the microstructure at the fractured surface of these samples. In addition, the process of grain size determination has been depicted in Fig. 3(g) and (h) where few grains are marked by a dotted boundary. Further, the linear measurement for grain size determination in horizontal and vertical directions has been illustrated using arrowed lines in one of the grains. 80

Figure 4.22. TEM micrograph of laser thermal treated Fe-Si-B metallic glass foil corresponding to laser fluence of 0.71 J/mm^2 without any loading. 81

Figure 4.23. Set of figures showing (a) schematic of a Fe-Si-B metallic glass sample undergoing tensile loading, (b) schematic of shear band extending into a crack, (d) temporal distribution of temperature from the center of a shear band at distance of 1 nm, and (c) spatial distribution of temperature time of 1 ns from the center of the shear band. 83

Figure 4.24. Illustration of localized plasticity in Fe-Si-B metallic glass foils showing (a) SEM micrograph of extended veins in as-cast Fe-Si-B metallic glass foil, (b), and (c) TEM micrographs corresponding to laser fluence of 0.49 and 0.71 J/mm^2 respectively showing step like features and elongated deformed grains as indicated by the arrow markers. 87

Figure 6.1. Schematic illustrating possible laser patterning treatments of Fe-Si-B metallic glass. 93

CHAPTER 1

INTRODUCTION

1.1. Brief Background

Metallic glasses possess attractive properties, such as high strength, good corrosion resistance, and superior soft magnetic performance [2, 4, 21–23]. They also serve as precursors for synthesizing nanocrystalline materials which in turn have superior properties such as mechanical performance and high hardness [24]. In addition, composite materials with nano/micro crystals embedded within an amorphous matrix hold the potential for further enhancing these properties by combining the characteristics of metallic glasses and nanocrystalline alloys [12, 25, 26]. Thus selective/complete crystallization of metallic glasses is the topic of research interest in the process of development of next generation structural and functional materials.

There are various conventional furnace based and non conventional methods such as electron beam processing, flash annealing, and laser processing have been employed for crystallization of metallic glasses [27–31]. Among these methods, laser processing offers distinct advantages such as faster processing, rapid heating and cooling, and suitability for continuous processing [30, 32]. Moreover, previous investigations from our research group related to laser assisted crystallization of Fe-Si-B metallic glass (an excellent soft magnetic material by itself) showed a further improvement in soft magnetic performance. However, for actual implementation during application also requires a reliable mechanical performance [1]. This becomes important in application such as a transformer core which may get subjected to sudden current surge, unexpected mechanical loading, or thermal shocks potentially leading to catastrophic failure. In light of this, it becomes important to understand the crystallization, phase and microstructural evolution during non-equilibrium laser processing of Fe-Si-B metallic glass and in turn its effects on mechanical properties. This forms the basis of the current work. The following Section chalks out the goals of the present work.

1.2. Objectives of Present Work

Based on the brief background discussed in previous paragraphs, the main objectives of the current work are as follows:

- To examine the process of crystallization of Fe-Si-B metallic glass driven by the non equilibrium thermokinetic conditions during laser processing.
- To investigate evolution of microstructure and phases within the laser treated area of the Fe-Si-B metallic glass.
- To determine the effects of structural changes and microstructural evolution on tensile behavior of laser treated Fe-Si-B metallic glass.
- To explore the statistical methods for rapid optimization of structure-tensile property relationship in laser treated Fe-Si-B metallic glass.
- To investigate the effect of loading on crystallization behavior of laser treated Fe-Si-B metallic glass for investigating microstructural changes occurring during the loading.

The objectives are collectively intended to understand the physics involved in laser material interaction and it's effect on the mechanical performance. The efforts to reach these objectives consisted of an integrated experimental and computational approach. Based on this discussion, the flow of thesis is presented in the next Section.

1.3. Organization of Thesis

The dissertation document has been based on the "traditional thesis format" rather than the "paper format" to which many graduate students are opting for in the recent times. Therefore, the current Chapter 1 provides a brief background about the topic, metallic glass based materials, and the work previously done by the author's research group. Based on this information, the problem statement of the thesis is defined followed by specific objectives/targets of the work. A literature review related to fundamentals of metallic glasses is presented in Chapter 2. It further goes into details such as effects of thermal energy on metallic glasses giving information about crystallization of metallic glasses, synthesis of crystalline phases into amorphous matrix to form metallic glass based composites, and various routes by which such materials can be produced. Chapter 2 then focuses on mechanical behavior of the metallic glass based materials and contrasts it with conventional crystalline structural metals and alloys. The Chapter 2 then concludes by giving a brief overview of the material and process under consideration for the current work. The thesis then provides the experimental and computational methodologies followed during the current work in Chapter 3.

Chapter 4 forms the heart of this thesis and is dedicated to the important findings of the current work. The Chapter 4 has been subdivided into Sections previously. Each finding has been coupled with possible fundamental explanations. Chapter 5 discusses important conclusions of the current work. A set of possible future directions based on the findings of the current work has been given in Chapter 6. Apart from these main Chapters, an Appendix is included which lists all the publications related to various projects the author worked on during his tenure as a graduate student in the current research group. Finally, a comprehensive list of references cited in the current work is provided.

Another important note to be mentioned here is, the literature review and the research work presented in this thesis is borrowed in part/as it is from the following list of publications by the author in the leading position with the permission from respective publisher:

(1) Joshi, Sameehan S., et al. "Dynamic crystallization during non-isothermal laser treatment of Fe–Si–B metallic glass." Journal of Physics D: Applied Physics 48.49 (2015): 495501. (with permission from IOP Publishing Ltd)
(2) Joshi, Sameehan S., et al. "Tensile behavior of laser treated Fe-Si-B metallic glass." Journal of Applied Physics 118.16 (2015): 164904. (with permissions from AIP Publishing LLC)
(3) Joshi, Sameehan S., et al. "Optimization of laser thermal treatment of Fe–Si–B metallic glass." Journal of Manufacturing Processes 24 (2016): 31-37. (with permission on behalf of The Society of Manufacturing Engineers from Elsevier Ltd)
(4) Joshi, Sameehan S., et al. "Crystallisation behaviour during tensile loading of laser treated Fe–Si–B metallic glass." Philosophical Magazine 97.7 (2017): 497-514. (with

permission from Taylor & Francis)

These permissions notes are reiterated wherever applicable with the specific publication under consideration.

CHAPTER 2

LITERATURE REVIEW

> *All liquids would become glasses at sufficiently low temperature, if crystallization did not intervene.*
>
> D. Turnbull and M. Cohen

2.1. Metallic Glasses

Usually, metallic materials when cooled from the melt solidify having regular repetitive arrangements of constituent atoms, resulting in characteristic crystalline structures. Crystalline structure can be detected using a diffraction experiment such as TEM electron diffraction which consists of characteristic rings or spots depending on the type of crystal structure and elements present (e.g. Fig. 2.1 a). Such an ordered structure plays a decisive role in determining various properties of crystalline metallic alloys. However, it was observed by Paul Duwez and coworkers in 1959 that when a $Au_{80}Si_{20}$ alloy was rapidly quenched from molten state, a disordered atomic arrangement was observed on solidification [33]. This disordered arrangement is called as amorphous structure and results in halo like electron diffraction pattern (Fig. 2.1 b). Such a phenomenon is regularly witnessed in case of polymers and silicate glasses even with the cooling rates that are not so severe. One of the important reason in formation of disordered/amorphous structure is difficulty in movement of atoms in liquid to end up in ordered arrangement [34]. The kinetics plays a key role during glass formation depending on the composition of the liquid being cooled as stated in the quote at the beginning [35].

The process of glass formation can be tracked by monitoring variation in a property with temperature such as specific volume (Fig. 2.2). In the case of crystallization, there is a discontinuity observed in the graph at the melting temperature (T_m) followed by completion of solidification and then a steady decrease in specific volume (Fig. 2.2). When the cooling rate is higher, the liquid gets retained even below melting temperature entering a supercooled state. As the temperature drops, the liquid becomes more and more viscus (viscosity values as high as 10^{16} have been reported [36]) until a point when significant atomic movement is no longer possible and liquid then solidifies into a disordered solid. Thus it can be said that glasses are rigid like a solid but disordered like a liquid [34]. The temperature at which glass solidification takes place is termed as glass transition temperature (T_g) as schematically shown in Fig. 2.2. It is worth noting here that the T_g is heavily dependent on the rate of change of temperature [4, 37–39]. Cooling beyond T_g does result in reduction in specific volume, but at any temperature below T_g, the solidified glass has an excess volume as compared to its crystalline counterpart. This excess volume is termed as *free volume* (Fig. 2.2) and it basically points towards the metastable nature of glassy materials [35]. On the other hand, free volume also increases the configurational entropy of the overall system and depending upon the chemistry of the composition, may help stabilizing the glassy state by increasing the free energy barrier between amorphous and crystalline structures [35]. It is worth noting here that the process of glass formation/amorphization need not always require a route consisting of cooling from liquid state and may happen directly in solid state. Means such as high energy ion or radiation bombardment result in large defect concentration in the solid and, thus, producing a disordered glassy structure on collapse of the crystalline order [4, 40, 41].

In case of metallic systems, the process of amorphization is much more difficult as thermodynamic and kinetic conditions required need a careful alloy design. A characteristic of the alloy termed as a *glass forming ability* (GFA) provides an idea about ease with which it can form glassy structure. These metallic alloys solidified amorphous are called metallic glasses. Owing to disordered/amorphous structure, metallic glasses posses unique set of properties including very high strength, good corrosion resistance as a result of absence of grain boundaries, excellent soft magnetic properties, high hardness and wear resistance [1, 4, 12, 22, 42–47]. As an example, the strength of metallic glasses is much higher than conventional materials like high strength steels (Fig. 2.3).

During early research since 1960 after discovery, metallic glasses were synthesized

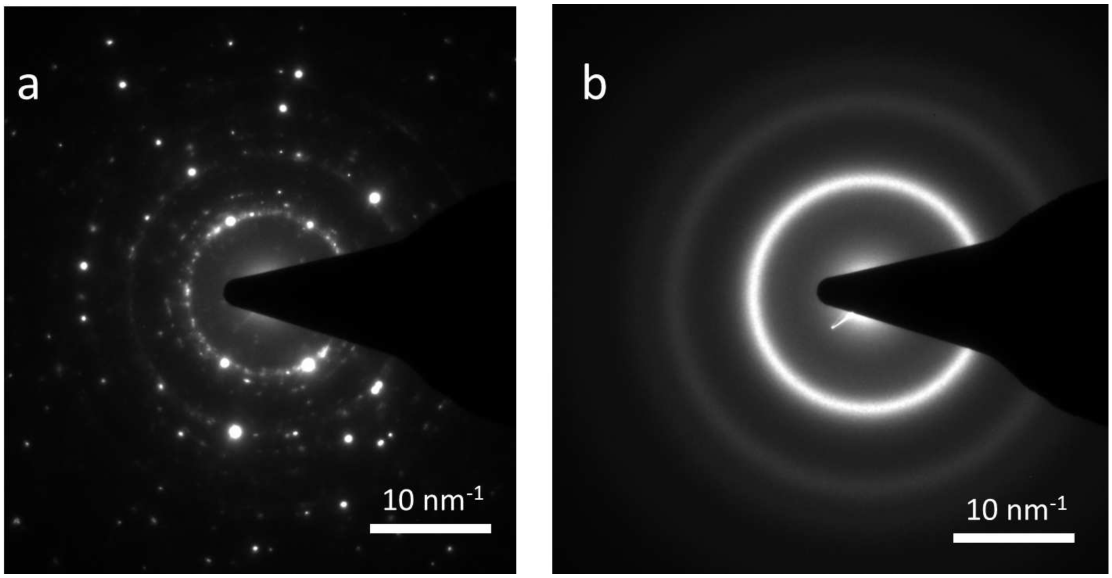

Figure 2.1. Electron diffraction patterns belonging to (a) nano crystalline Fe-Si-B alloy showing crystalline rings and (b) the corresponding amorphous counterpart.

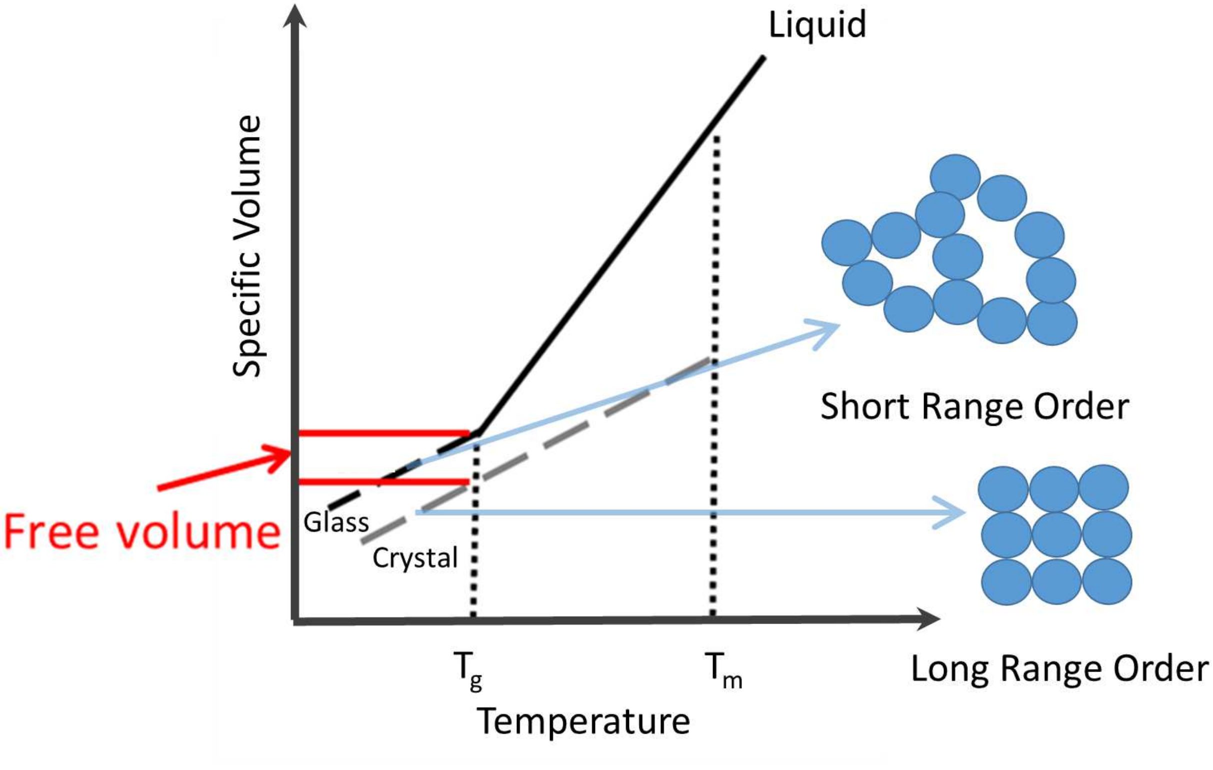

Figure 2.2. Variation in specific volume as a function of temperature in case of glass and crystal formation.

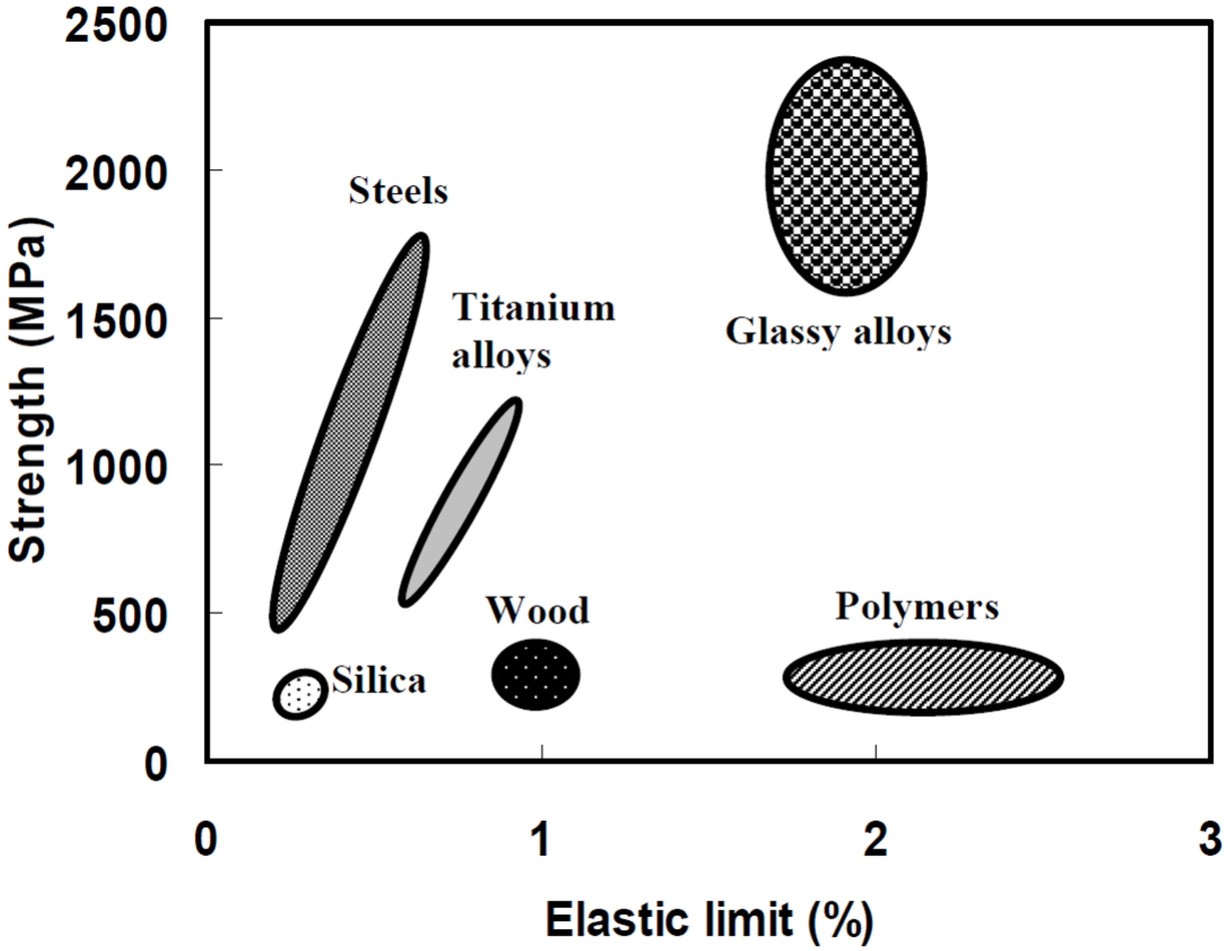

FIGURE 2.3. Strength versus elastic limit of glassy alloys compared to other structural materials [2].

majority as thin foils of few micron thickness and mostly confined to alloy systems like gold and palladium based alloys. With advancement however, new systems were designed based on elements such as Zr, Ti, Ni, Fe, Mg, Al, etc. and at the same time the cross sectional thickness obtained as amorphous also increased (Fig. 2.4). The thicknesses obtained were of the order of few centimeters coining the name bulk metallic glass (BMG) describing such thick metallic glasses. The first commercially scaled BMG was $Zr_{41.2}Ti_{13.8}Cu_{P}12.5Ni_{10.0}Be_{22.5}$, popularly known as vitrealloy. Owing to the unique set of properties origin of which traces to the amorphous structure, BMGs and metallic glasses in general are being considered and to certain extent actually put into real life applications. However, metallic glasses being metastable have some inherent limitations including structural relaxation and

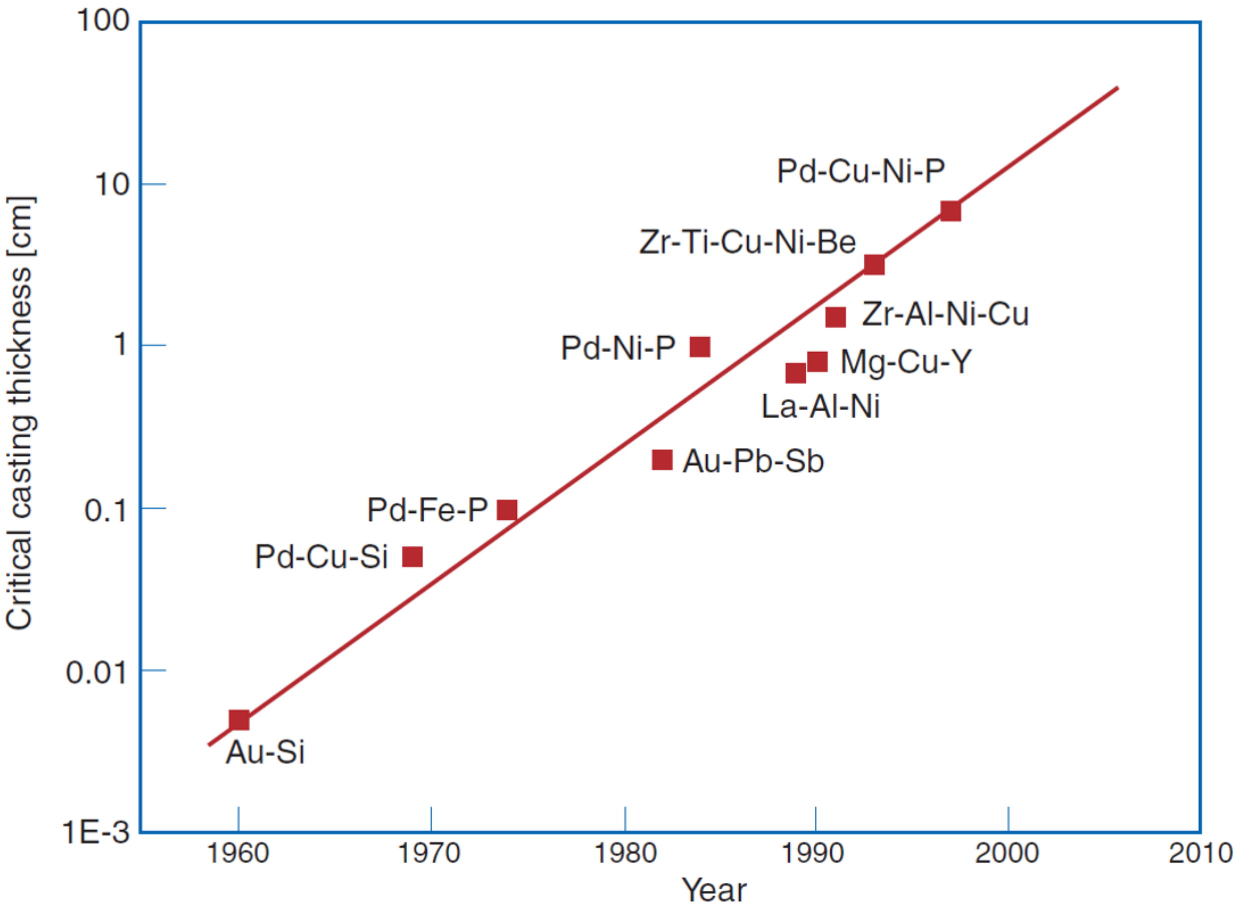

Figure 2.4. Time line of evolution of thickness of metallic glasses of various compositions [2].

crystallization at elevated temperatures, limited ductility, and cross section that can be obtained as amorphous. Structural relaxation and crystallization can have significant effects on properties of metallic glasses. Furthermore, it has also been reported that controlled crystallization may even improve mechanical and magnetic performance of the metallic glasses [1, 6, 25]. In light of this, the following subsection discusses the fundamentals of the structural relaxation and crystallization process of metallic glasses.

2.2. Effects of Thermal Energy on Metallic Glasses

2.2.1. Structural Relaxation

Reiterating from the quote at the beginning of this Chapter, David Turnbull and Morrel H. Cohen state in their classic paper that every liquid would like to become a glass, unless crystallization intervenes [35]. As discussed in previous section, metallic glasses are arrested from getting crystallized by means of kinetic effects induced during rapid cooling. Even though, in general, the metallic glasses have a short range order at the atomic level, the degree of metastability may be different depending upon the composition and kinetics of the glass formation [4]. Furthermore, response of a metallic glass to thermal energy depends on such degree of metastability as well as amount of energy being input. If the heat flowing into the glass is not sufficient to pass the energy barrier of crystallization, a process called structural relaxation takes place [48, 49]. In this course, the overall free energy of the glass gets reduced transforming it to a more stable glassy structure than the starting point. Heat energy just insufficient to cause the crystallization transforms the glass to "ideal" condition wherein the physical properties of the glass are same as the equilibrium liquid from which the glass was formed extrapolated to the relaxation temperature. The relaxation process has two components [48]:

1. Topological short range order which requires more energy input and is characterized by substantial reduction in the free volume.
2. Compositional short range order characterized by the way atoms get arranged and can be described by activation energy curves.

The first component induces irreversible structural relaxation, whereas the second one leads reversible structural relaxation. Detailed analyses about mechanisms of structural relaxation has been provided in the literature [48–52]. The structural relaxation can be tracked by monitoring a variation in property such as modulus, hardness, density, and electrical resistivity of the glass [53–56]. A schematic is presented in Fig. 2.5 which illustrates the variation in a density as function of relaxation temperature. Thus, it is clear that structural relaxation may have a key influence on the properties of metallic glasses which are inherently metastable. Moreover, structural relaxation can be proceeded by crystallization which can further affect the properties. The process of crystallization of metallic glasses is discussed in the following paragraphs.

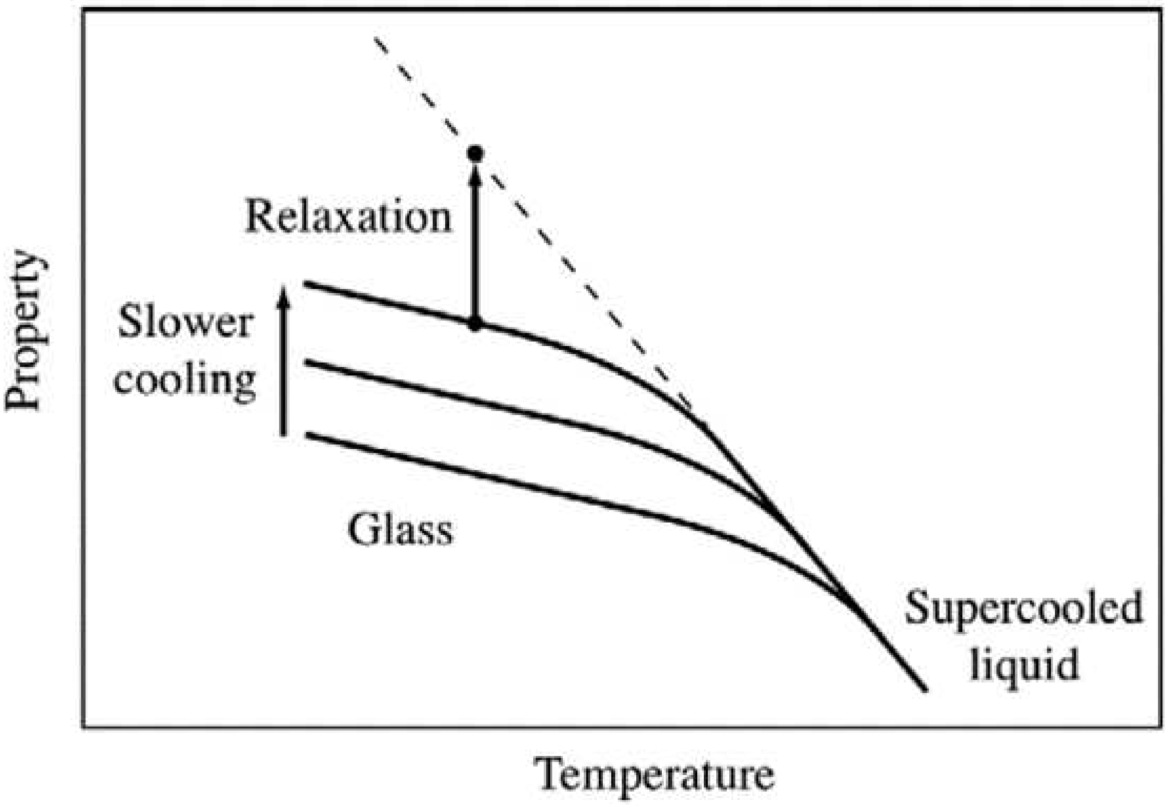

FIGURE 2.5. Process of structural relaxation illustrated by a schematic of a variation in property that is density of a metallic glass as a function of relaxation temperature. The dotted line represents "ideal" glass with lowest possible energy [3].

2.2.2. Crystallization

Provision of sufficient energy to the frozen amorphous structure would result in its transformation to the more stable crystalline phase(s). A good tool to track the process of crystallization of metallic glass is non-isothermal differential scanning calorimetry (DSC). The sample is heated at a predetermined constant heating rate under inert environment and heat flowing into the sample with respect to a reference material is monitored as a function of temperature. An example of the resultant plot is shown in Fig. 2.6. As the temperature increases a small hump is observed in the curve until T_g, when metallic glass starts absorbing heat and enters the super cooled liquid region. This region spans till crystallization temperature (T_x) at which the excess energy starts to evolve and long range atomic order gets introduced. On a side note in context to structural relaxation discussed in the previous paragraph, the area under this exothermic peak for heat treated metallic glass can be monitored with respect to non-heat treated glass to quantify the degree of structural relaxation [4]. Each peak appearing here after corresponds to phase separation by crystallization. T_x depends on and increases as a function of heating rate (Fig. 2.7[4]). Ones the crystallization events conclude, the temperature keeps rising without any significant activity in heat flow until it reaches the melting temperature.

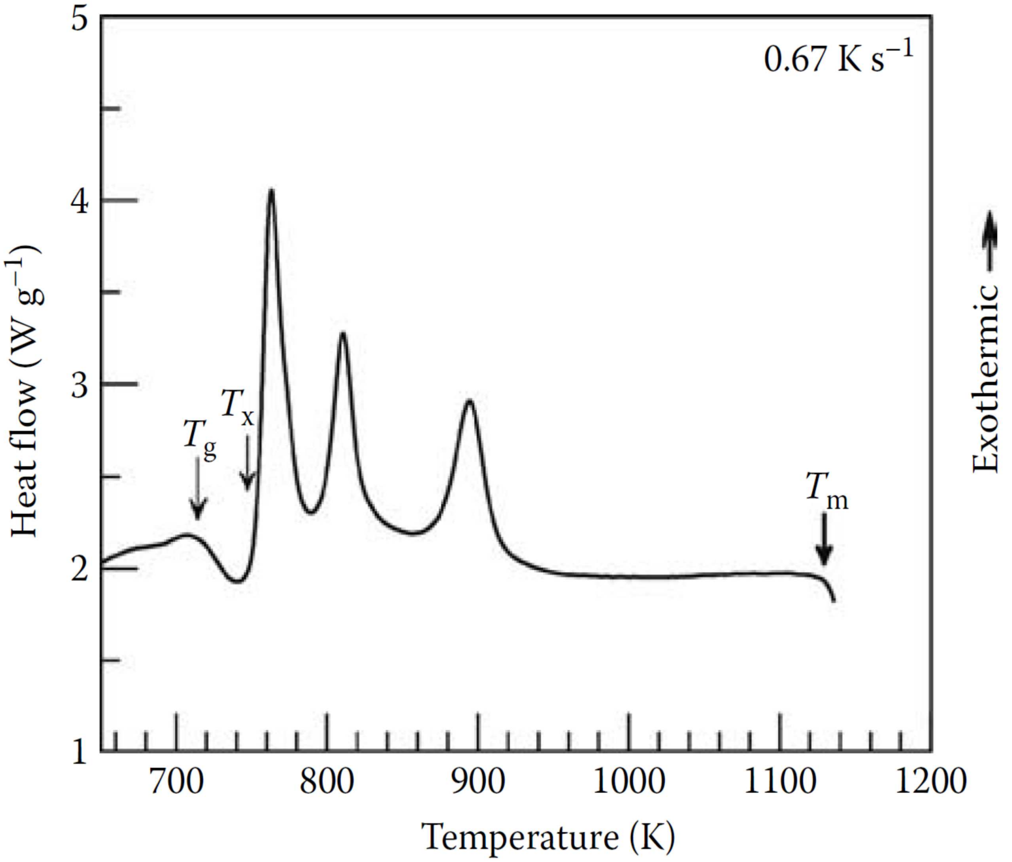

Figure 2.6. A typical non-isothermal DSC curve obtained during crystallization of metallic glass. The heating rate used is indicated along with glass transition temperature (T_g), crystallization temperature (T_x), and melting temperature (T_m) [4].

There are various modes in which crystallization of a metallic glass can take place [57–60] as mentioned below.

- Polymorphic crystallization: The composition of the crystalline phase remains same as the starting glass.

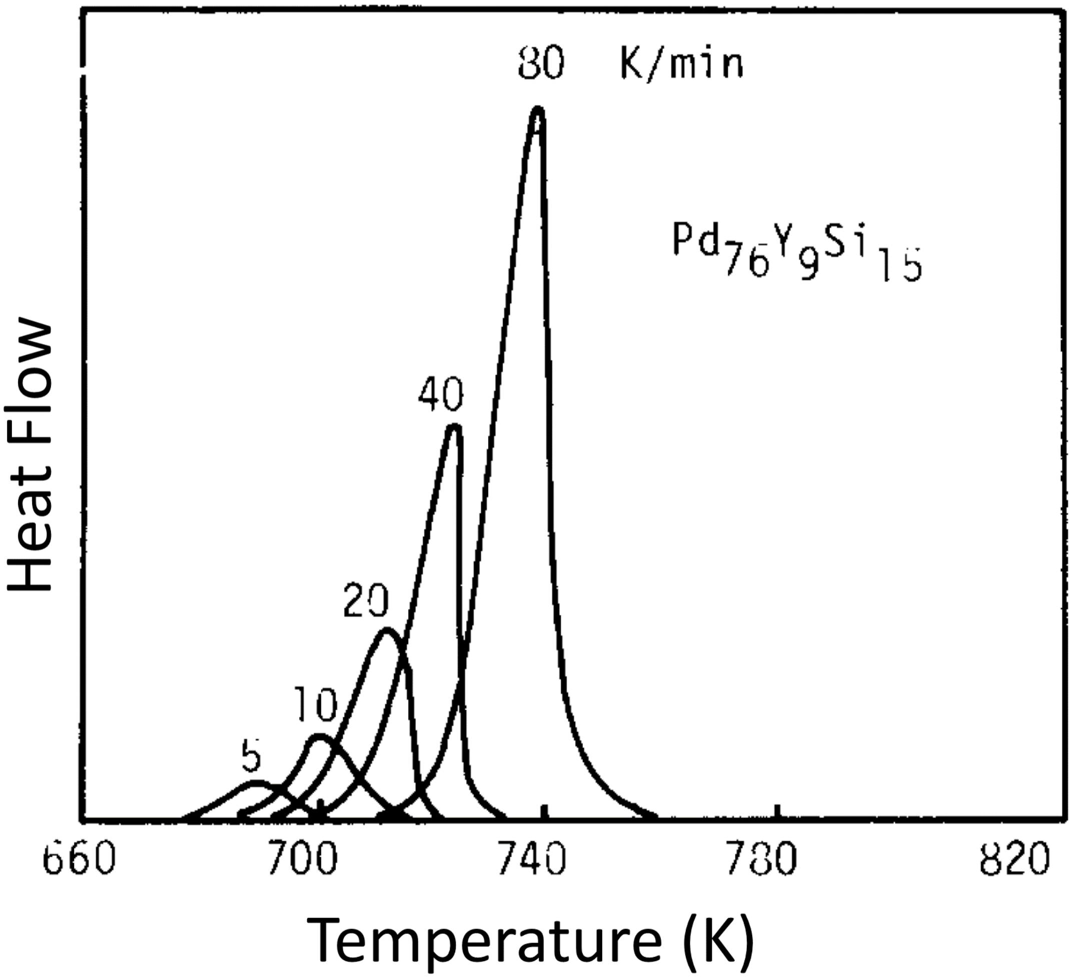

FIGURE 2.7. Heating rate dependence of crystallization commencement temperature shown in case of $Pd_{76}Y_9Si_{15}$ metallic glass as an example [5].

- Eutectic crystallization: Formation of the crystalline phases with two different compositions in a simultaneous manner is termed as eutectic crystallization.
- Primary crystallization followed by polymorphic or eutectic crystallization: A primary crystallization product with different chemical composition than that of the parent glass forms in the first stage. The composition of amorphous matrix also changes in this course. In the second stage, this matrix undergoes crystallization either by a polymorphic or by an eutectic mechanism.

The crystallization may reach completion or can be restricted to produce crystalline phases within the amorphous matrix. A newly emerging class of composite metallic glasses is based on partial crystallization of metallic glasses [12, 23, 25, 26]. These composite metallic glass materials combine performance of metallic glasses with crystalline alloys for resultant properties such as improved ductility [25, 26] and superior soft magnetic performance [61]. As an example, the fracture toughness of metallic glass composites is expected to be much higher than the conventional structural materials (Fig. 2.8). Additionally, as these glasses when subjected to heat treatment undergo nano crystallization serve as one of the desired methods for synthesis of nano crystalline materials [24, 62–68]. Therefore, the heat treatment not only helps to determine thermal stability of the metallic glasses, but can also be applied in controlled manner to serve as useful way of synthesis of crystallite reinforced amorphous (glass) matrix composite. Thus, there is an increasing research interest in crystallization of metallic glasses and synthesis of metallic glass based composites. Various processing techniques have been explored to achieve crystallization in metallic glasses. These techniques can be classified as:

(1) Isothermal or near isothermal techniques
(2) Non isothermal techniques

based on the thermokinetic conditions involved.

In the first set of methods, the metallic glass is heated usually in a furnace environment above the crystallization temperature. The onset of crystallization followed by growth of crystallite/grain is monitored as a function of time [7, 69]. It has been observed that the grains coarsen rapidly in initial period, and then the grain size reaches a saturation (Fig. 2.9). Impurity segregation at grain boundaries, reduced grain boundary curvature effects, and reduction in chemical gradients are some of the reasons behind reaching the saturation [7, 69, 70]. Such a behavior during isothermal treatment can be mathematically expressed (Eq. 2.1) as per the classic grain growth theory [69]

$$X^{\frac{1}{n}} - X_0^{\frac{1}{n}} = kt \tag{2.1}$$

where X is the grain/crystallite size at particular time t, X_0 is the initial grain/crystallite size

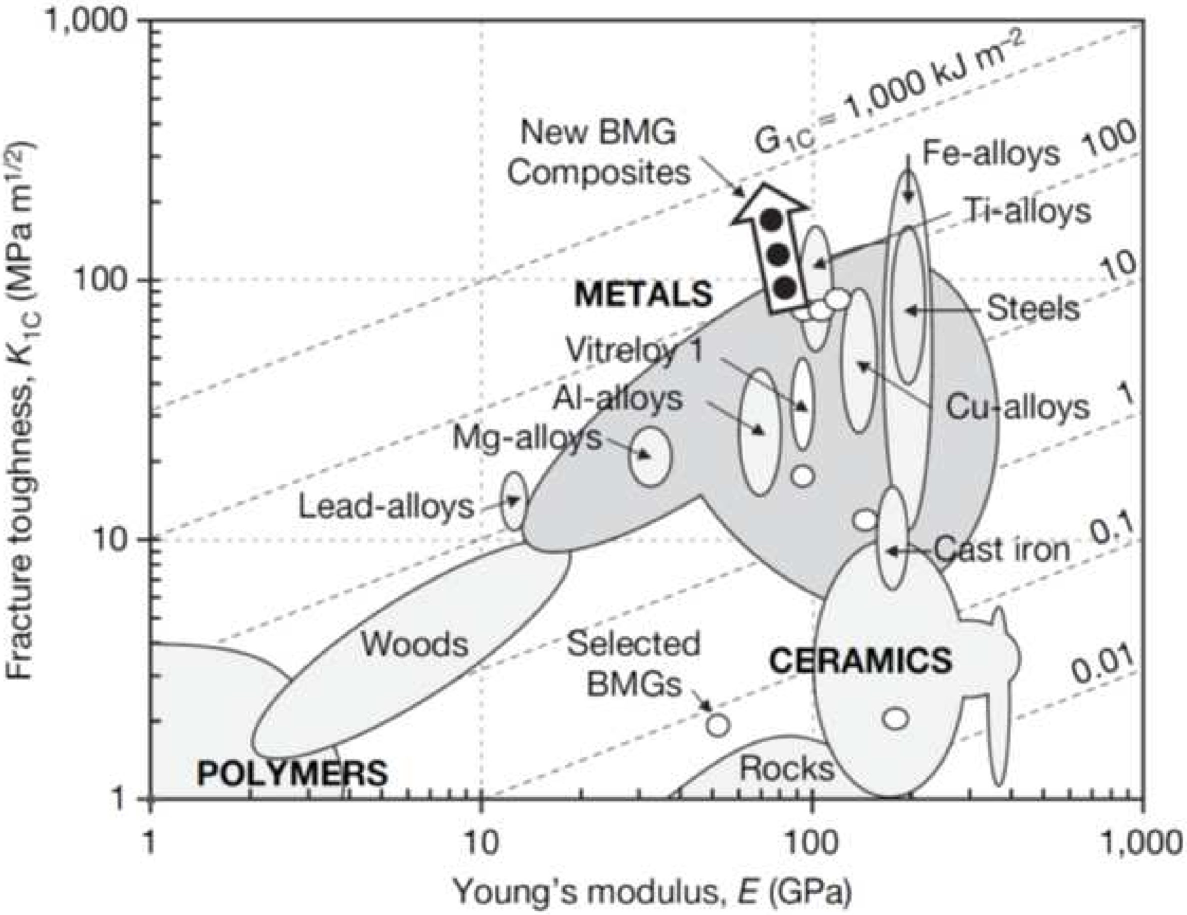

FIGURE 2.8. Fracture toughness as a function of Young's modulus for various structural materials. The metallic glass composites are highlighted with an arrow [6].

at t=0, n is the grain growth exponent, k is the temperature dependent rate constant. n can have values $\leqslant 0.5$ and k is expressed as k = $k_0 exp(\frac{-E}{RT})$, where k_0 is the frequency constant, R is the universal gas constant, E is the activation energy, and T is the temperature. However, in case of amorphous material system, it is reasonable to take value of X_0 as zero [69], hence the expression in Eq. 2.1 takes the form as indicated in Eq. 2.2.

$$X^{\frac{1}{n}} = kt \tag{2.2}$$

Although conventional isothermal or near isothermal heating (annealing) is a feasible method of inducing crystallization followed by nano/micro grain growth in amorphous phase and is

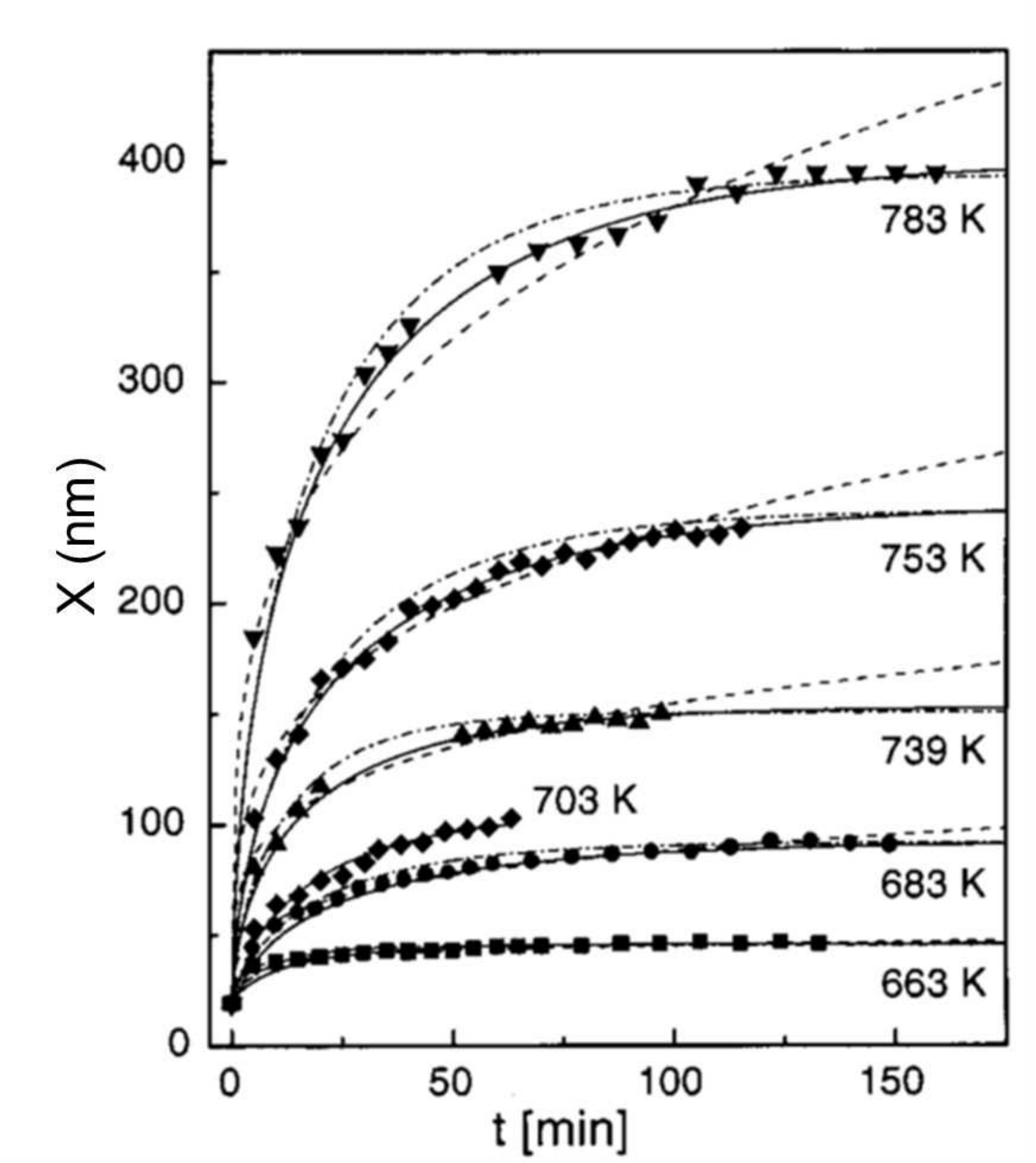

Figure 2.9. Graphs illustrating grain growth characteristics of nano crystalline Fe at various temperatures during isothermal furnace annealing [7].

simple to adopt, it may have some inherent problems such as oxidation, uncontrolled and uneven heating of the entire material, and possibility of uncontrolled grain growth. In light of this, some alternative novel techniques have also been explored for this purpose such as flash annealing [28], microwave heating [29], and laser processing [1, 30, 43, 71]. Flash annealing consists of holding the material at constant high temperature (static heating) in a furnace for short amount of time on the order of few seconds, followed by rapid quenching. Whereas, microwave induction heating consists of exposing the material to microwave radiation (dynamic heating) leading to rise in temperature and crystallization. Both these methods heat the entire bulk of sample. On the contrary to these two techniques, laser thermal treatment is capable of instantaneously spatially (surface and subsurface regions) selective heating the portion of sample using laser radiation. In addition, it is also a self quenching method where the mass of sample surrounding the laser material interaction volume rapidly extracts the heat, giving rise to cooling rates in the order of 10^3 - 10^5 K/s [1]. The process is highly controllable, rapid, and avoids bulk material heating for extended period associated with the conventional furnace treatment.

One of the important aspects of crystallization is the size of crystals formed, which critically influences mechanical, chemical, and functional properties and performances [64, 65]. Crystallization characteristics in the above described unconventional non-isothermal techniques are different compared to the conventional isothermal techniques. The crystallite sizes evolved during these unconventional processes are typically much finer. Therefore, emphasis has been given to explore the non-isothermal methods for crystallization of various metallic glasses [1, 28–30, 43, 71, 72].

The current work employs laser as a heat source for the crystallization of Fe-Si-B metallic glass. Previous studies from the present research group have indicated formation of nano crystals in the amorphous matrix upon laser treatments which led to substantial improvements in the soft magnetic performance of the material. The main focus of the work has been on crystallization under non equilibrium laser processing conditions as well as on effect of microstructure evolution on tensile behavior of laser treated Fe-Si-B metallic glass. In light of this and after discussing about effects of thermal energy, the following Section of the literature review has been dedicated to the mechanical behavior of the metallic glass based materials. It is worth noting here that a separate Section has been included to provide the information about Fe-Si-B metallic glass, the specific material under consideration of the present work.

2.3. Mechanical Behavior of Metallic Glasses

Metallic glasses on the account of their short range order structure posses a high strength of the order of few GPa irrespective of mode of loading and chemical composition [2, 73–78]. Absence of grains, grain boundaries, and other defects makes the deformation mechanisms in metallic glasses much different than the conventional crystalline structural materials. The metallic glasses have been reported to have strength closer to the theoretical strength values [26]. The model designed for theoretical strength by Orowan does not take into account the defects and imperfections within a material [79, 80]. The strength predicted by such a model is expressed approximately according to Eq. 2.3

$$\sigma_{theoretical} \approx \frac{E}{\pi} \tag{2.3}$$

That is, in absence of defects, a material would posses the strength which is approximately one third of it's Young's modulus. Considering the typical Young's moduli of 100-200 GPa, the expected strengths are $\sim$ 30-60 GPa. However, because of presence of defects (driven by thermodynamic stability), the usual strengths reported for conventional crystalline materials are of the order of 100-1000 MPa. Metallic glasses have the modulus values less than 100 GPa [25, 26]. Thus, estimated values of strength according to Eq. 2.3 are much smaller and hence the observed difference between calculated and experimental values of strength becomes smaller as well. Nonetheless, these values are of the order of few GPa and are much higher than actual strengths of the conventional structural materials. The structural differences amongst these two types of materials give rise to the differences in the corresponding response to the load. The following subsection provides information about features of deformation in metallic glass based materials and also provides key differences when compared to their crystalline counterparts.

2.3.1. Formation of Shear Bands

The absence of dislocations and crystallographic planes also leads to absence of mechanism to accumulate the macroscopic plastic deformation. Crystalline materials on the other hand, have a periodic structure on atomic level. The deformation happens by mechanisms of slip and twining. Dislocations form the key elements of deformation and controlling dislocation motion also results in controllable mechanical properties. Very common example of slip is FCC aluminum where {111} is the family of closed pack planes and <110> family of directions form closed pack directions lying in those planes. Dislocation motion and interactions primarily on these planes determines macroscopic response of a FCC material to applied load. The deformation is visually observable in the form of slip bands. In case of metallic glasses, deformation occurs in a very localized manner. It has been proposed that, on application of load, a small volume of material gets activated and undergoes shear. This volume is termed as shear transformation zone (STZ) [81] which are reported to be of having average diameter of around 1 nm [9]. Formation of STZs is illustrated in Fig. 2.10 [8]. On comparing metallic glasses with crystalline materials, STZs are analogues counterparts of dislocations in metallic glasses. Collective activation of STZs on application of applied load leads to formation of a band like volume of material undergoing localized shear deformation which is called as shear band (Fig. 2.11 [9]). Shear bands are similar to the slip in crystalline materials. The key differences between crystalline and amorphous materials have been summarized in Fig. 2.12. Shear bands can easily nucleate at stress concentrators such as defects and notches within the material because of high value of stress associated with them. Shear bands are soft as compared to surrounding matrix because of the deformation happening within them. They can rapidly propagate throughout the cross-section of the material under the applied load and may lead to catastrophic failure without any noticeable macroscopic plastic deformation.

2.3.2. Dependence of Response to Load on Crystallizations and Loading Directions

The mechanical behavior of amorphous materials and their composites with crystalline reinforcements is governed mainly by the movement of shear bands [9, 12, 82]. As discussed, shear bands are basically the soft volume of a material undergone localized plastic shear deformation during loading [9]. Thus, controlling the nucleation and propagation of shear bands determines the macroscopic mechanical response of metallic glasses and their

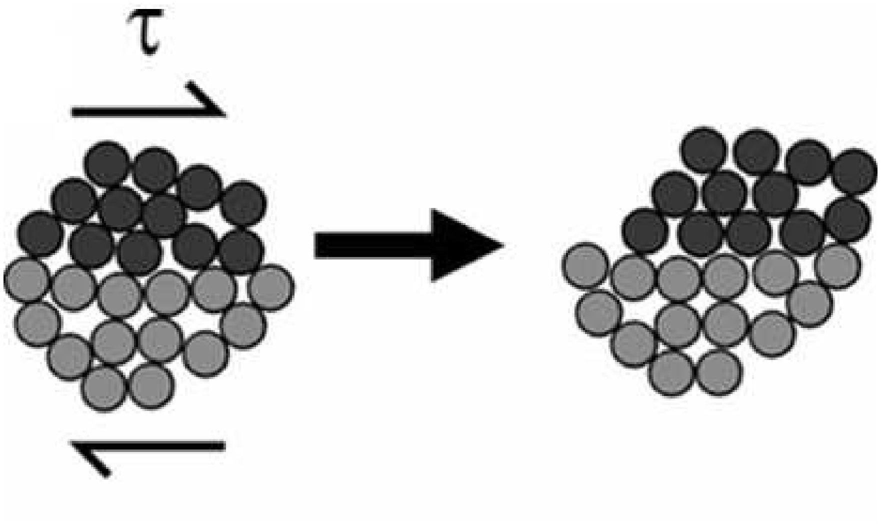

FIGURE 2.10. Formation of shear transition zones on application of stress within a metallic glass [8].

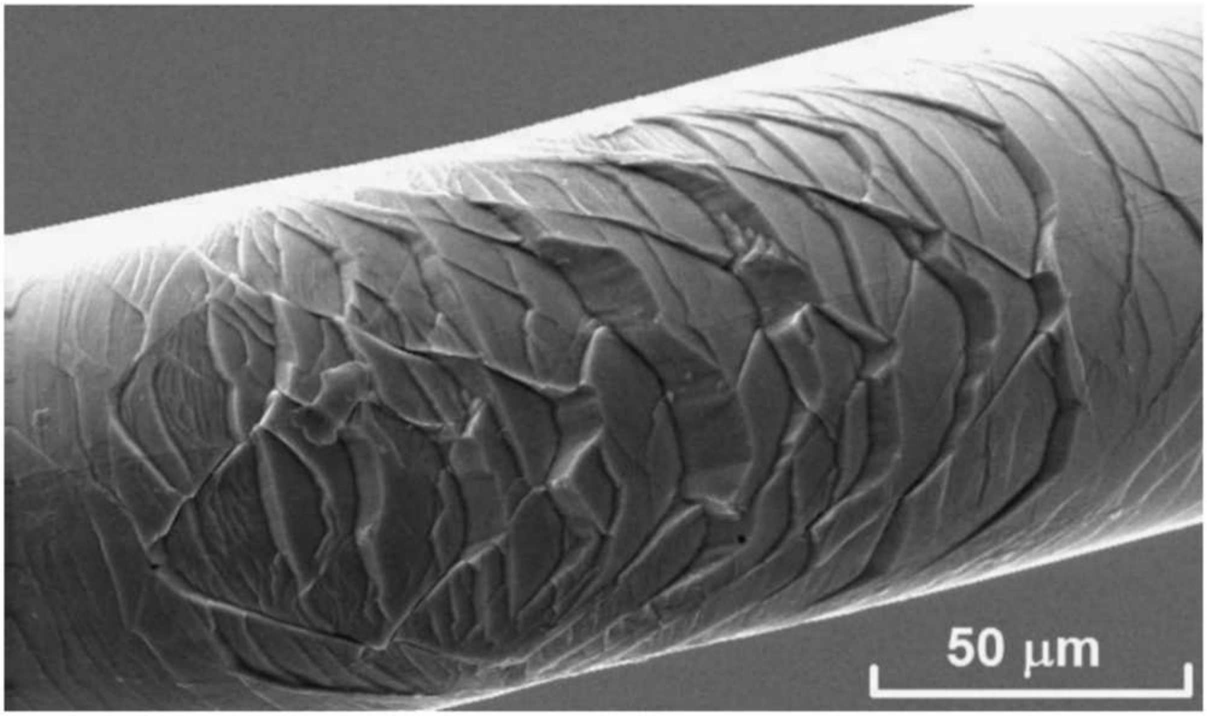

FIGURE 2.11. Surface markings caused by shear bands, observed on the tensile side of a bent wire (diam. 100 mm) of a $[(Fe_{50}Co_{50})_{75}B_{20}Si_5]_{96}Nb_4$ (in at.%) metallic glass [9].

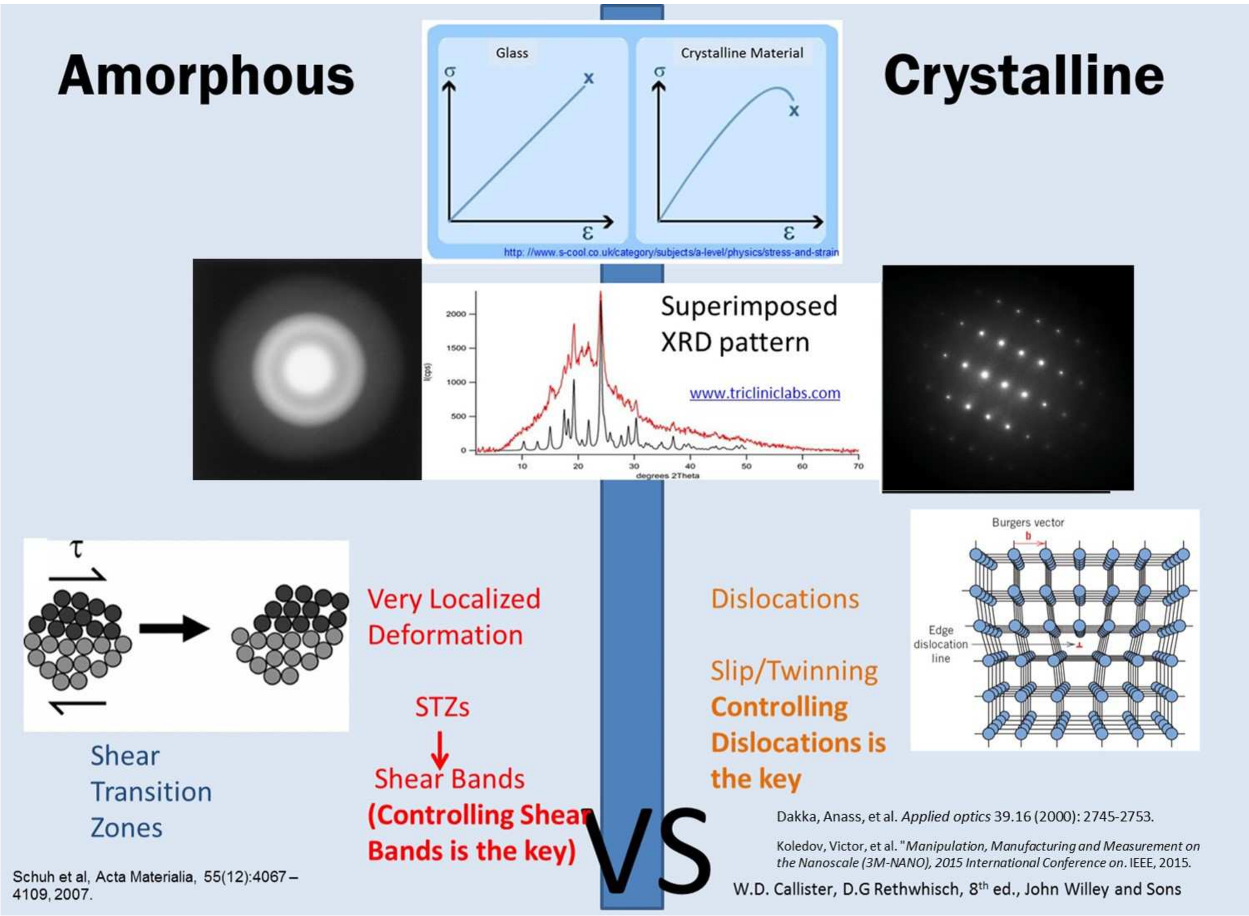

Figure 2.12. Schematic illustrating differences in tensile stress strain behavior of amorphous and crystalline materials along with the key microstructural differences leading to different deformation mechanisms. The composite has been constructed from references [10–15].

composites. It has been reported that crystallization of these materials can either results in ductility improvement or severe embrittlement [12, 25, 26, 83]. These two opposing effects depend on the method of loading (tensile or compressive) and the types of phases formed due to crystallization [12, 26]. Applying a compressive constrained loading to these materials results in the formation of multiple shear bands which leads to macroscopic plastic deformation. This is attributed to confined nature of the test along with the frictional forces generated at the grip-sample interface [26]. Such a loading scenario tends to exert closing stresses on shear bands leading to their multiplication throughout the cross-section of the sample. On the contrary, in tensile loading, often times a single shear band propagates through the entire cross section of the specimen leading to a brittle failure [25, 26].

Furthermore, while considering the role of crystalline phases, their volume fraction and the nature (brittle or ductile) considerably affect the mechanical properties [12, 25, 26]. Two potential roles can be assigned to these phases. Depending upon their nature, they may serve as a hard interface with the amorphous matrix initiating the failure or they may pose a barrier for the movement of shear bands and act as nucleation sites for new shear bands. The latter results in a measurable plastic deformation independent of the loading direction. Thus, even though crystallization may be necessary for improving functional properties such as soft magnetic properties in case of Fe based metallic glass [1, 27, 30, 43, 71] the microstructural investigation and control becomes critical to ensure mechanically reliable performance. On the other hand, as stated earlier, crystallization can serve as the barrier to shear band movements and further nucleate new shear bands leading to macroscopic plasticity in metallic glasses [6, 25]. Thus, it is clear from the discussion so far that metallic glasses differ drastically from their crystalline counter parts in terms of their mechanical behavior. Added to this list is another unique feature of temperature rise in the shear bands which leads to formation of a characteristic vein morphology as discussed in the following subsection.

2.3.3. Temperature Rise in Shear Bands and Fracture Behavior

Another interesting feature of the mechanical response of metallic glasses is the temperature rise within the shear band region during loading. Temperatures as high as few thousand degrees centigrade have been reported depending upon the composition of the metallic glass [9, 84]. One of the early evidences of temperature rise was presented and quantified by Lewandowski and Greer in the case of Zr based metallic glass using a fusible coating method (Fig. 2.13 [16]). Atomistic simulations have also suggested increase in temperature of the shear band region [85]. As a matter of fact, the appearance of vein like features on the fracture surface of the metallic glass suggests localized plastic flow in the fractured region of the metallic glass due to combined effect of loading and the temperature rise within the shear bands. For example, during tensile loading, a single shear band extends at 45° to the loading axis throughout the cross section [26]. This results in formation of shear offset on the surface of the sample (Fig. 2.14 a). As the shear band heats up the free volume within the shear band increases leading to coalescence of voids giving rise to crack nucleation [86]. Upon fracture, a characteristic vein pattern appears on the surface indicative of signs of localized plastic deformation and temperature rise (Fig. 2.14 b). The origins of such a vein pattern have been reported to be in localized increase in viscosity as the temperature increases within the shear bands. This generates the negative pressure effects as a result of balance between the surface tension of the viscous fluid (Fig. 2.15 a) [19, 87]. The localized meniscus in the low viscosity regions near the crack tip generated from the shear bands is sensitive to the movement of crack. Any perturbation in the meniscus normal to the crack propagation will make it unstable. A perturbation of length λ greater than the critical length λ_c can grow to develop a finger type shape (Fig. 2.15 a). Collective growth of these perturbations leads to formation of characteristic vein pattern at the fracture surface (Fig. 2.15 b).

The temperature plays a key role in formation of low viscosity zones. This temperature rise within the shear bands is expressed mathematically according to Eq. 2.4 [16, 88]

$$\Delta T = \left(\frac{H}{\rho C_p \sqrt{\pi \alpha}}\right) \frac{1}{\sqrt{t}} exp \left(\frac{-y^2}{4 \alpha t}\right) \tag{2.4}$$

where ΔT is the rise in temperature, C_p is the specific heat, H is the heat content within the shear band region, ρ is the density, t is the time, α is the thermal diffusivity, and y is the distance from the center of a shear band.

Thus, it is clear that temperature rise inevitably occurs during mechanical loading and fracture of the metallic glasses. Such a temperature rise in turn intuitively may lead to crystallization in metallic glasses. However there are contradicting reports suggesting both the presence [88, 89] and absence [90] of crystallization in the fractured region. This points towards the dependence of such a crystallization on factors such as chemical composition and strain rate apart from temperature rise. Furthermore, it becomes important to investigate behavior of metallic glass with and without presence of preexisting crystallization which is one of the motivations for the current work.

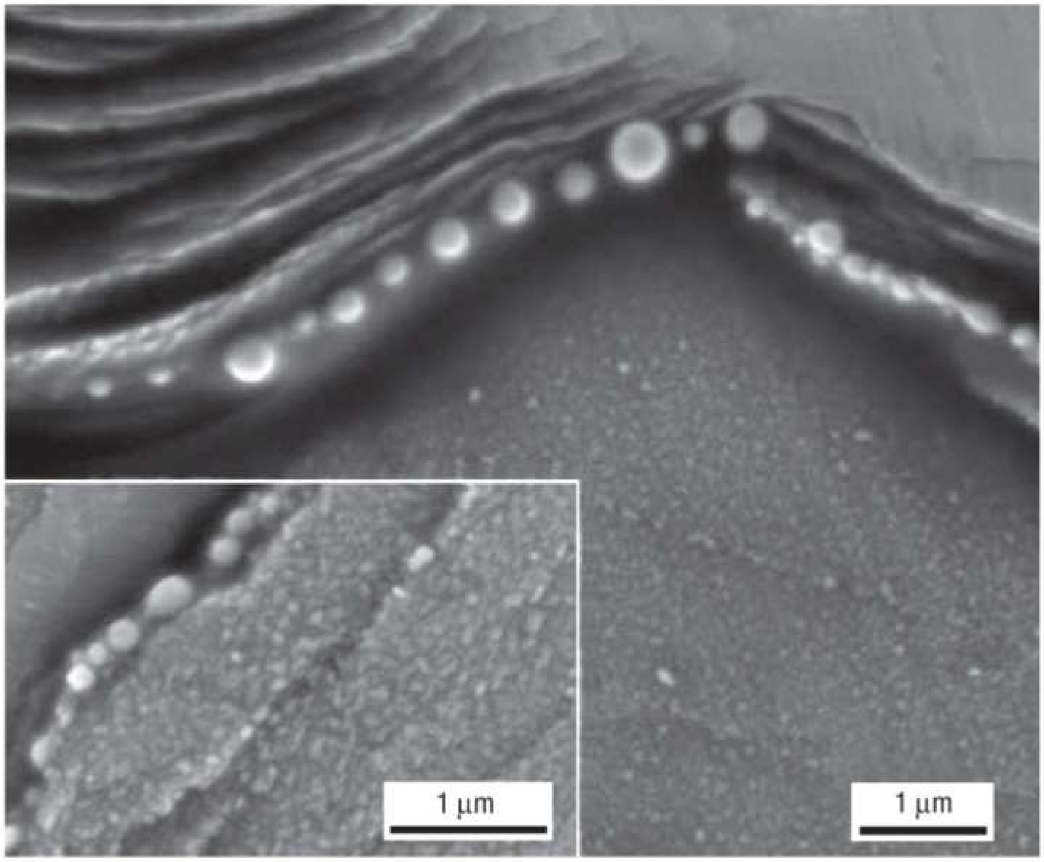

Figure 2.13. Melting of tin coating on the Zr-based metallic glass upon fracture [16]. This is one of the first experimental evidences about temperature rise during fracture of a metallic glass.

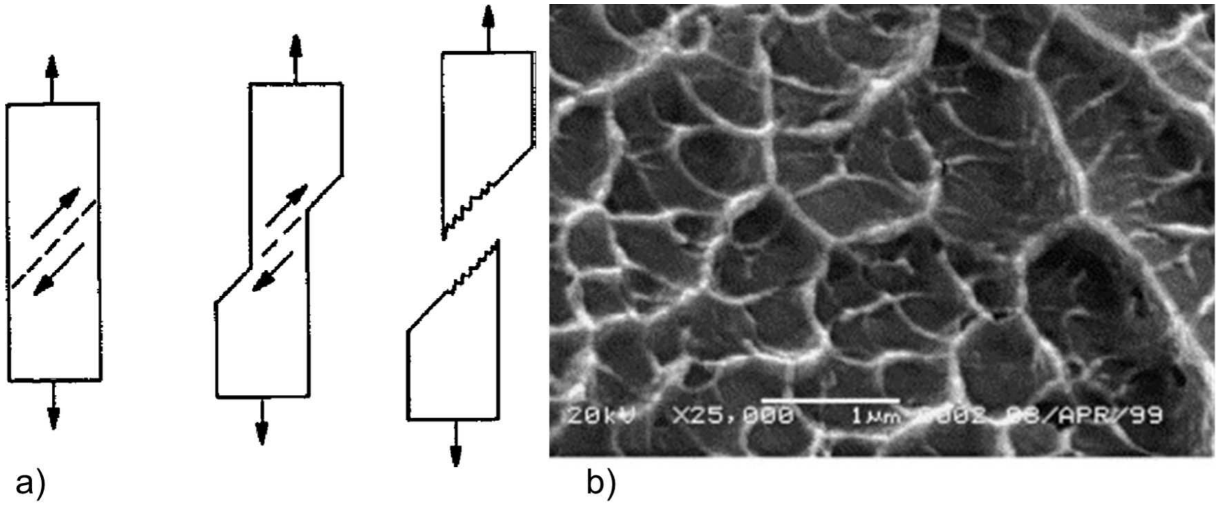

Figure 2.14. Set of figures illustrating (a) formation of shear offset during propagation of shear band in the cross-section of the sample [17] and (b) appearance of vein pattern on the fracture surface of the metallic glass [18].

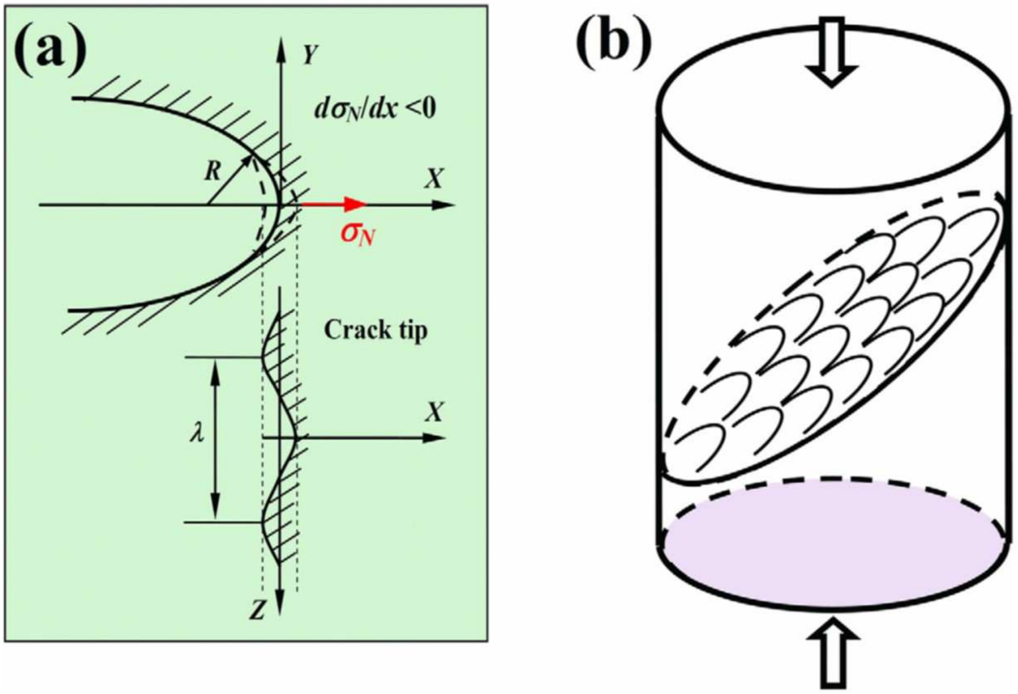

FIGURE 2.15. (a) Instability of the fluid meniscus in the crack tip [19] (b) Illustration of the catastrophic fracture process [20]. Where $\frac{d\sigma_N}{dz}$ is the pressure gradient with respect to normal stress σ_N and R is the radius of curvature of the meniscus.

Having discussed topics such as metallic glasses, effects of thermal energy on metallic glasses, and mechanical behavior of metallic glasses; the current Chapter switches gear and now provides a brief review about the material under consideration for the current work, i.e., Fe-Si-B metallic glass. Information about previous investigations from the current group has been provided which sets the basis for the research problem for the current work.

2.4. Brief Overview of Material and Processing Method Under Consideration

The current work focuses on laser processing of Fe-Si-B metallic glass. It forms the part of ongoing efforts in the present research group to understand the crystallization behavior, microstructure evolution, magnetic performance, and mechanical behavior upon laser treatment of Fe-Si-B metallic glass. The choice of laser as a processing tool in the particular case of metallic glasses/amorphous material is based on various advantages offered by the laser technique such as non contact processing, no need of vacuum for instrument operation, ease of automation, high controllability, site specific heating, and chemical cleanliness [23, 30, 42, 71]. Furthermore, laser treatment also avoids harmful effects associated with the conventional methods such as oxidation and uncontrolled grain growth. Laser thermal treatment is capable of instantaneously spatially (surface and subsurface regions) selectively heating the portion of sample using laser radiation. This leads to a self quenching effect where the mass of the sample surrounding to the laser material interaction volume rapidly extracts the heat, giving rise to cooling rates on the order of 10^3 - 10^5 K/s [1]. This becomes critical in the case of selective surface crystallization of metallic glasses wherein control of crystallite/grain size evolved and area of crystallization is critical. In light of the advantages offered by the laser, it was chosen as the processing tool for this ongoing investigation on Fe-Si-B metallic glass.

Fe-Si-B-based metallic glasses have gained popularity as a result of their superior soft magnetic performance which is5 far better than their conventional crystalline counterparts [1, 91, 92]. It has been reported that the controlled crystallization of these glasses can result in optimal functional properties [1, 93]. Partial crystallization results in evolution of a composite microstructure consisting of crystalline pockets within the glassy matrix. Such a microstructure has been reported to improve magnetic performance of partially crystallized Fe-Si-B metallic glass by resulting in improved saturation magnetization and reduced coercivity (Table 2.1) [1, 27, 43, 44, 71, 94]. Furthermore, it was also pointed out that magnetostrictive effects (the undesired changes in shape of a magnetic material upon undergoing the process of magnetization [95]) would be minimized in such a partially crystallized Fe-Si-B metallic glass because the magnetostrictive vectors of crystalline and amorphous phases have opposite directions [96].

Table 2.1. Summary from the Previous Work of Magnetic Properties of Fe-Si-B Metallic Glass in Various Conditions [1]

Property	Furnace Annealing	Laser Treated	As received
Coercivity (Oe)	64	37	0.45
Saturation Magnetization (emu/g)	155	175	136

However, apart from improvements in soft magnetic properties, a mechanical reliability is also critical from practical application point of view. As an example, Fe-Si-B metallic glasses have been considered attractive material for the transformer core application [97]. The transformer core is subjected to mechanical loading and thermal stresses during the course of operation and catastrophic events such as a current surge may lead to permanent failure [98–100]. Hence, along with improved magnetic properties, a good mechanical strength is critical from this application point of view. Therefore, an understanding of the evolution of crystallization and microstructure during laser treatments is important. Moreover, understanding of structure-mechanical properties relation and effect of loading on structural changes also becomes critical from the performance point of view. This forms the basis of the problem statement for the current work. The following Chapter goes into the details of the experimental and computational methodologies opted in the current work. This is proceeded by Chapters discussing the important findings and conclusions of the current work.

CHAPTER 3

EXPERIMENTAL AND COMPUTATIONAL PROCEDURES

3.1. Material

Commercially available iron based metallic glass ribbons (Metglass$^{\text{TM}}$) with the average composition of 85Fe-10Si-5B in atomic percent and the thickness of 23 microns were used in the current work. This particular composition has been popular for applications such as transformers, high frequency inductors, and motors as a result of superior soft magnetic properties [101]. Previous research work from our research group focused on the same material with an emphasis on spatially controllable crystallization and its effects on soft magnetic properties [1, 23, 30, 43, 44, 61, 94]. A significant improvement in magnetic properties upon laser-induced crystallization was reported. The focus of current work was on effect of thermokinetic conditions during laser treatments on crystallization and in turn on tensile properties with an aim to develop functionally better and mechanically reliable Fe-Si-B metallic glass based soft magnetic materials.

Rectangular foil samples of the length of 90 mm and the width of 12 mm were cut using a carbide blade from the sheet of the metallic glass. The central portion of length of 50 mm was regarded as the gage length during the tensile test (Fig. 3.1). Grip regions of 2 cm on both sides of the foil were utilized to hold the samples in the grips during tensile tests. The central was subjected to a single linear laser track treatment in the middle (Fig. 3.1). Detailed description about experimental setup during laser thermal treatments, range of laser processing parameters explored during current work, and tensile testing have been provided in the following Sections.

3.2. Laser Thermal Treatments

A continuous Nd-YAG laser of 1064 nm wavelength, 0.6 mm beam diameter on the sample surface, and input power of 100 W was employed for this purpose. The sample was treated for a single linear laser track (Fig. 3.2) in the central region. The scanning speeds

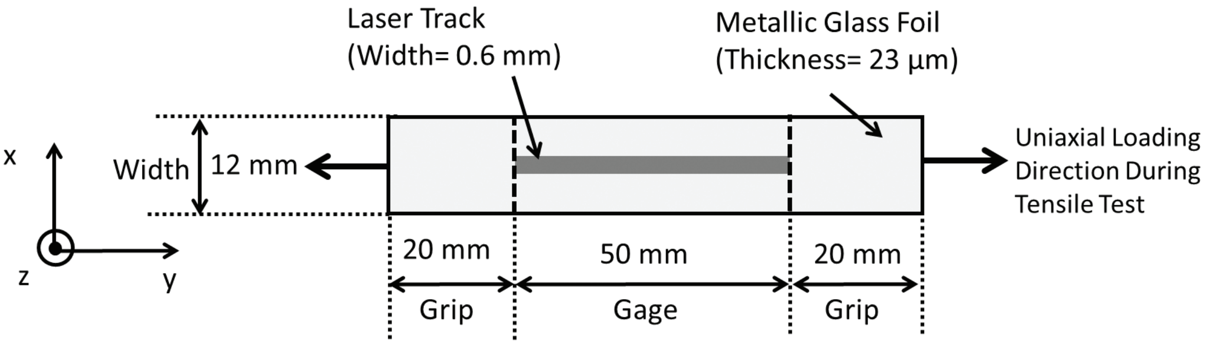

FIGURE 3.1. Schematic of the Fe-Si-B metallic glass foil used in the current work. Features such as region subjected to laser thermal treatment and griping areas during mechanical tests have also been shown.

were varied to get various laser fluences on the sample surface (F) expressed in Eq. 3.1

$$F = \frac{P_0 t_0}{A} \tag{3.1}$$

where P_0 is the input laser power, A is the cross sectional area of the laser beam, t_0 is the beam residence time as expressed in Eq. 3.2

$$t_0 = \frac{d}{V} \tag{3.2}$$

where d is the laser beam diameter and V is the laser beam scanning speed.

The initial intent of the study was to understand the crystallization of the Fe-Si-B metallic glass under the non equilibrium thermokinetic conditions imposed during laser thermal treatments. The laser beam scanning speeds chosen for this set of experiments were in the range of 235-350 mm/s (Table 3.1). These conditions were finalized after number of trials wherein speeds higher than 350 mm/s did not indicate any crystallization in X-ray diffraction (XRD) analysis, whereas speeds lower than 235 mm/s melted the foil. On the other hand, for the studies on tensile behavior, additional laser beam scanning speeds in the range of 350-550 mm/s were introduced to cover the structural changes such as structural relaxation (Table 3.2).

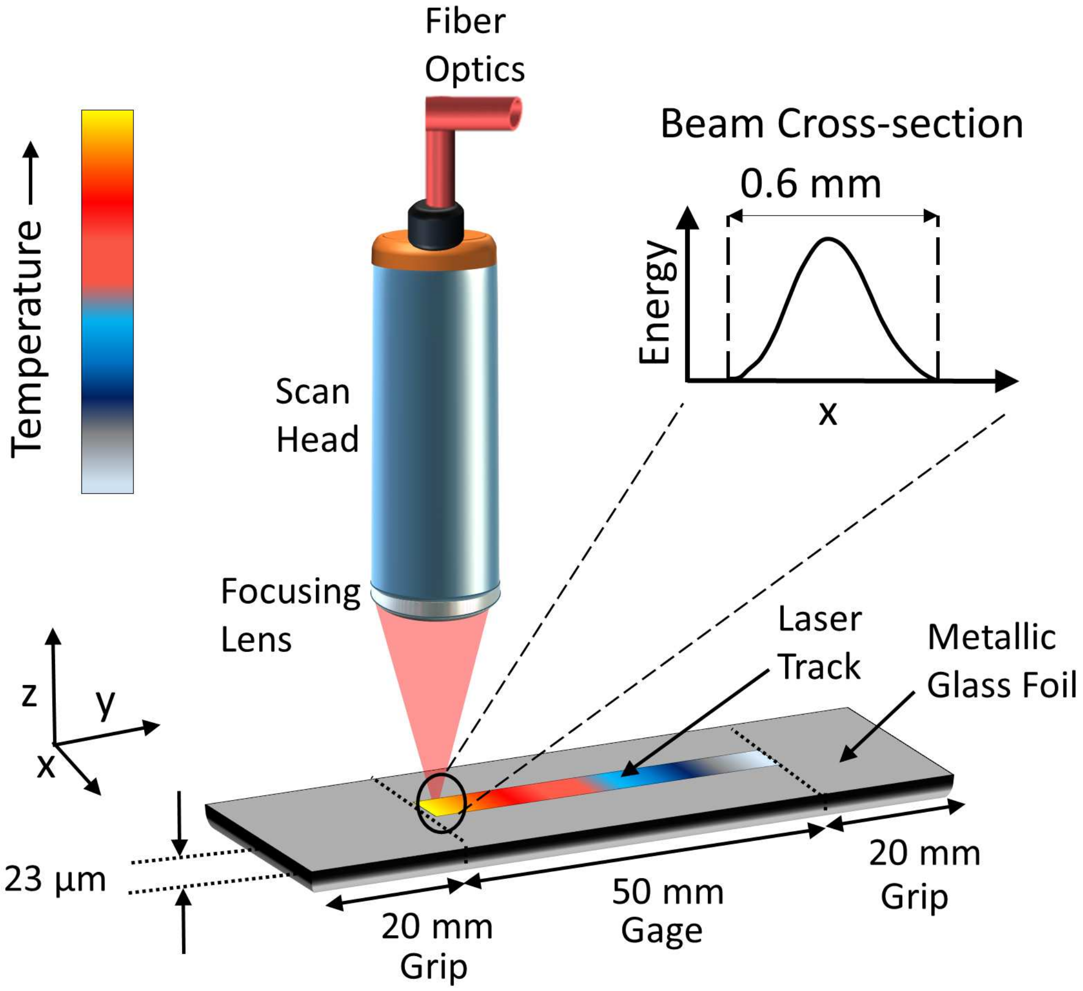

FIGURE 3.2. Schematic of setup during laser thermal treatments of Fe-Si-B metallic glass.

TABLE 3.1. Laser Processing Parameters Employed during Crystallization Studies

Laser Power (P_0) W	**Scanning Speed (V)** mm/s	**Laser Fluence (F)** J/mm^2
100	235	0.90
100	250	0.85
100	275	0.77
100	300	0.70
100	325	0.65
100	350	0.60

Table 3.2. Laser Processing Parameters Employed during Tensile Behavior Studies

Laser Power (P_0) W	**Scanning Speed (V)** mm/s	**Laser Fluence (F)** J/mm^2
100	550	0.39
100	500	0.42
100	450	0.47
100	440	0.48
100	430	0.49
100	420	0.51
100	410	0.52
100	400	0.53
100	350	0.61
100	300	0.71

3.3. Identification/Characterization of Crystallization and Phase Evolution

3.3.1. X-ray Analysis

XRD was carried on Rigaku Altima diffractometer for detecting crystallization within laser treated volume with Cu K_α radiation (0.154 nm wavelength), step size of 0.025°, and a scan speed of 2 °/minute. Thin films module with Z-omega alignment feature of the Rigaku XRD setup software was utilized for this purpose.

3.3.2. Calorimetric Analyses

In order to gain some insight about fraction of crystallization under non-isothermal treatment, differential scanning calorimetry (DSC) experiments were performed on laser treated region.The samples were carefully cut and weighed on a sensitive Secura^{TM} semi-microbalance prior to the experiments. DSC runs were conducted on Perkin Elmer calorimeter at the heating rate of 20 K/min and alumina as the reference material. Carefully cleaned alumina crucibles were used to hold the samples. Ar was used as an inert gas inside the sample enclosure furnace during all the runs.

3.3.3. Resistivity Measurements

The physical transformations such as structural relaxation and crystallization were further investigated via measurement of the electrical resistivity of laser treated regions of the foils. These measurements were performed within the voltage range of 0.2-1 V using a four point probe method as a function of laser fluence. The sample dimensions and slope of voltage-current plots were measured carefully for the determination of the resistivity of the samples.

3.3.4. Electron Microscopy [1]

The microstructure analyses of laser treated regions were further performed on selective samples using FEI Tecnai F20 field emission gun transmission electron microscope (TEM) operated at 200 keV. Foils for TEM analyses were prepared using a Dual-Beam^{TM} focused ion beam scanning electron microscope (FIB/SEM). Selected area diffraction (SAD) patterns corresponding to the various laser treated foils were obtained and analyzed to get an insight into phase separation and types of the crystallized phases. The multi beam bright field images as well as dark field images were analyzed to determine the average grain size using ImageJ software.

3.4. Computational Model [2]

Development of various temperature fields during heating and cooling stages of different applied laser fluences are expected to generate a host of microstructures in metallic glass. In more specific, the imposed heating and cooling rates, along with the values of maximum (peak) temperatures attained and the time interval above the crystallization temperature determine the characteristics of crystallites evolved. In order to obtain the thermal history developed during laser processing for each set of parameters of laser treatment, a COMSOL^{TM} Multiphysics® based three dimensional finite element (FE) heat transfer analysis model was developed. The FE model involved a geometrical simulation of the Fe based amorphous ribbon in a rectangular block of 50 x 1.2 x 0.023 cm^3 in dimensions

---

[1] The content of this section has been previously published in author's publication:
(i) Joshi, Sameehan S., et al. "Tensile behavior of laser treated Fe-Si-B metallic glass." Journal of Applied Physics 118.16 (2015): 164904. (Reproduced with permissions from AIP Publishing LLC)

[2] The content of this section has been previously published in part in author's publication: Joshi, Sameehan S., et al. "Dynamic crystallization during non-isothermal laser treatment of Fe–Si–B metallic glass." Journal of Physics D: Applied Physics 48.49 (2015): 495501. (Reproduced with permission from IOP Publishing Ltd.)

(Fig. 3.3). It was meshed by a physics-controlled extra fine type of mesh (with mesh edge dimension of 0.1 mm).

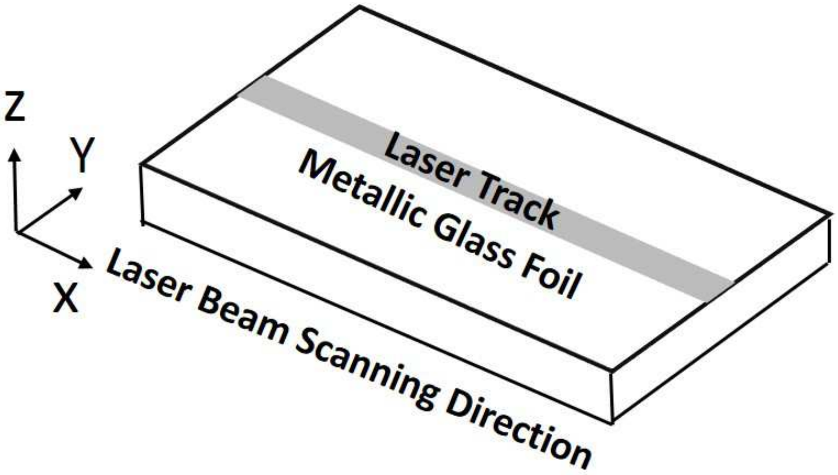

Figure 3.3. Schematic of geometry of model used in current study.

The heat transfer module of COMSOL^{TM} adopted in the present work is based on the fundamental principle of conservation in heat transfer, and in case of a three dimensional heat transfer it is expressed below in Eq. 3.3

$$\rho C_P \left(\frac{\partial T}{\partial t}\right)_{(x,y,z)} = k' \left[\left(\frac{\partial T}{\partial x}\right)_{(y,z.t)} + \left(\frac{\partial T}{\partial y}\right)_{(x,z.t)} + \left(\frac{\partial T}{\partial z}\right)_{(x,y.t)}\right] \tag{3.3}$$

where ρ is the density, C_P is the specific heat capacity and k' is the thermal conductivity of the material. Thermal conductivity for the present material is reported to be 9 W/mK [101] which is close to polycrystalline Fe-Si alloys [102]. The expression in Eq. 3.3 actually provides the transient temperature field developed within the sample while the laser beam is moving along x-axis. The corresponding three dimensional heat flux ($Q_{x,y,z}$) generated by Gaussian laser beam is expressed in the Eq. 3.4.

$$Q_{x,y,z} = \frac{P_0}{A} * exp\left[-\frac{(x - Vt)^2 - y^2}{2S_D^2}\right] \tag{3.4}$$

where t is the time, and S_D the standard deviation of Gaussian beam.

The boundary conditions assigned in the model represent the different mechanisms of heat transfer during heating and cooling on each surface . On the top surface of the ribbon a general inward heat flux boundary was set. Radiation and convection happening simultaneously carried the heat out of the top surface as expressed in Eq. 3.5

$$-k'\left[\frac{\partial T}{\partial x}+\frac{\partial T}{\partial y}+\frac{\partial T}{\partial z}\right]=Q_{x,y,z}-\epsilon\sigma[T^4-T_0^4]-h[T-T_0] \tag{3.5}$$

where ϵ is the emissivity, h is the convective heat transfer coefficient, σ is the Stephen Boltzman's constant and T_0 is the ambient temperature. Heat transfer coefficient has been reported to have value in tens of W/m^{2}K [103–105] for natural convection due to the surrounding air at ambient temperature, therefore it was set as 10 W/m^2/K in current FE model. Emissivity depends on surface condition of the sample and has been reported to vary from 0.07 to 0.79 for iron based material [106]. In the present case, it was chosen as 0.7 which is typical for unpolished surfaces. On rest of the surfaces, the boundary conditions of convection and surface to ambient radiation were chosen and they are described by equation 3.6 as

$$-k'\left[\frac{\partial T}{\partial x}+\frac{\partial T}{\partial y}+\frac{\partial T}{\partial z}\right]=\epsilon\sigma[T^4-T_0^4]+h[T-T_0] \tag{3.6}$$

The values of laser processing parameters and thermo-physical properties used in computational simulations of current work are presented in Table 3.3. The thermo-physical properties are constant room temperature values as the temperature dependent properties for this material system are not available in the open literature. Moreover, laser-material interaction is a complex process involving transition of material through several phases (eg. crystallization, phase evolution, and melting in the current case) in extremely short duration (∼ms) of the process. Along with phase changes, the laser based surface treatment may also involves additional physical phenomena such as evolution of surface roughness and generation of material plume/plasma on the substrate surface. The occurrence of multiple physical phenomena in such short duration makes it, if not impossible, very difficult either to conduct in-situ experimental measurements or design a computational model for obtaining temperature dependent thermophysical properties for any material system. In light this, it was reasonable to assume the room temperature thermophysical properties during the current

Table 3.3. Thermophysical and Processing Parameters Employed in FE Model

Thermophysical Parameters		
Symbol	**Description**	**Value**
ρ	Density	7180 kgm^{-3} [107]
C_P	Specific heat	500 J(kgK)$^{-1}$ [108]
k'	Thermal conductivity	9 W(mK)$^{-1}$ [101, 102]
h	Convective heat transfer coefficient	10 W(m^{2}K)$^{-1}$
ϵ	Emissivity	0.7 [106]
σ	Stefan-Boltzmann constant	5.67 x 10^{-8} W(mK^4)$^{-1}$
Processing Parameters		
Symbol	**Description**	**Value**
P_0	Laser power	100 W
L	Length of the laser track	50 mm
t	Time of processing	L/V s
d	Laser beam diameter	0.6 mm
A	Laser beam cross sectional area	$\pi d^2/4$ mm^2
S_D	Standard deviation of Gaussian beam	0.2 mm

computational modeling efforts. These computational simulations were primarily employed to generate temperature as function of time and corresponding heating and cooling rates during laser thermal treatments and correlated them with the crystallization and crystal growth behavior under various laser fluences used in the present work.

Finally, the heat of crystallization was not considered during the computational thermal modeling. The total value of heat of crystallization for the as cast foil estimated with the aid of DSC analysis was 61 J/g (Fig. 3.4). On the other hand, in case of laser processing the heat input during the residence time of the beam was of the order of thousands of J/g (in the range of 3633-5450 J/g for the laser fluence range of 0.60-0.90 J/mm^2 employed in the present work). These values of heat input are several orders of magnitude higher than the heat evolution during crystallization (Fig. 3.4). Thus, the small amount of heat of crystallization (61 J/g) compared to large amount of laser heat input (3633-5450 J/g) is likely to assert minimal or no influence on the thermal conduction, radiation, and convection in metallic glass during computational thermal modeling. In view of this it was reasonable to not consider the heat of crystallization during computational thermal modeling.

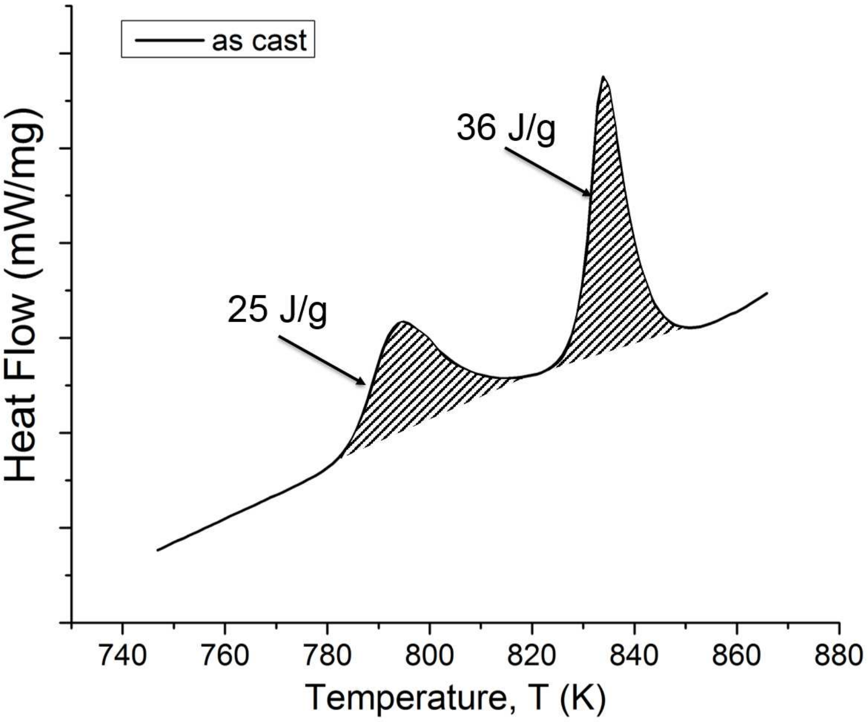

FIGURE 3.4. Differential scanning calorimetry curve showing heat of crystallization for as cast Fe-Si-B metallic glass foil.

3.5. Tensile Testing [3]

The effect of different laser treatments on the overall tensile behavior was investigated using a hydraulically driven Instron^{TM} universal testing machine. Prior to the testing, edges of the foils were polished using 1200 SiC paper so as to avoid effect of preexisting irregularities on the edges. The 50 mm long laser treated region was subjected to a uniaxial tensile loading at the strain rate of 10^{-3}/s following American Society for Testing and Materials (ASTM) Standard #E345 (Standard Test Methods of Tension Testing of Metallic Foil) guidelines, while the untreated areas of 20 mm on each end of the sample served as the grip regions (Fig. 3.1). Elongation at fracture and ultimate tensile strength (UTS) values were obtained from the extracted engineering stress-strain data from the tensile tests. At least four samples were tested for each laser processing condition in order to ensure repeatability of the results.

---

[3] The content of this section has been previously published in author's publication:
(i) Joshi, Sameehan S., et al. "Tensile behavior of laser treated Fe-Si-B metallic glass." Journal of Applied Physics 118.16 (2015): 164904. (Reproduced with permissions from AIP Publishing LLC)

3.6. Optimization [4]

Response Surface Method (RSM) was employed to determine an optimal laser processing condition based on combination of lowest electrical resistivity and highest UTS. A one factor design within StatEase ^{TM} software (version 9) package was chosen for the optimization study. The RSM developed predictive models for each response (in present case UTS and electrical resistivity). Each response was combined into an objective function called desirability, which was then optimized by univariate techniques. By application of desirability functions, the optimum combinations of the electrical resistivity and UTS can be determined for laser processed Fe-Si-B metallic glass. RSM consists of three basic steps:

- Develop predictive models for the responses of UTS and electrical resistivity. Fit each set of response data with an appropriate mixture model using least squares regression.
- Combine all responses in to one overall desirability function by (1) establishing specifications for each response, (2) transforming each response to a desirability scale that ranges from zero, for undesirable outcomes, to one, for perfectly desirable results, and (3) combining the individual desirabilities in to one overall function by use of the geometric mean.
- Find the maximum value of combined desirability, the corresponding impact factors, and value for each responses in interest.

The steps above are sequentially shown in the form of a flow diagram in Fig. 3.5. In present case, a combination of laser processing parameters (laser power and scanning speed) which would lead to a combination of maximum UTS (to ensure mechanical durability) and lowest resistivity (indicating crystallization) was considered an optimum processing condition. The results were obtained in terms of predicted vs actual material properties (UTS and electrical resistivity) plots and desirability vs laser processing condition (laser fluence and

---

[4] The content of this section has been previously published in author's publication: Joshi, Sameehan S., et al. "Optimization of laser thermal treatment of Fe–Si–B metallic glass." Journal of Manufacturing Processes 24 (2016): 31-37. (Reproduced with permission on behalf of The Society of Manufacturing Engineers from Elsevier Ltd.)

scanning speed) to further have an idea about optimum processing condition. The optimum condition was decided by setting the lowest electrical resistivity to assure crystallization and highest UTS value for superior functional and structural properties. Various functions were examined for curve fitting the variation in UTS and electrical resistivity. The square root function for resistivity and Logit function for UTS provided the best possible fit with respect to R^2 values, there was no physical significance in particular.

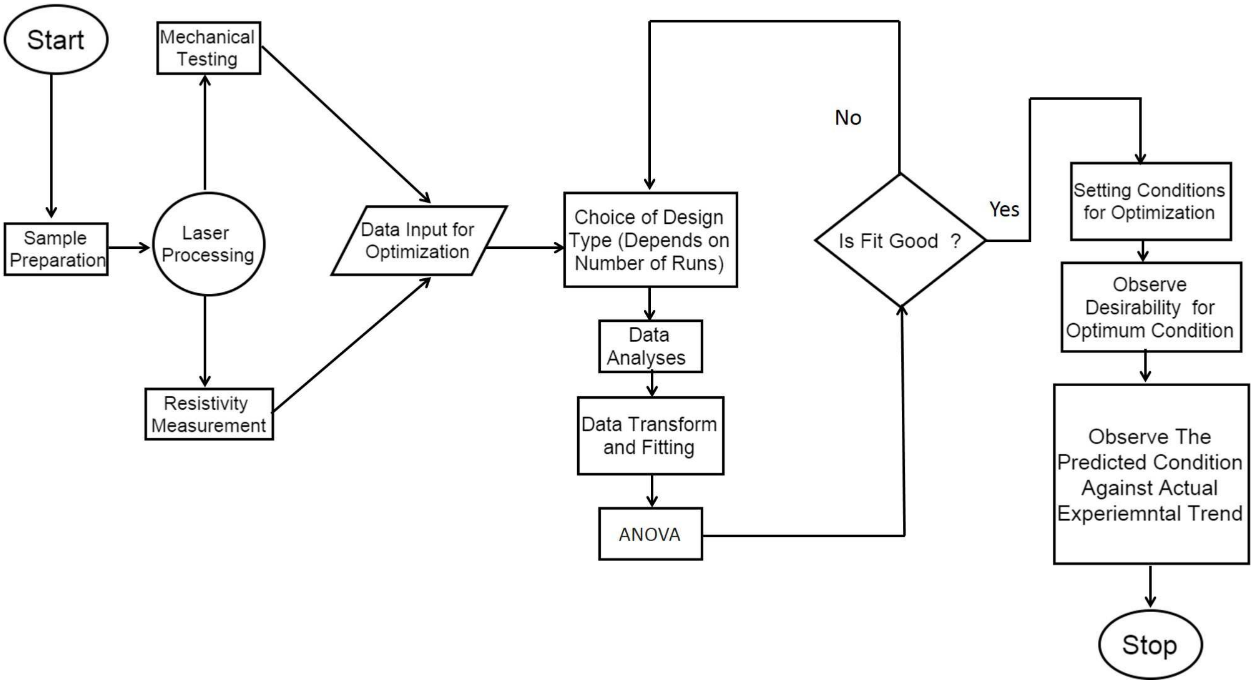

FIGURE 3.5. Flow diagram for experimental procedures and subsequent statistical optimization study.

3.7. Fractography [5]

Fractographic observations of the tensile tested samples were carried out with the aid of electron microscopy. The current section goes into the strategies followed in experimental setup and microscopy techniques to extract the information about fracture surface.

---

[5] The content of this section has been previously published in author's publication: Joshi, Sameehan S., et al. "Crystallisation behaviour during tensile loading of laser treated Fe–Si–B metallic glass." Philosophical Magazine 97.7 (2017): 497-514. (Reproduced with permission from Taylor & Francis.)

3.7.1. Observations of Fracture Surface Morphology

The primary observations of the fractured surface such as morphological (surface relief) features were made by FEI ESEM scanning electron microscope (SEM). The fractured metallic glass foils were held in a special clip type holder to ensure a firm hold and vibration free observations of the fracture surface. The SEM was operated at the voltage of 15 keV. Surface sensitive Everhart-Thornley secondary electron detector was employed for SEM imaging in order to capture the features of fracture surface topography. The SEM fractrographs were analyzed using linear intercept method to determine the average measurement of features such as vein spacing and thickness chevron ridges using linear measurement tool of the ImageJ software (developed by National Institute of Health, USA). As the veins appeared in the form of a mesh of polygons in the two-dimensional field of view of SEM micrograph, linear intersections across the polygon in at least eight directions using linear measurement tool of the ImageJ software were taken and presented as a mean value. The procedure was repeated for at least 20 other polygons within the field of view of the same SEM fractrograph and presented as a mean value with the standard deviation as the vein spacing. The thickness of chevron ridges was measured at various locations along the length of each individual ridge using the linear measurement tool of the ImageJ software. At least 10 ridges were measured in this manner in the field of view of a SEM fractograph and was reported as an average value with the standard deviation.

3.7.2. Site Specific Transmission Electron Microscopy

Effects of the tensile loading on a laser treated Fe-Si-B metallic glass such as microstructural features (crystallization and grain deformation) after fracture were observed using transmission electron microscope. Site specific TEM samples were prepared from the fractured region and a location away from the fracture using a Dual-Beam$^{\mathrm{TM}}$ focused ion beam scanning electron microscope (FIB/SEM) technique as indicated in Fig. 3.6. The final thinning of the samples was carried out using low energy beam (5 kV) at a low beam incidence angle to assure no microstructural changes were induced during the sample preparation process. Notably, the TEM foils were lifted out from the region perpendicular to the surface of the samples within the thickness in both non-fractured and fractured samples for consistency (Fig. 3.6).

The FIB lift out samples were then observed using FEI Tecnai F20 field emission TEM operated at 200 keV. The selected area diffraction (SAD) patterns were captured to analyze the phases present/evolved in various regions of the sample. The multi beam bright field (BF) images as well as dark field (DF) images were recorded. To determine the average crystallite/grain size using linear intercept measurement tool of ImageJ software, series of dark field images associated with different spots in the recorded diffraction pattern images were analyzed. It has been acknowledged that the recorded images were two dimensional projections of the grains. It is imperative to note here that to get an estimation of the grain size distributions with high precision, relatively new orientation microscopy techniques such as ASTAR^{TM}-precession electron diffraction [109] need to be used. In the current work, geometry of the grain was measured for its size (diameter) by drawing linear intersections (diameters) across each grain in at least eight different directions using the linear measurement tool of ImageJ software and presented as a mean value. The procedure was repeated for at least 25 grains within the field of view of each TEM micrographs and presented as a mean value with a standard deviation as the grain size. Such an assessment of TEM micrographs have been reported to estimate the grain size with a reasonable accuracy [110–112].

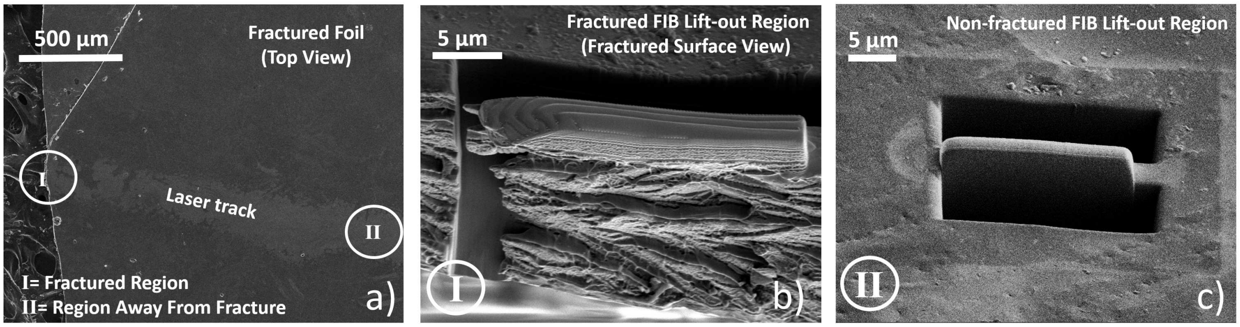

FIGURE 3.6. Set of micrographs showing (a) the regions for FIB lift out for a tensile fractured laser treated Fe-Si-B metallic glass, high magnification view showing (b) FIB lift-out region at the fractured region within the laser track, and (c) FIB lift-out region away from the fracture.

CHAPTER 4

RESULTS AND DISCUSSION

4.1. Effects of Laser Thermal Treatment on Crystallization of Fe-Si-B Metallic Glass [1]

The current Section explores the evolution of crystallization in light of various thermokinetic effects induced during laser thermal treatments of Fe-Si-B metallic glass. The observations of crystallite size as a function of laser processing condition (Table 3.1) have been presented. Identification of the crystalline phases formed has been performed with the aid of various techniques. The microstructure evolution has been analyzed based on computational predictions of the time temperature cycles induced within the material during laser thermal treatments.

4.1.1. Observations of Crystallite and Phase Evolution

XRD analysis was utilized for initial assessment of crystallization. XRD spectrum of as-cast Fe-Si-B metallic glass foil contained a broad hump typical to the amorphous nature of material (Fig. 4.1). XRD spectrum for 400 mm/s (0.53 J/mm^2 fluence) also wielded a pattern similar to as-cast material thereby indicating the absence of any crystallization and retention of amorphous nature during laser thermal treatment with such rapid scanning speed (Fig. 4.1). However, with increase in laser fluence, within the range of fluences (0.60-0.90 J/mm^2) employed in the present work, XRD spectra indicated the occurrence of crystallization with the presence of α-(Fe,Si) peak (Fig. 4.1). Specifically, the peak became more prominent in terms of its intensity and sharpness with increase in laser fluence (decrease in scanning speed). The corresponding crystallite size, X, was determined using the Scherrer's formula (Eq. 4.1) [113] and presented as function of laser fluence (F), beam residence time (t$_o$) and average peak temperature (T) attained during processing in Fig. 4.2.

$$X = \frac{0.9\lambda}{\beta cos(\theta_B)} \tag{4.1}$$

---

[1] The content of this section has been previously published in author's publication: Joshi, Sameehan S., et al. "Dynamic crystallization during non-isothermal laser treatment of Fe–Si–B metallic glass." Journal of Physics D: Applied Physics 48.49 (2015): 495501. (Reproduced with permission from IOP Publishing Ltd.)

where λ is the X-ray wavelength, β is the value of X-ray peak full width at half maximum (FWHM) in radian, and θ_B is the Bragg angle in degree of the peak in consideration. The analyses was performed using peak analyses and measurement tools of the OriginPro^{tm} plotting software. It is acknowledged here that the peak broadening can result from factors such as instrument induced factors and stresses apart from average crystallite/grain size within the sample [114]. However, the experimental conditions were consistently maintained and all the starting material was from the exact same sheet of the metallic glass. In light of this, it was reasonable to assume that the other factors were normalized and the variation in crystallite/grain size was the main contributor towards variation in corresponding peak broadening in XRD spectra. Moreover, it has been reported that crystallite size estimations using Eq. 4.1 are reasonably accurate for Fe based and other nanocrystalline systems [69, 91, 114–118].

Primarily, the crystallite size increased with increase in laser fluence initially and then appeared to reach nearly stable value of about 32 nm. In other words, the crystallite size increased rapidly with a decrease in laser scanning speed initially and then reached an almost steady value of 32 nm with a further decrease in scanning speed within the range of scanning speeds explored in the present study.

The DSC curves revealed two crystallization events (Fig. 4.3) which are typically observed for this material [1, 119]. The first crystallization event began at 780 K and second followed at 820 K. The first crystallization peak corresponded to α-(Fe,Si) phase, whereas the second peak was associated with the formation of Fe_3B followed by its transformation to Fe_2B intermetallic phase as reported in the literature [119] for this type of metallic glasses. Even though Fe_2B peaks were not distinctly observed in XRD spectra of laser processed metallic glass foils (Fig. 4.1), the DSC analysis indicated formation of Fe_2B phase [1, 27, 119]. This can be attributed to the closeness of the peaks of α-(Fe,Si) and Fe_2B and to the low fraction of Fe_2B formed which was possibly beyond the resolution of XRD analysis.

Estimation of transformed fraction (f) was done using comparison of areas under the peaks in DSC curves (Fig. 4.3) corresponding to crystallization events. These areas

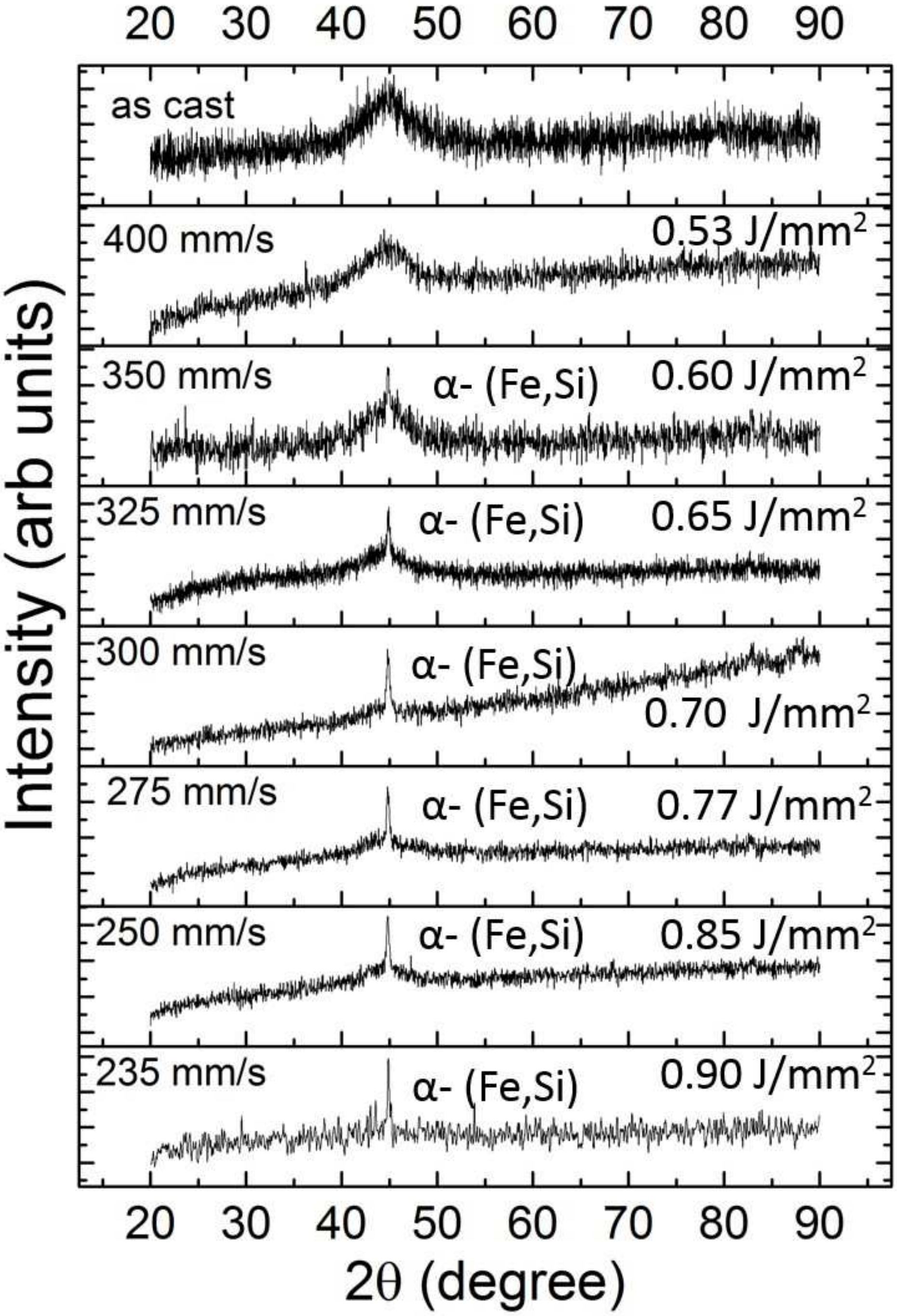

Figure 4.1. XRD patterns of Fe-Si-B metallic glass foil samples subjected to various laser energy inputs indicating crystallization.

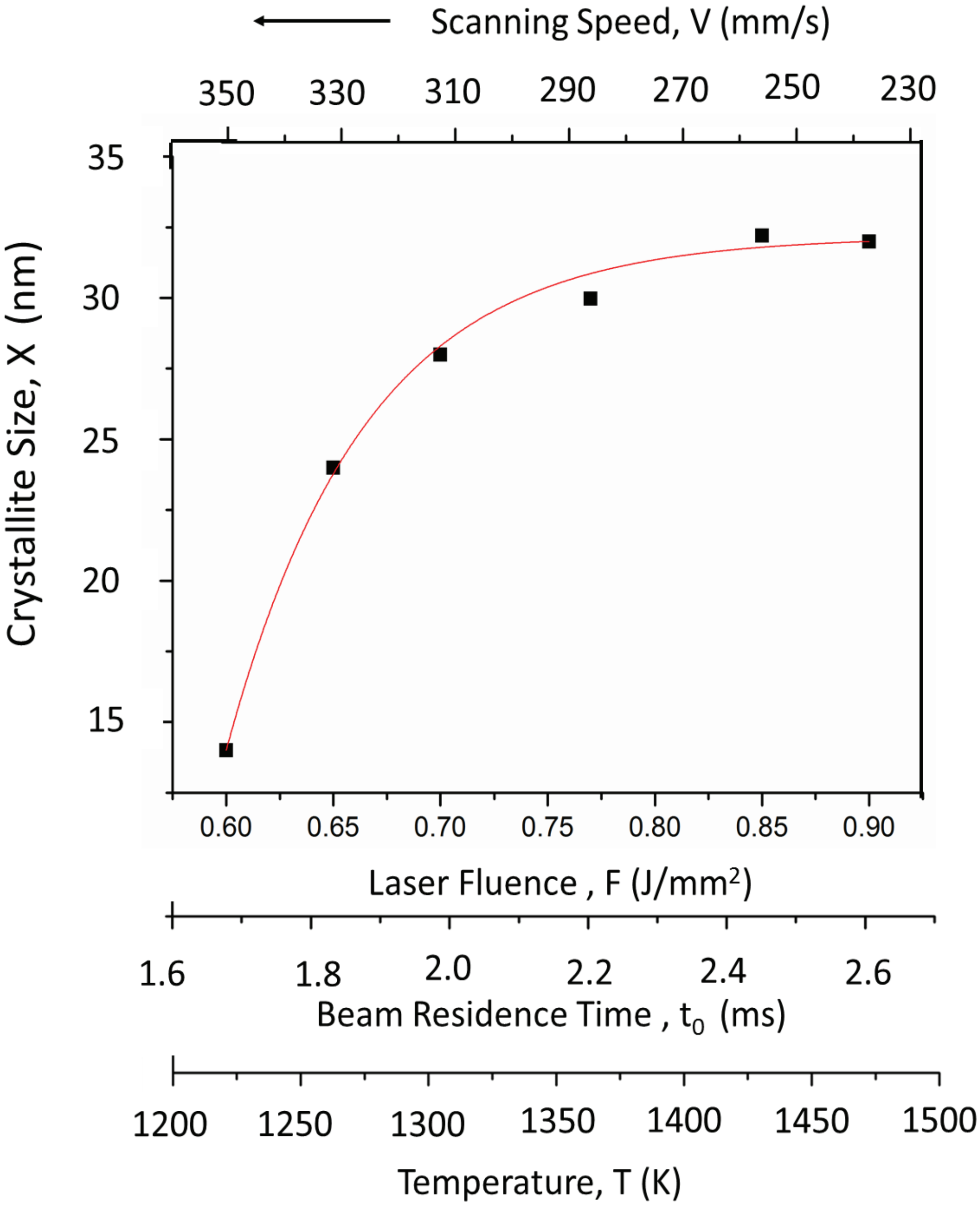

Figure 4.2. Variation of crystallite size with laser fluence, beam residence time, peak temperatures reached and scanning speed.

represent heat of crystallization for as-cast (ΔH_{cast}) and laser processed (ΔH_{laser}) samples. Crystallization being an exothermic process, if there are pre-existing crystals in the volume of material being tested, less heat would be evolved as compared to completely amorphous sample. There was a clear reduction in area under the crystallization peaks for laser processed

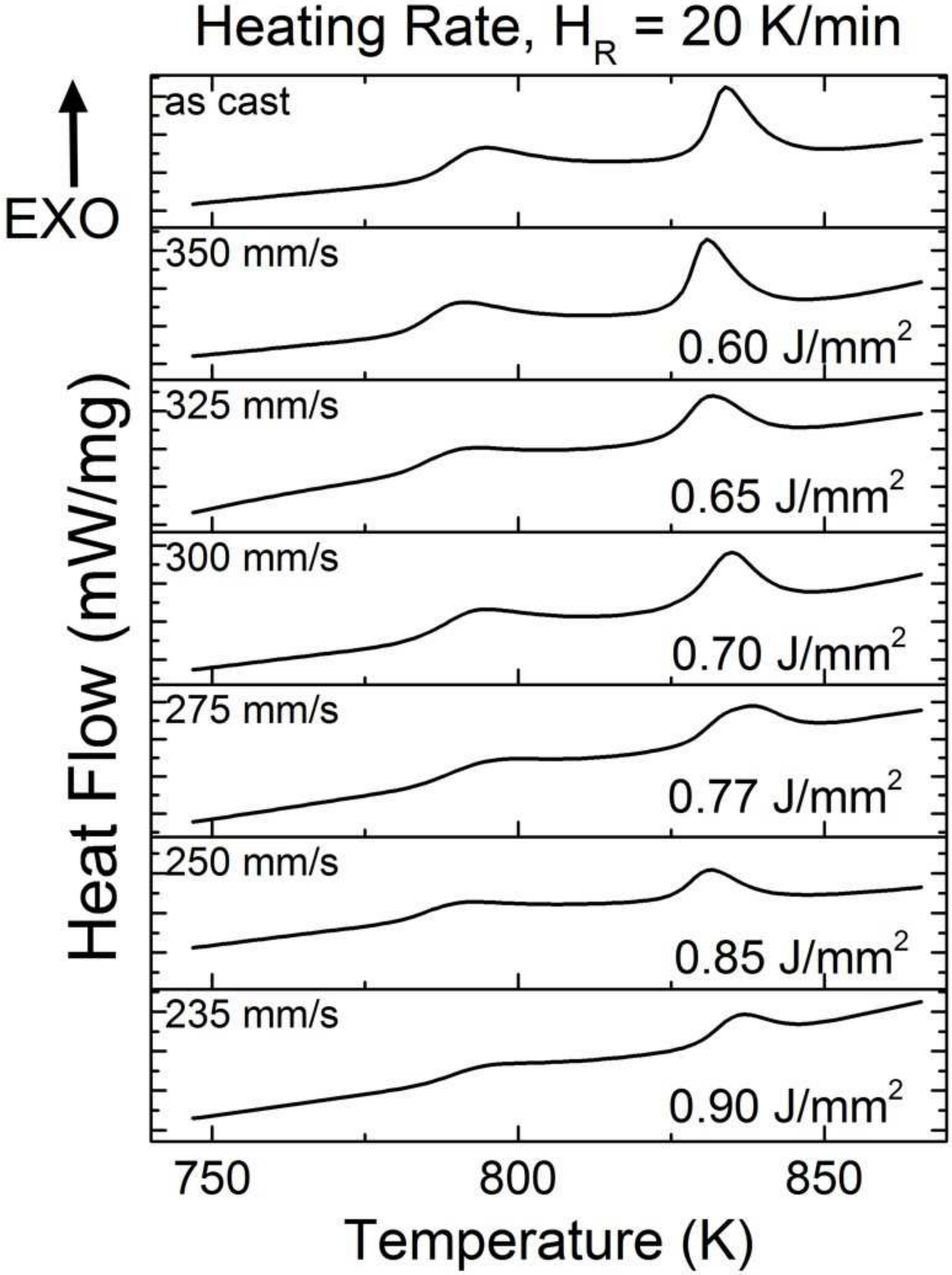

FIGURE 4.3. DSC curves for Fe-Si-B metallic glass foils treated with various laser fluences. They indicate two crystallization events and reduction in area under the curve for those with progressive crystallization.

samples as compared to as-cast sample, indicating crystallization happened during laser thermal treatment. Eq. 4.2 was employed for the estimation of f as

$$f = m.(f_{\alpha(Fe,Si)}) + n.(f_{Fe_2B}) \tag{4.2}$$

where $f_{\alpha(Fe,Si)}$ and f_{Fe_2B} are the fractions of α - (Fe,Si) and Fe_2B formed respectively and defined as f = $(\Delta H_{cast}$-$\Delta H_{laser})/\Delta H_{cast}$ [120, 121], m and n are defined here as multiplication phase factors. These quantities correspond to fraction of α-(Fe,Si) (phase factor m) and Fe_2B (phase factor n) formed when an as-cast amorphous Fe-Si-B alloy is completely crystallized. The values of m and n can be approximately calculated from equilibrium Fe-B phase diagram [122] using lever rule at the boron composition in the present system. With this approach of slight modification of the formula given in literature [120, 121], it is possible to approximately predict the fraction of each phase crystallized as well as the total crystallization by the following Eq. 4.3

$$f = m.\left(\frac{\Delta H_{cast} - \Delta H_{laser}}{\Delta H_{cast}}\right)_{\alpha(Fe,Si)} + n.\left(\frac{\Delta H_{cast} - \Delta H_{laser}}{\Delta H_{cast}}\right)_{Fe_2B} \tag{4.3}$$

Value of m and n are taken here as 0.82 and 0.18 corresponding to fractions of α Fe and Fe_2B in Fe-5at %B alloy. The fractions computed using Eq. 4.3 are presented in table 4.1. The fraction of crystalline phases steadily increased with laser fluence. α-(Fe,Si) got crystallized in significant amounts and fraction of Fe_2B indeed was very low.

Table 4.1. Fraction of Crystallization from DSC Analysis

Laser Fluence (F) J/mm^2	**Scanning Speed (V)** mm/s	**α-(Fe,Si) Crystallized Fraction** Vol%	**Fe_2B Crystallized Fraction** Vol%	**Total Crystallized Fraction** Vol%
0.60	350	16	0.5	16.5
0.65	325	29	5.0	34.0
0.70	300	31	6.0	37.0
0.77	275	32	6.2	38.2
0.85	250	37	7.0	39.0
0.90	235	46	7.4	53.4

Further, the formation of α-(Fe,Si) and Fe_2B as well as the nano size nature of

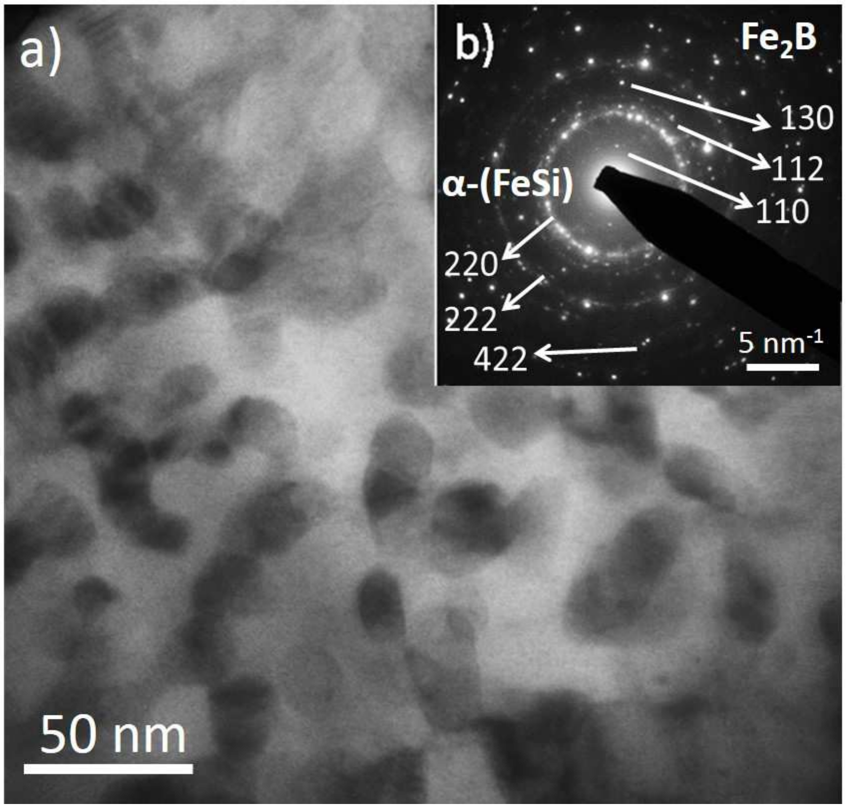

FIGURE 4.4. TEM micrograph of laser processed Fe-Si-B metallic glass foil showing (a) bright field image revealing nano grains and (b) the corresponding diffraction pattern indicating evolution of α-(Fe,Si) and Fe_2B.

crystallites were confirmed in TEM analysis for laser thermal treated Fe-Si-B metallic glass foil with scanning speed of 300 mm/s (0.7 J/mm^2 fluence). The representative TEM micrograph is presented in Fig. 4.4 along with selected area diffraction (SAD) pattern in the inset. The selected area diffraction (SAD) pattern (inset of Fig. 4.4) did confirm the presence of α-(Fe-Si) and Fe_2B phases as observed in DSC analysis (Fig. 4.3 and Table 4.1). Furthermore, the average crystallite size measured from multiple TEM micrographs was 29 ± 6 nm. It was very close to the average crystallite size of 28 nm determined from XRD analysis for this particular laser processing condition. Similar to the range of crystallite sizes obtained in the current work, it has also been reported for Fe-based nano crystalline materials that the crystallite sizes predicted by Scherrer's equation are reasonably accurate [7, 69].

Previously, similar behavior of crystallite coarsening has been observed in conventional isothermal annealing [7, 91, 123]. However, unlike the conventional isothermal techniques, the laser processing is a dynamic technique wherein temperature varies over extremely short time duration. To realize such dynamic development of thermal fields within the material, a FE based thermal model was developed. Following subsection has been dedicated to the discussions on estimations of the thermal model of laser thermal treatments followed by analyses of crystallization process based on these predictions.

4.1.2. Computational Predictions of Thermal Effects

The FE model was primarily used to estimate temperature evolution as a function of time during various laser treatments. As mentioned in Chapter 3, the laser power was fixed while the scanning speeds were varied to get various laser fluences on the sample surface. Therefore, the material experienced variation in laser energy density as well as beam residence times. In view of this, the heating and cooling curves derived from the computational thermal model are presented in Fig. 4.5.

The estimated peak temperatures increased as a function of laser fluence as expected. Moreover, the heating and cooling rates are significantly rapid (10^4-10^5 K/s) compared to that in the conventional processing techniques (10-10^2 K/s). Therefore, the conventional theory of crystallite growth under equilibrium thermal conditions is likely to deviate when applied in the analyses of phenomenon of crystallization and growth during laser processing which often experiences near or complete non-equilibrium thermal conditions. In view of this, the unique characteristics of laser processing were taken into consideration. The crystallization process was analyzed based on the predictions of the thermal FE model with the aid of additional extracted parameters such a heating rates, cooling rates, and peak temperatures. The following subsection presents discussions about dynamic process of crystallization of Fe-Si-B metallic glass during laser thermal treatments.

4.1.3. Influence of Thermokinetic Effects during Laser Treatments on Crystallization

It is a well known observation that crystallization temperature shifts to higher level during dynamic (non-isothermal) treatment [4, 45, 124, 125]. This effect could be

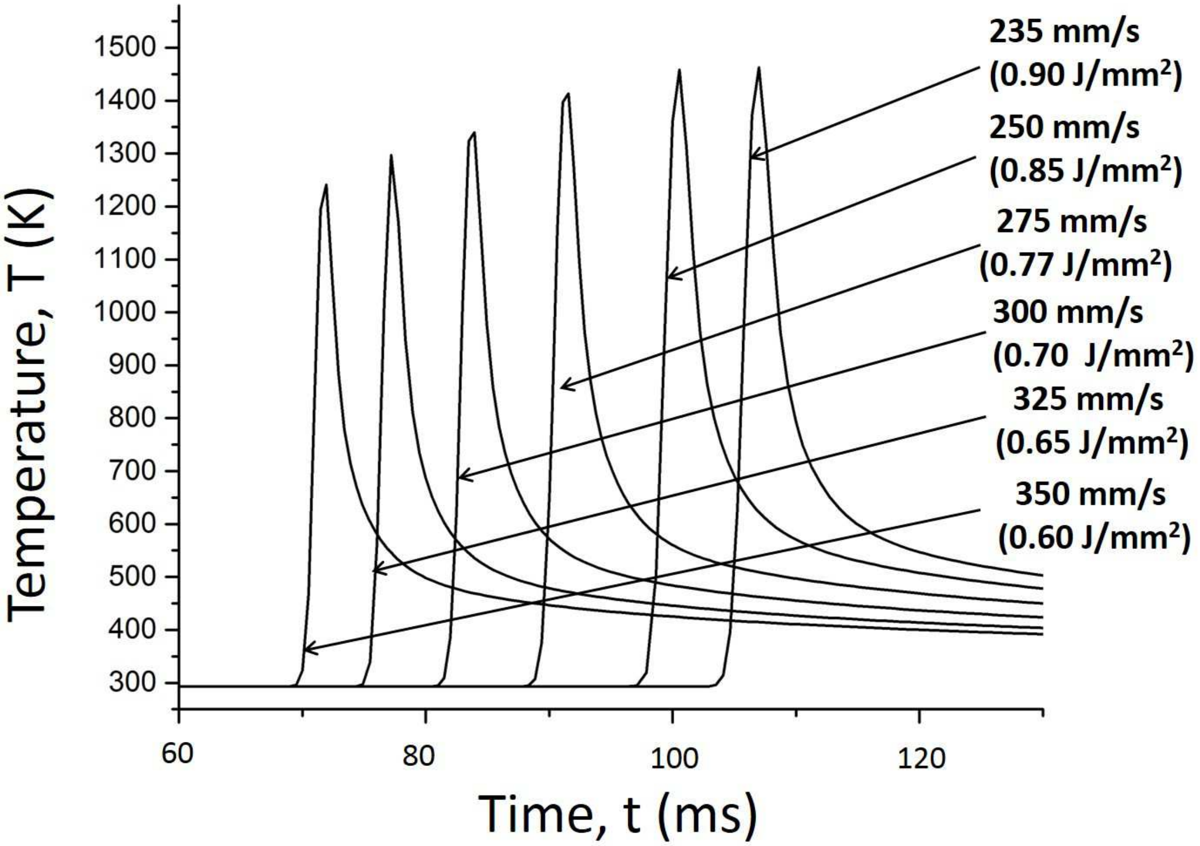

FIGURE 4.5. Temperature as a function of time for various laser processing conditions as predicted by the thermal model.

mathematically expressed by the Ozawa equation (Eq. 4.4) [124]

$$ln(H_R) = \frac{-E_{cryst}}{RT_{cryst}} + B \tag{4.4}$$

where H_R is the heating rate, E_{cryst} and T_{cryst} are the activation energy (295 kJ/mol [91]) and the onset temperature of crystallization respectively, and B is the constant of integration. It has to be mentioned here that such analysis can also be done using Kissinger method [126]. As revealed from DSC analysis, for heating rate of 20 K/min, the onset of crystallization for present composition occurs at 780 K (Fig. 4.3). Therefore, the value of the constant B can be determined from Eq. 4.4 with the known parameters for a given material system.

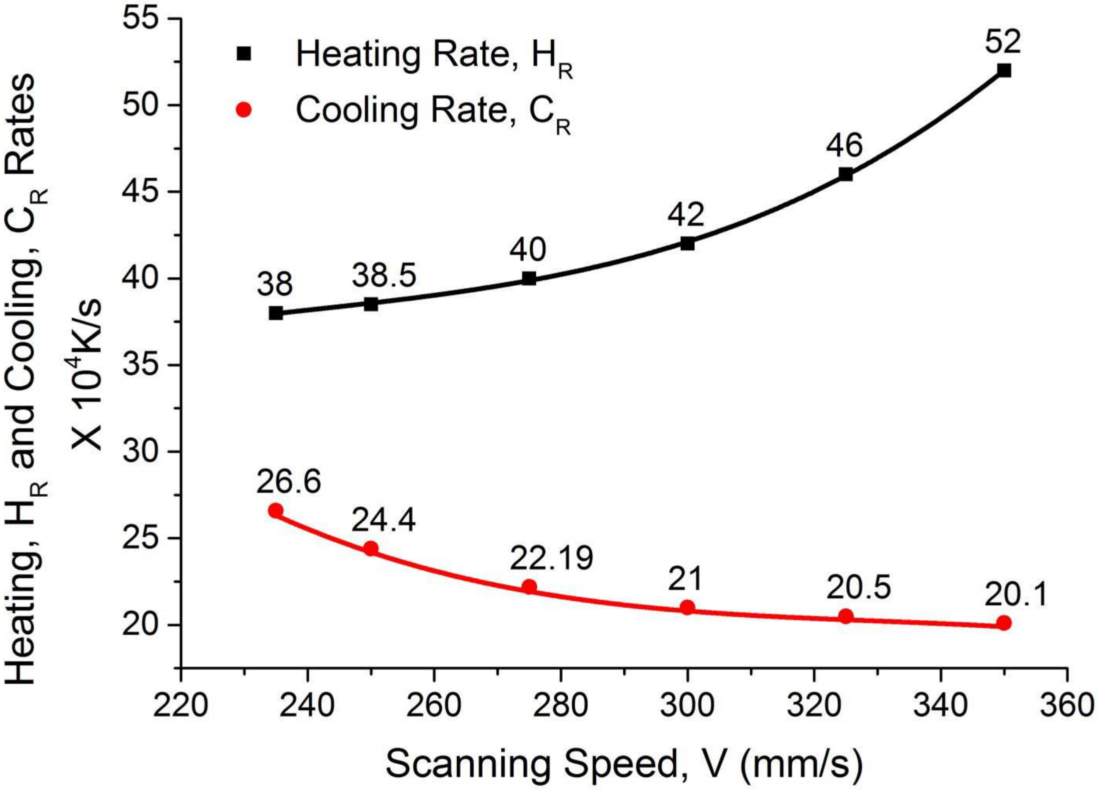

FIGURE 4.6. Heating and cooling rates predicted by thermal model during various laser scanning speeds.

The heating and cooling rates (K/s) were determined by curve fitting within the heating and cooling sections respectively of the data presented in Fig. 4.5 for the range of laser fluences (laser beam scanning speeds) employed in the present work. The heating rates increased whereas cooling rates decreased with increment in scanning speeds (decrease in laser fluence) (Fig. 4.6). The crystallization onset temperature T_{laser}, predicted for the range of laser fluences (laser beam scanning speeds) employed in the present work from Eq. 4.4 was much higher than 780 K (for 20 K/min heating rate), and gradually increased from 1089 to 1100 K with increase in scanning speed (Fig. 4.7 a). This is indicative of substantial delay in onset of crystallization followed by growth of crystallites during laser thermal treatment.

In case of any isothermal or non-isothermal (dynamic) treatment of amorphous material, crystallization commences at the crystallization onset temperature followed by the

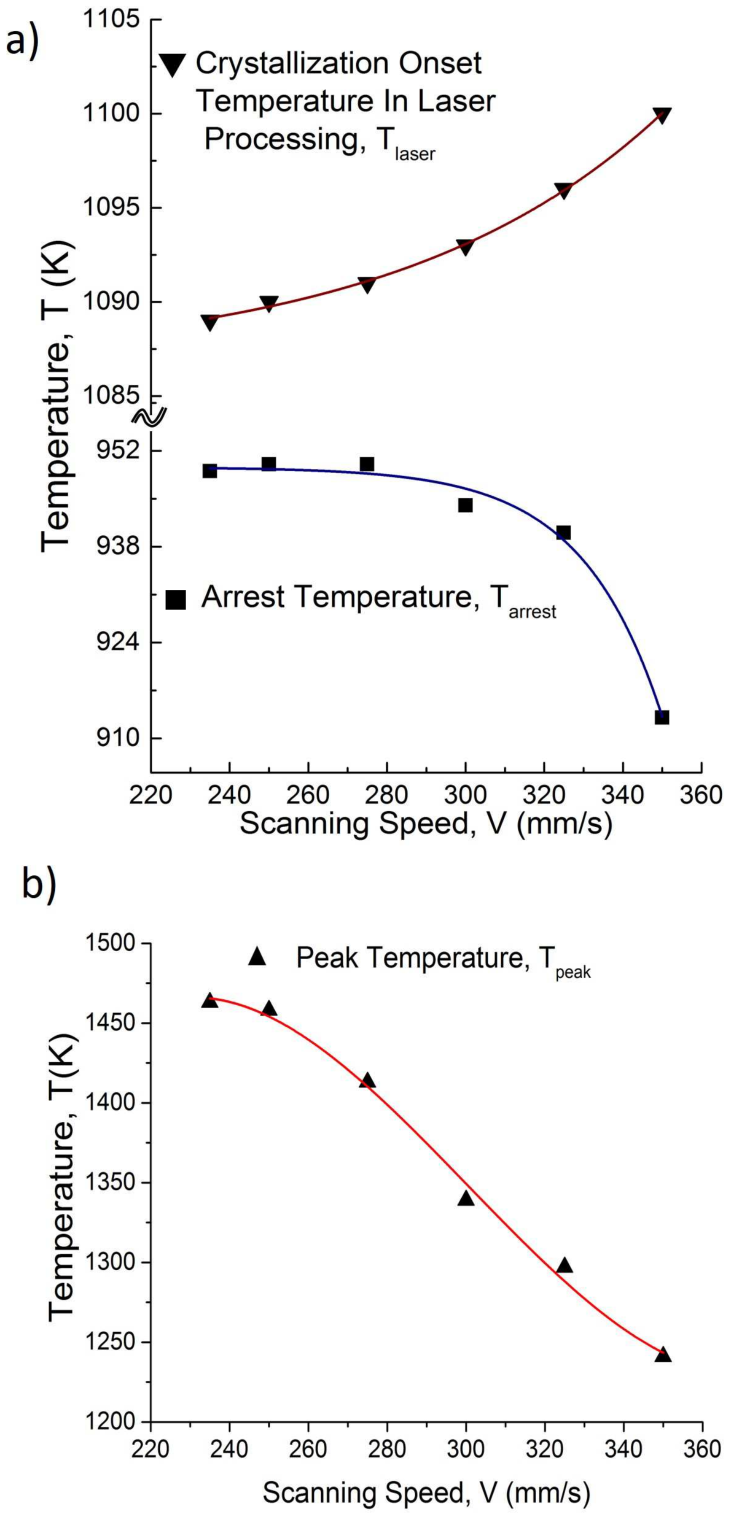

FIGURE 4.7. Variation in (a) onset of crystallization temperature in laser treatment T$_{laser}$, arrest temperature T$_{arrest}$, and (b) peak temperature T$_{peak}$ with laser beam scanning speed.

growth of crystallites through the heating and continues through the cooling process. The growth ceases when the temperature drops back to the crystallization onset temperature. During any non-isothermal treatment such as laser thermal treatment, temperature rises to the peak temperature while heating and drops rapidly during cooling after the termination of laser thermal treatment. However, the growth of crystallites continues during cooling cycle, until it is prematurely arrested (terminated) at the temperature T_{arrest} because of the rapid cooling. As explained earlier, estimation of crystallization onset temperature based on Ozawa equation (Eq. 4.4) took into account the heating rate during non-isothermal treatment. However, termination of crystal growth at temperature, T_{arrest} occurred in the cooling stage of the non-isothermal treatment. In view of the preexisting crystals, a semi-empirical approach involving cooling rate, C_R was adopted to estimate T_{arrest}. Accordingly, Eq. 2.2 was modified to include time t, as a function, f(T,C_R) of temperature, T and cooling rate C_R and expressed in the Eq. 4.5.

$$X^{1/n} = k_0.\ e^{(\frac{-E}{RT})}.\ f(T, C_R) \tag{4.5}$$

The function, f(T,C_R), was obtained as an expression corresponding to a curve fit in the cooling section of the data presented in Fig. 4.5. The activation energy E and k_0 for α-(Fe,Si) crystallite coarsening are reported as 248 kJ/mol and 0.00424 respectively [69]. The value of n was approximately chosen as 0.5, which describes parabolic growth of crystallites, and holds good in initial stages of crystallite growth till the crystallite size reaches values of the order of 60 nm [7]. Using the experimental values of crystallite size for X (Fig. 4.2), and f(T,C_R) from the cooling cycles in Fig. 4.5, corresponding temperatures were computed using Eq. 4.5. Thus, the temperature computed semi-empirically, from Eq. 4.5, is the temperature T_{arrest} at which the crystallite growth was arrested. Although T_{arrest} (913-949 K) for all laser fluences is higher than 780 K, the temperature of crystallization onset for 20 K/min heating rate, it decreased with increase in scanning speed (with decrease in laser fluence) within the range of laser processing parameters explored in the present work (Fig. 4.7 a). The laser thermal treatment being a dynamic (non-isothermal) process, the variation from

T_{laser} to T_{arrest} happens via attendance of maximum temperature, T_{peak} corresponding to termination of laser treatment in the intermediate stages. This T_{peak} computed using thermal model described earlier and presented in Fig. 4.5 decreased with increase in scanning speed (with decrease in laser fluence) within the range of laser processing parameters explored in the present work (Fig. 4.7 b).

The crystallite size indicated by XRD and TEM analyses was the net result of heating and cooling cycles. As schematically illustrated in Fig. 4.8, the time duration, Δt, between the onset of crystallization during laser treatment (T_{laser}), and the temperature at which growth ceased (T_{arrest}), was the time over which the entire crystal growth took place. Since, the peak temperatures, T_{peak} distinctly changed for each processing condition (Fig. 4.7 b), the difference, ΔT in T_{peak} and T_{arrest} (Fig. 4.8), can also be a distinct indicator of the influence of dynamic nature (variation of temperature in short duration of time) and various process parameters on crystal growth during non-isothermal processing such as laser thermal treatment adopted in the present work. In view of this, it is worth noting that both ΔT and Δt decreased with increased scanning speed, in other words decreased laser fluence (Fig. 4.9). This in turn also resulted in providing decreased crystallite size with increased scanning speed or decreased laser fluence (Fig. 4.2). It was clear that increased heating rates (figure 4.6) and decreased ΔT and Δt with increased scanning speed, ie., lowered fluences (Fig. 4.9) resulted in providing reduced thermal gradient and time for the crystal growth. As a result, the non isothermal laser thermal treatment yielded much smaller crystallites (size less than 35 nm) (Fig. 4.2) as compared to several other conventional and non-conventional thermal treatments (50-150 nm) [28, 29, 91]. These observations indicated that in general, dynamic non-isothermal laser treatment generated extremely rapid heating and cooling rates that shifted the temperatures of crystallization onset and termination of crystallite growth to higher temperatures thereby substantially reducing the time interval of crystallite growth.

Thus the crystallization was strongly influenced by the laser process parameters. Although the peak temperatures developed during laser treatments were high (1241-1463 K),

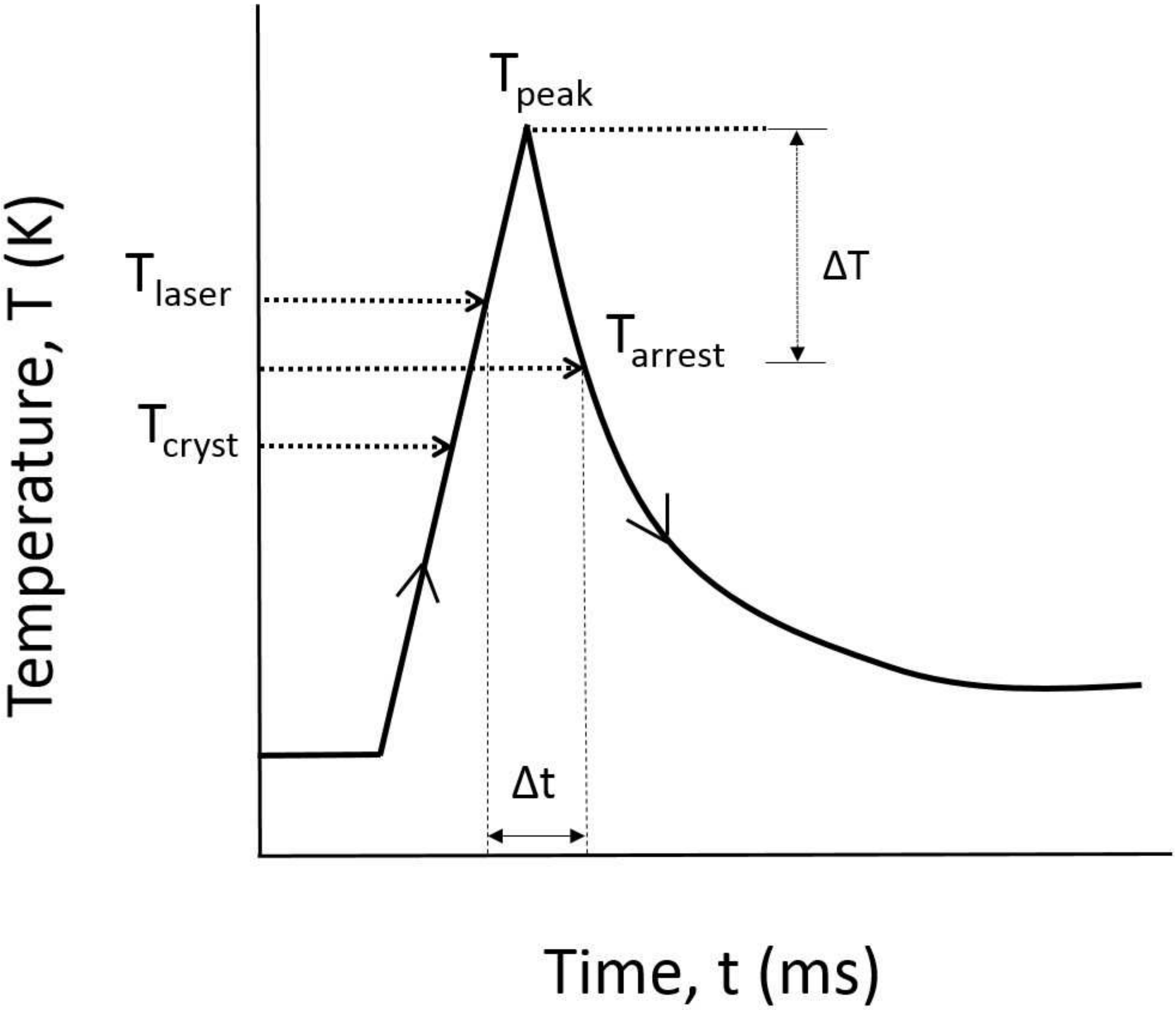

FIGURE 4.8. Schematic of time-temperature curve illustrating concept of arrest temperature, time of growth Δt, and dynamic nature of laser processing.

the coarsening of crystallites was avoided due to rapid heating and cooling rates (10^4-10^5K/s) inherently associated with the laser thermal treatment. It has been reported that Fe-Si-B alloys can coarsen above 100 nm, and additions of Nb and Cu are required to limit the coarsening [127]. Furthermore, in the non-conventional technique such as microwave heating of $Fe_{73}Si_{16}B_7Nb_3Cu_1$, with the heating rates of the order of 10^2 K/s, heating of the entire volume of the material resulted in generation of average crystallite size of 64 nm [29]. On the contrary, in the present case, without any alloying addition, direct laser thermal treatment of Fe-Si-B amorphous alloy generated much finer crystallite size with the occurrence of

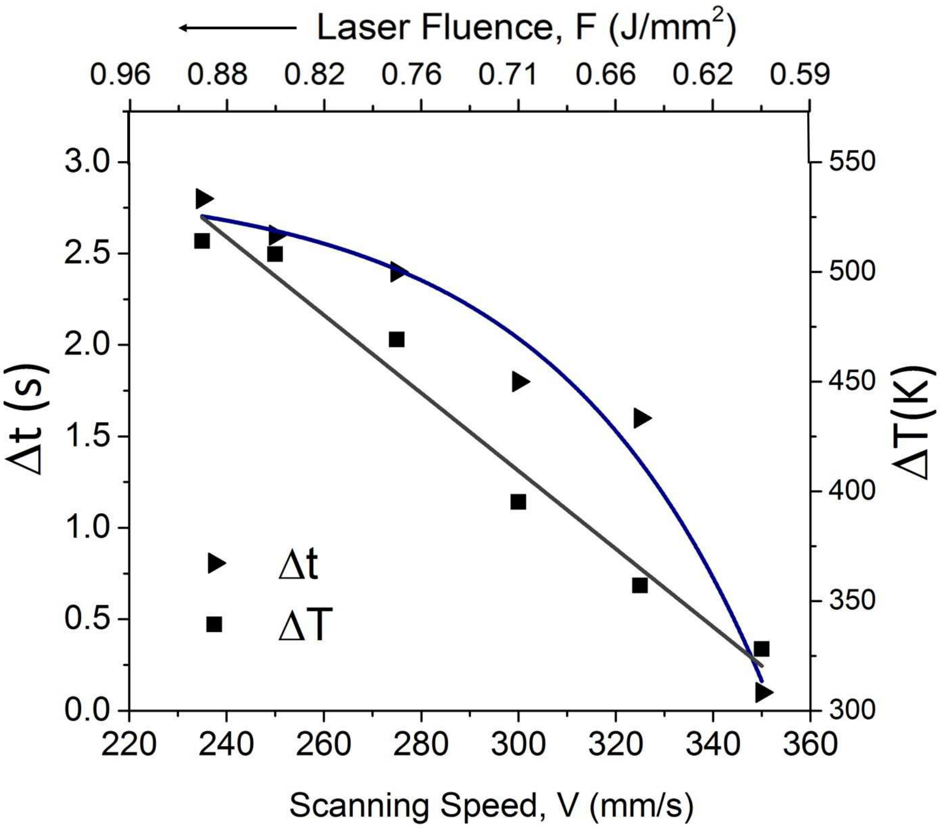

FIGURE 4.9. Dynamic nature of process reflected in variation of time of growth (Δt) and difference between peak and arrest temperatures (ΔT) with scanning speed.

crystallization only in laser treated region. This laser-based thermal treatment approach wields an added advantage of producing composite materials with nano crystals embedded in amorphous matrix via selective crystallization which are reported to have much superior magnetic performance [1, 71] and mechanical properties [128]. Thus, the current efforts in succession of the previous work published on same material and similar laser treatment by the present research group [1, 30, 43, 71], provided more understanding regarding the dynamic effects of laser processing parameters on important crystallization attributes such as temperature of crystallization onset and crystal growth arrest along with the total time of crystallization. The overall understanding of the effect of these parameters is likely to provide precise control in tailoring the process for desired microstructure in amorphous material. After developing understanding about the crystallization of laser treated Fe-Si-B metallic glass, as discussed in Chapter 1, th next goal was to understand effects of microsturucture evolution on tensile behavior of laser treated metallic glass. The results about the same have been presented in the following Section.

4.2. Tensile Behavior and Process Optimization of Laser treated Fe-Si-B Metallic Glass [2]

In this Section, the main focus is on effects of laser processing parameters (Table 3.2) on tensile behavior of Fe-Si-B metallic glass. Moreover, for any processing operation, the optimization of processing conditions/parameters to arrive at the desired outcome becomes critical. In view of this, efforts made on statistical optimization of laser processing parameters using response surface methodology of statistics have been discussed. Such efforts are helpful in expedited realization of the structure-property relationship. Based on these optimizations and confirmations, further detailed investigations of microstructure and phase evolution have been presented. Thus, the current Section tries to bridge the process optimization with physics-based investigations of the effects of processing within the material.

4.2.1. Observations of Stress Strain Behavior

The engineering stress-strain curves for the as-cast as well as the laser treated foils indicated purely elastic behavior (Fig. 4.10). The point of UTS/fracture strength was same as the fracture strength due to the elastic nature of the stress-strain curve. The UTS/fracture strength values for the as-cast and the foils treated with the laser fluences of 0.39-0.52 J/mm^2 were within the range of 1500-2500 MPa. For the laser fluences in the range 0.53-0.71 J/mm^2, the UTS/fracture strength values severely dropped and were in the range of ∼300-500 MPa. These observations suggested some drastic structural changes happening within laser thermal treated Fe-Si-B metallic glass with an increase in laser fluence. To obtain a quick qualitative idea about such structural changes, electrical resistivity measurements on these samples were performed.

---

[2] The content of this section has been previously published in author's publications:
(i) Joshi, Sameehan S., et al. "Tensile behavior of laser treated Fe-Si-B metallic glass." Journal of Applied Physics 118.16 (2015): 164904. (Reproduced with permissions from AIP Publishing LLC) and
(ii) Joshi, Sameehan S., et al. "Optimization of laser thermal treatment of Fe–Si–B metallic glass." Journal of Manufacturing Processes 24 (2016): 31-37. (Reproduced with permission on behalf of The Society of Manufacturing Engineers from Elsevier Ltd).

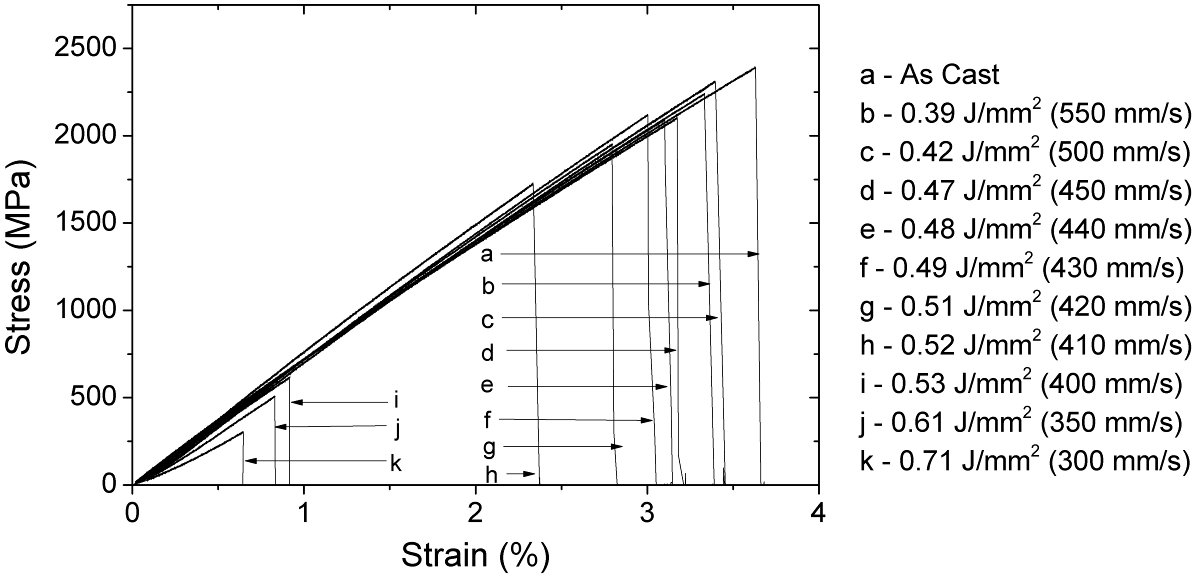

FIGURE 4.10. Representative engineering stress-strain curves are depicted for Fe-Si-B metallic glass foils treated with single laser track at the center of gage length.

4.2.2. Localized Structural Changes during Laser Thermal Treatments

In order to realize the structure-property relationship in an expedited manner, electrical resistivity measurements were performed on as-cast and laser treated metallic glass foils. Electrical resistivity is a good and quick tool (compared to other sophisticated methods such as X-ray and electron diffraction) to track the crystallization process which critically influences the physical and functional properties of laser treated Fe-Si-B metallic glass.

Heating amorphous materials to energy levels insufficient for crystallization may result in structural relaxation [12, 129, 130]. During relaxation, atoms of amorphous materials undergo rearrangements to lower overall free energy [131, 132]. This process continues till the amorphous structure reaches the lowest possible free energy before commencement of crystallization. Noticeably, structural relaxation can result in the variation of various properties such as resistivity, density, and free volume of amorphous materials [130]. In the current work, the manifestation of relaxation was realized by expressing resistivity as a function of laser fluence (Fig. 4.11). Compared to the resistivity of the as-cast foil, the resistivity of the laser treated foils increased initially with increase in the laser fluence (0.39 and 0.42 J/mm^2). Further increase in the laser fluence to larger values (0.47-0.71 J/mm^2) gradually dropped the resistivity of the laser treated foils to the values smaller than the resistivity of the as-cast foil. The initial increase in resistivity is a clear indicator of structural relaxation as reported in the literature [55, 133, 134]. The reason behind such an increase has been attributed to redistribution of the free volume upon commencement of structural relaxation in a metallic glass. At the same time, the redistribution of free volumes also alters the localized arrangements of the atoms. Moreover, as the laser treatment induces rapid cooling ($\sim 10^4$ K/s, Fig. 4.7 a), it is possible that such a structure with redistributed free volume and atoms gets retained after completion of the laser treatment. Collectively, these localized structural changes and process induced rapid cooling led to increased scattering centers throughout the structurally relaxed volume of the material leading to an increase in the electrical resistivity [55].

Another phenomenon which could be occurring prior to crystallization is phase separation [135–138]. In such as case, a localized redistribution of atoms causes a fine scale compositional phase separation prior to commencement of crystallization. Such a localized inhomogeneity of clusters of different compositions could also lead to excess number of scattering centers compared to a as-cast metallic glass leading to an increase in the electrical resistivity. However, this aspect needs a further investigation to provide a direct observational evidence. Thus, an initial increase in resistivity could be due to redistribution of atoms, and free volume along with a localized phase separation prior to crystallization.

After the redistribution of atoms and free volume at lower laser fluences, the annihilation of free volume commenced at higher temperatures achieved for higher laser fluences. The reduction in free volume pushed the laser treated Fe-Si-B metallic glass towards crystallization. The crystallization reduces the number of scattering centers as reflected in a gradual drop in resistivity with further an increase in the laser energy can. Such a a gradual drop can be associated to progressively higher volume of crystallization [134]. Based on these resistivity measurements, a possible structural evolution consisting of structural relaxation and partial crystallization was expressed schematically (Fig. 4.12).

With these observations, it was evident that for laser fluences the Fe-Si-B metallic glass foils likely underwent structural relaxation. Whereas, for the higher laser fluences the metallic glass foils provided an indication of occurrence of crystallization. As discussed earlier in Chapter 3, the process of partial crystallization was necessary for functional properties as reported by previous investigations from the current research group [1, 27, 30, 43, 94], observations of Fig. 4.10 indicated that the process of crystallization would have been responsible for reduction in the strength values. Thus, there was a need to investigate a laser fluence which would induce crystallization in Fe-Si-B metallic glass foils needed for functional performance at the same time retain a high mechanical strength. Response surface methodology based statistical optimizations were performed for this purpose as discussed in the following subsection.

4.2.3. Statistical Process Optimization to realize Structure-Tensile Property Relationship

As stated earlier in Chapter 2, the optimized condition was set as the one which would show reduction in resistivity (a qualitative indicator of fraction of crystallization) while retaining high strength. In order to do this, the experimentally derived values were input to the RSM algorithm. In case of UTS/fracture strength, a logarithmic function (Eq.4.6) resulted in the best fit ($R^2 = 0.87$) whereas electrical resistivity showed the best fit ($R^2 = 0.92$) by inverse square root function (Eq.4.7). The actual versus predicted plot for UTS/fracture strength as well as electrical resistivity indicated a linear trend pointing towards a reasonable choice of corresponding fitting functions (Fig. 4.13 a and b). The plot of externally studentized residuals and predicted values by the fitting function indicated the absence of any trend in both the cases (Fig. 4.13 c and d). The significance of such a plot is that it indicates constant variance in the data, a requirement to perform ANOVA [139]. In addition, it has been reported that, an externally studentized residual greater than 3.5 points towards possible outliers, that is a value with the possibility of unacceptable error [140]. No such outliers were observed in either of the cases. These initial results during optimization indicated the suitability of experiments under consideration towards ANOVA

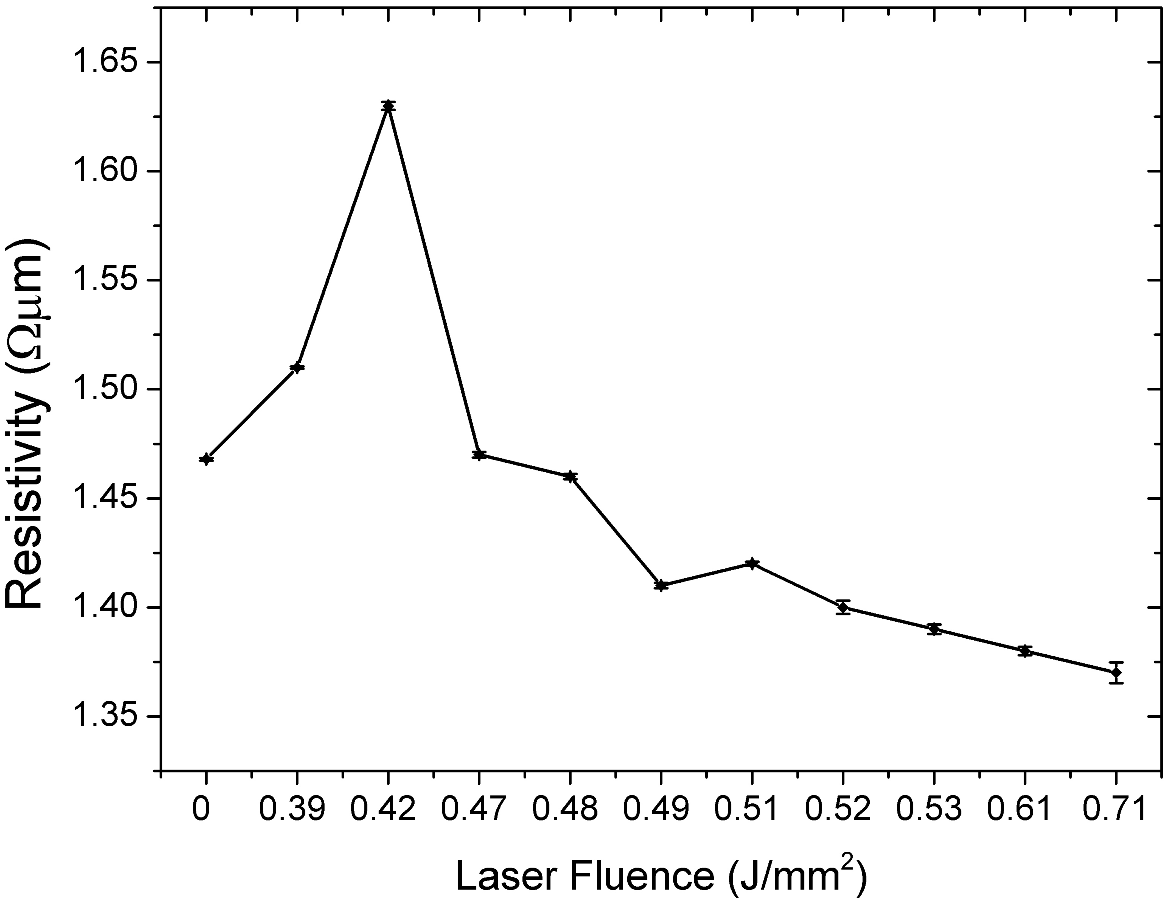

FIGURE 4.11. Variation in the resistivity of laser treated Fe-Si-B metallic glass foils as a function of laser fluence.

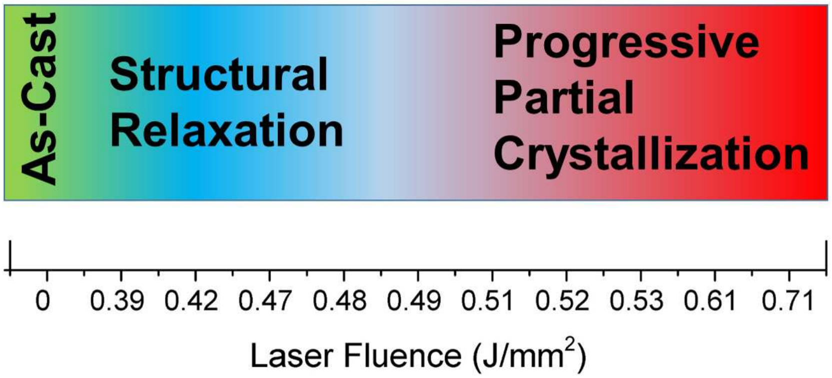

FIGURE 4.12. A possible structural evolution as a function of laser fluence for laser treated Fe-Si-B metallic glass.

and subsequent investigation about the most optimal condition.

$$Logit(U) = ln\frac{U-300}{2191-U} = -439 + 2603*F - 4930*F^2 + 2991*F^3 \tag{4.6}$$

$$\frac{1}{\sqrt{\rho}} = 126 - 1197*F + 4515*F^2 - 8423*F^3 + 7778*F^4 - 2845*F^5 \tag{4.7}$$

Where U stands for UTS/fracture strength and ρ denotes electrical resistivity.

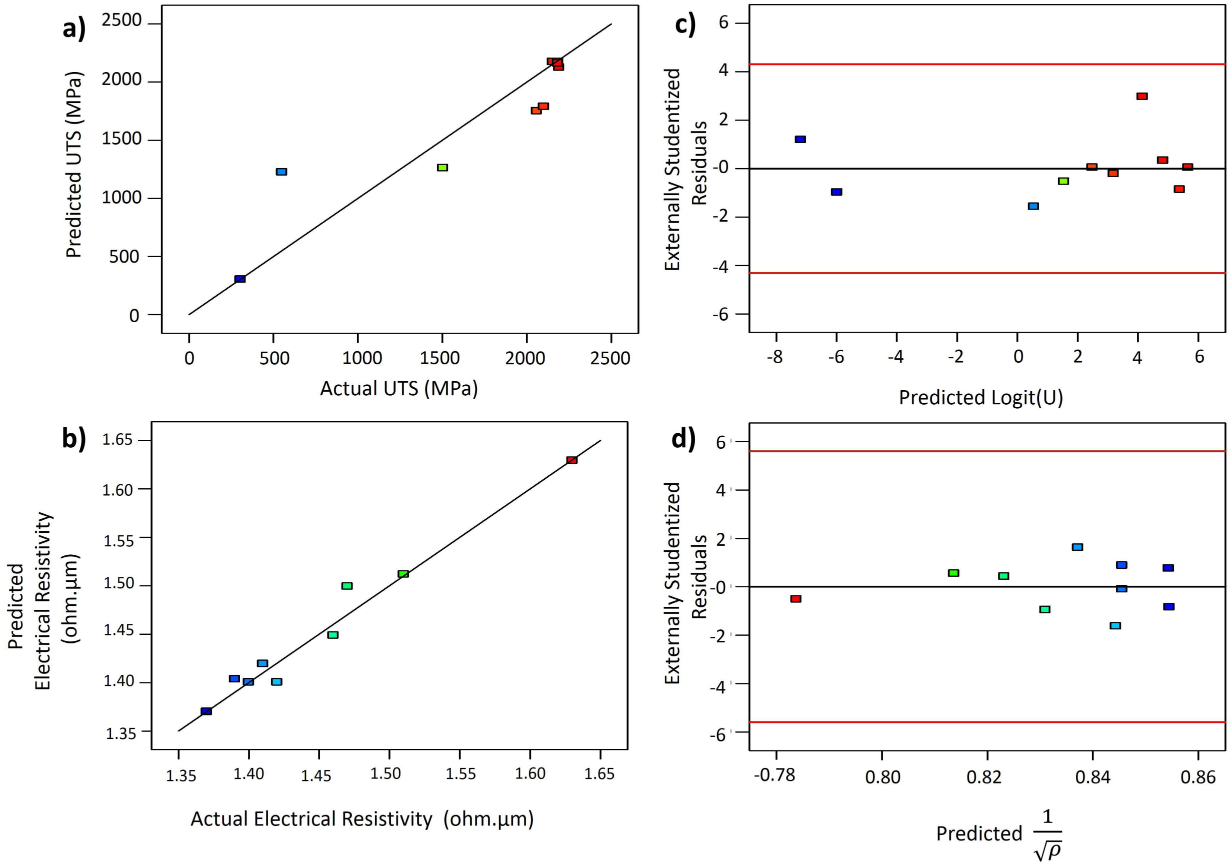

FIGURE 4.13. Set of plots showing predicted vs actual values for and (a) UTS/fracture strength and (b) electrical resistivity and externally studentized values versus predicted values by the function showing a random scatter for (c) UTS/fracture strength and (d) electrical resistivity.

Another important aspect of the optimization study is the behavior of desirability function. This function takes into account the desirable conditions for the individual responses of the experiment and assigns the desirability index for each response for corresponding processing condition. An overall/composite desirability is then computed by the optimization software to indicate the most favorable processing condition [140, 141]. The overall/composite desirability index of 1 is considered ideal and any value closer to it corresponds to the most suitable processing condition. Mathematically the overall/composite desirability is expressed as a geometric mean according to Eq. 4.8 [141, 142]

$$D = d_1^{w_1} * d_2^{w_2} * d_3^{w_3} .... * d_n^{w_n} = \left(\prod_{i=1}^{n} [d_i^{w_i}] \right)^{\frac{1}{\Sigma w_i}} \tag{4.8}$$

where D denotes a overall/composite desirability for a particular experimental condition, i is the number of responses being evaluated during the experiment, d is the individual desirability for each response, and w is the weighting assigned to the respective response.

Furthermore, the individual desirability in case of maximizing a response has been mathematically expressed according to Eq. 4.9 [143]

$$d = \begin{cases} 0, & \text{y<L} \\ \left(\frac{y-L}{T-L}\right)^w, & L \leq y \leq T \\ 1, & \text{y>T} \end{cases} \tag{4.9}$$

where y is the response, T is the target value for y, L is the lowest value obtained in the experiments for y.

On the contrary to the case given in Eq. 4.9, the individual desirability in case of minimizing a response takes the mathematical form as expressed in Eq. 4.10 [143]

$$d = \begin{cases} 1, & \text{y<T} \\ \left(\frac{H-y}{H-T}\right)^w, & T \leq y \leq H \\ 0, & \text{y>H} \end{cases} \tag{4.10}$$

where H is the highest value of y obtained in the experiments.

As mentioned before, the processing condition leading to low electrical resistivity (indicating reasonable fraction of crystallization) and high UTS/fracture strength was regarded desirable in present investigation. This implied assigning the equal weighting (w=1) for both of the responses. Based on these considerations, the overall/composite desirability index was computed by the StatEase^{TM} optimization software in accordance with Eq. 4.8, 4.9, and 4.10. Furthermore, it was expressed as a function of laser fluence (and scanning speed) (Fig. 4.14). There was a drop in overall/composite desirability as a function of laser fluence within the laser fluence range of 0.39-0.43 J/mm^2. Even though the UTS/fracture strength was very close to the as-cast metallic glass foil in this range, the electrical resistivity increased as a result of structural relaxation (Figs. 4.10 and 4.11). Hence, this was set as undesirable condition in the optimization process. With further increase in laser fluence (decrease in scanning speed), the overall/composite desirability also increased. Such an increase in desirability was the result of retention of high UTS/fracture strength and at the same time experiencing continuous drop in electrical resistivity by the laser thermal treated Fe-Si-B metallic glass foils. The desirability function reached a maximum at the laser fluence of 0.497 J/mm^2 (scanning speed of 425 mm/s) indicating towards most optimal processing condition and then dropped as a function of laser fluence (Fig. 4.14). At this point of maximum, the value of desirability was 0.91. The corresponding values of UTS/fracture strength and electrical resistivity were 2090 MPa and 1.4 $\Omega.\mu$m respectively (Fig. 4.14). Even though this exact value of laser fluence of 0.497 J/mm^2 was not actually employed in experimentation, it was much closer to the laser fluence of 0.49 J/mm^2 actually utilized in the current work. This particular condition had average UTS/fracture strength value of 2190 ±95 which is very similar to the values predicted from optimizations. Hence, this particular condition is likely to ensure generation of fraction of crystallization necessary for the low resistivity while retaining high UTS/fracture strength needed for the optimum performance. In light of this, in depth experimental investigations were carried out in terms of microstructure to do verification of the predictions by the RSM.

Hence, the statistical RSM based algorithms clearly pointed towards optimum laser fluences which would lead to crystallization at the same time retaining strength of laser

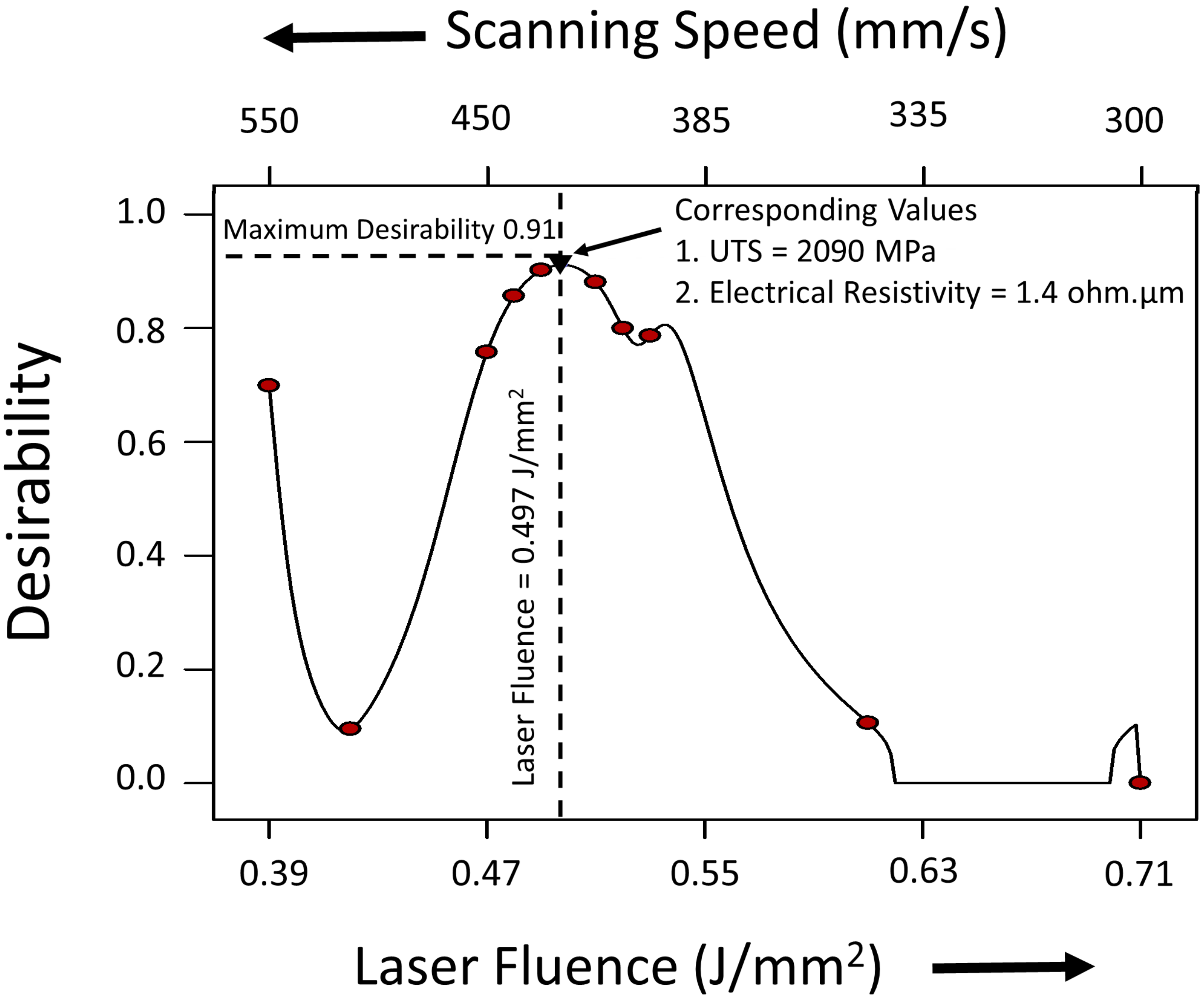

FIGURE 4.14. Behavior of desirability as a function of laser fluence.

treated Fe-Si-B metallic glass both required for its functional performance. To get further insights into microstructure developments in the laser treated zone of the Fe-Si-B metallic glass, an in depth investigation was undertaken as discussed in the following subsection. The results essentially served as confirmatory tests for the predictions of the RSM based optimizations.

4.2.4. Microstructure Evolution and its Effects on Tensile Behavior

The atomic rearrangements (amorphous to crystalline transition) of Fe-Si-B metallic glasses can be accomplished by subjecting them to laser thermal treatments. Apart from electrical resistivity discussed earlier (Fig. 4.11), as a primary means of investigating the occurrence of crystallization in the as-cast and laser treated foils, XRD experiments were performed. XRD spectrum of the as-cast foil (Fig. 4.15) revealed a typical hump characteristic of amorphous materials. Laser treated foils for the fluence range of 0.39-0.53 J/mm^2 (scanning speed range of 550-400 mm/s) exhibited similar hump in the spectra within the resolution limit of XRD technique (Fig. 4.15). The results primarily indicate that these scanning speeds were not sufficiently low (the laser fluences were not high enough) to crystallize the as-cast amorphous material (Fig. 4.15). However, increasing the laser fluence to the range of 0.61-0.71 J/mm^2 corresponding to the scanning speeds of 350 and 300 mm/s respectively, results in crystallization with the presence of α-(Fe,Si) peak in the corresponding XRD spectra (Fig. 4.15).

After collectively observing the results obtained from XRD analysis (Fig. 4.15), stress strain curves (Fig. 4.10), resistivity measurements (Fig. 4.11), and predictions of RSM (Fig. 4.14) the crystallization was expected for laser fluences around 0.49 J/mm^2 and higher. Therefore, further detailed analyses such as TEM and DSC were required to have idea of structural changes at happening at better resolution during laser thermal treatments using these set of laser fluences. Such findings have been presented in the following discussions.

Microstructure evolution during relaxation followed by crystallization has a marked influence on the tensile response of metallic glass foils [12]. The samples corresponding to the laser fluence range of 0.39-0.48 J/mm^2 appeared to retain the amorphous structure based on the SAD analysis. The representative TEM micrograph corresponding to the laser fluence of 0.42 J/mm^2 (scanning speed of 500 mm/s) revealed no diffraction contrast (Fig. 4.16 a). Also, the inset of this figure represents a typical ring or halo-like electron diffraction pattern consistent with an amorphous structure. These results along with the resistivity measurements confirmed the retention of amorphous nature with occurrence of structural relaxation in the laser treated metallic glass foils within the laser fluence range of 0.39-0.48 J/mm^2.

Interestingly, although crystallization was not evident within the limits of XRD

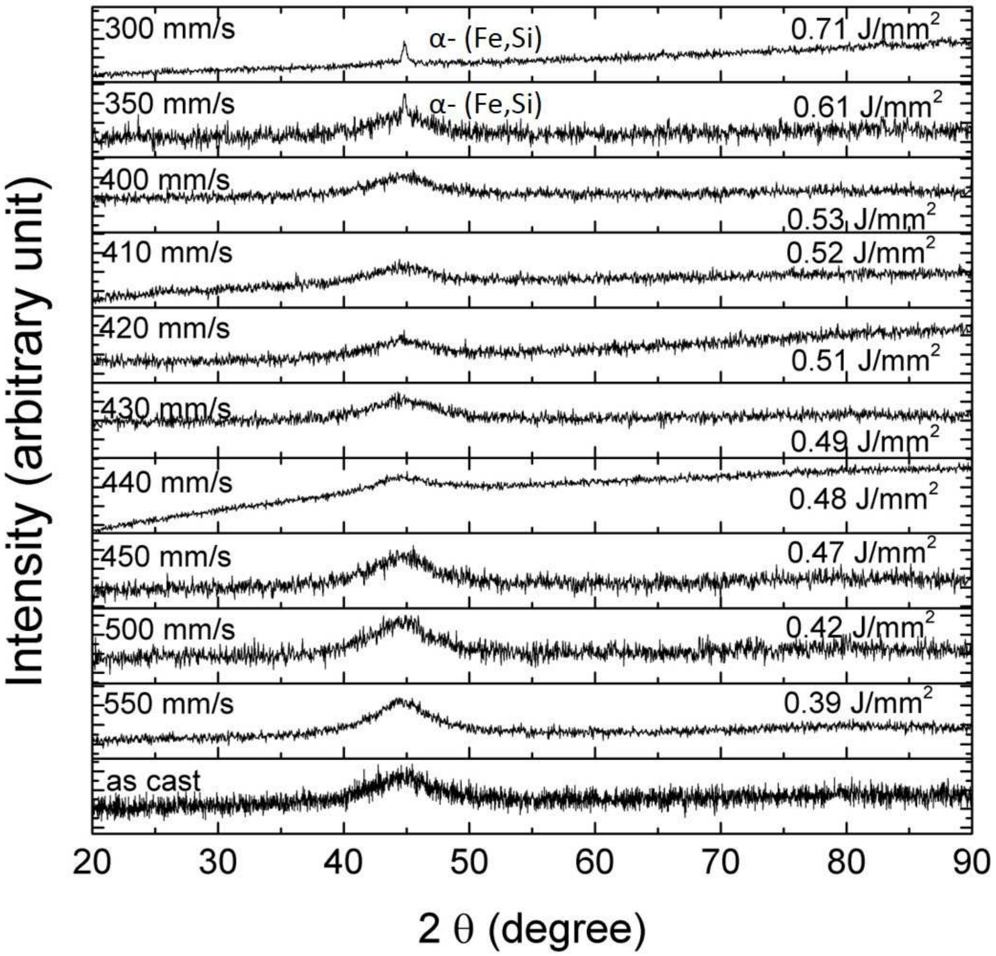

FIGURE 4.15. XRD patterns of Fe-Si-B metallic glass foils subjected to various laser energy inputs investigated during this study on tensile behavior.

analysis of the laser fluences in the range of 0.49-0.53 J/mm^2, it was clearly noticed for the laser fluences of 0.49 J/mm^2 and higher (scanning speed of 430 mm/s and lower) during the TEM analysis of selective laser fluence foils (Fig. 4.16 b-d). This can be attributed to the small fraction (volume) of crystallization as well as very small crystallite sizes in the foils of the laser fluence 0.49-0.53 J/mm^2. The TEM analyses of the foil treated with 0.49 J/mm^2 laser fluence revealed the grain size of 11±3 nm (Fig. 4.4 b) and a predominant presence of α-(Fe,Si) phase (inset of Fig. 4.16 b). These finding were indeed on the lines predicted by the RSM statistical algorithms pointing towards presence of crystallization based on initial qualitative observations of electrical resistivity (Figs. 4.14 and 4.11). The grain size increased marginally with further increase in the laser fluence to 0.61 J/mm^2 (Fig. 4.16 c). Also, for this laser fluence, Fe_2B phase in addition to α-(Fe,Si) phase was detected in the SAD analysis (inset of Fig. 4.16 c). On the other hand, the metallic glass foil thermally treated with the laser fluence of 0.71 J/mm^2 (scanning speed of 300 mm/s) possessed substantially coarse grained microstructure within the laser treated region with the average grain size increasing to 30±6 nm (Fig. 4.16 d). This condition also indicates the presence of α-(Fe,Si) and Fe_2B phases (inset of Fig. 4.16 d). Thus, TEM analyses along with XRD and resistivity data together confirmed that laser treated foils for the fluence range of 0.39-0.48 J/mm^2 retained amorphous structure while undergoing structural relaxation. Whereas increased laser fluence to larger values (0.49-0.71 J/mm^2) led to progressive increase in the crystallization.

In order to better assess the effect of crystallization on mechanical properties of the laser treated foils, firstly the volume fraction of the crystalline phases was quantified using DSC technique. The DSC curves revealed two crystallization events for the as-cast as well as the laser treated conditions (Fig. 4.17) which was also earlier reported in Fe-Si-B metallic glass foils [1, 119]. Reiterating from Section 4.1, the onset of crystallization was at 780 K for the first event and 820 K for the second event. The first crystallization peak corresponds to the formation of α-(Fe,Si) phase whereas the second peak is related to the formation of Fe_3B phase followed by its transformation to Fe_2B intermetallic phase, as reported in the literature [119]. No clear glass transition temperature (T_g) was observed with the employed heating rate of 20 K/s. Notably, the relaxation event was not quantified using the DSC analyses because the glass transition could not be detected. The ternary iron based metallic glasses have been reported to not show a marked glass transition because of a smaller range of temperature for super cooled liquid region ΔT_x, defined as T_x-T_g [144]. Also, in case of foils treated within the fluence range of 0.39-0.48 J/mm^2, the area under the crystallization peaks of the corresponding DSC curves remained identical to that of the as-cast foil indicating the enthalpy of crystallization (ΔH) for these laser treated foils to be the same as that for the as-cast foil. This pointed towards the absence of crystallization during the laser treatments

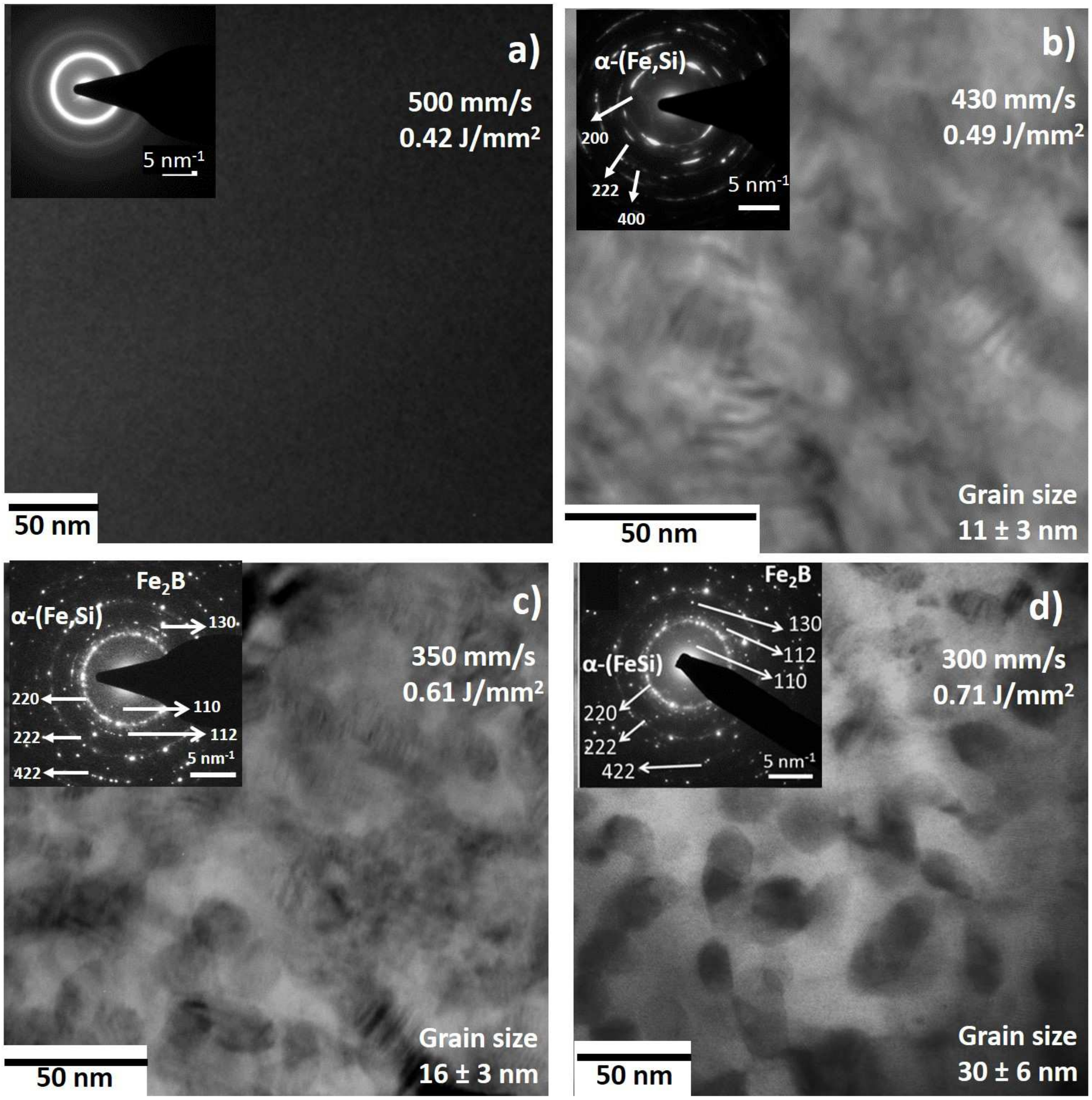

FIGURE 4.16. TEM micrographs and their corresponding SAD pattern in the inset for a) 0.42 J/mm^2 revealing amorphous structure, b) 0.49 J/mm^2, c) 0.61 J/mm^2 and d) 0.71 J/mm^2 laser fluences clearly showing the presence of nanocrystals and the phases formed as a result of crystallization.

corresponding to fluences 0.39-0.48 J/mm^2.

The crystallized phase fractions were computed using Eq. 4.3 are presented in Table 4.2. The overall fraction of crystallization increased with the laser fluence, ranging from the values of 3.7% for the foil treated with 0.49 J/mm^2 fluence to 37% for the foil treated with 0.71 J/mm^2 fluence (Table 4.2). The presence of α-(Fe,Si) phase was evident for all the conditions with its fraction increasing from 3.6% to 31% within the fluence range of 0.49-0.71 J/mm^2. This trend also indicates that α-(Fe,Si) phase formed as a majority component. On the other hand, fraction of crystallization of Fe_2B phase was significantly marginal for the laser fluence range of 0.49-0.52 J/mm^2. Increase in the laser fluence to 0.71 J/mm^2 increased the volume fraction of the crystallized Fe_2B phase to the maximum value of 6%. This fact confirms Fe_2B phase as the minor product of the crystallization process for the laser treated Fe-Si-B metallic glass foils.

In order to clearly realize a trend in the influence of single track laser treatment under various laser fluences on the overall tensile behavior of the test foils, the UTS/fracture strength values of laser treated foils were normalized with respect to the UTS/fracture strength value of as-cast foil and represented as a bar chart in Fig. 4.18. The bar chart can be divided into three distinct regimes. In the first regime, the UTS/fracture strength values were close to the UTS/fracture strength of the as-cast foil. In the second regime, even with some drop, the UTS/fracture strength values of laser treated foil remained comparable to the UTS/fracture strength of the as-cast foil. On the contrary, in the third regime, the UTS/fracture strength values severely reduced. In the first regime, all laser treated foils (0.39-0.48 J/mm^2) except the foil treated with 0.49 J/mm^2 remained mostly in the structurally relaxed condition with retention of amorphous nature. Whereas, the foil treated with the fluence of 0.49 J/mm^2 experienced structural relaxation along with evolution of minor amount of crystallization. Apparently, the structural relaxation and minor fraction of crystallization did not have a marked effect on the UTS/fracture strength values as well as the overall tensile behavior of the foil. This can be attributed to the significantly small fraction of the structurally relaxed volume.

With increasing the laser fluences to 0.49 J/mm^2 and higher values (corresponding to the second and third regimes, respectively), all the samples were crystallized partially. Although the average grain/crystallite size marginally changed up to the laser fluence of 0.61 J/mm^2, the crystallization fraction increased from 5% to 8% in the second regime (fluences corresponding to 0.51 and 0.52 J/mm^2) with α-(Fe,Si) as the major phase. In

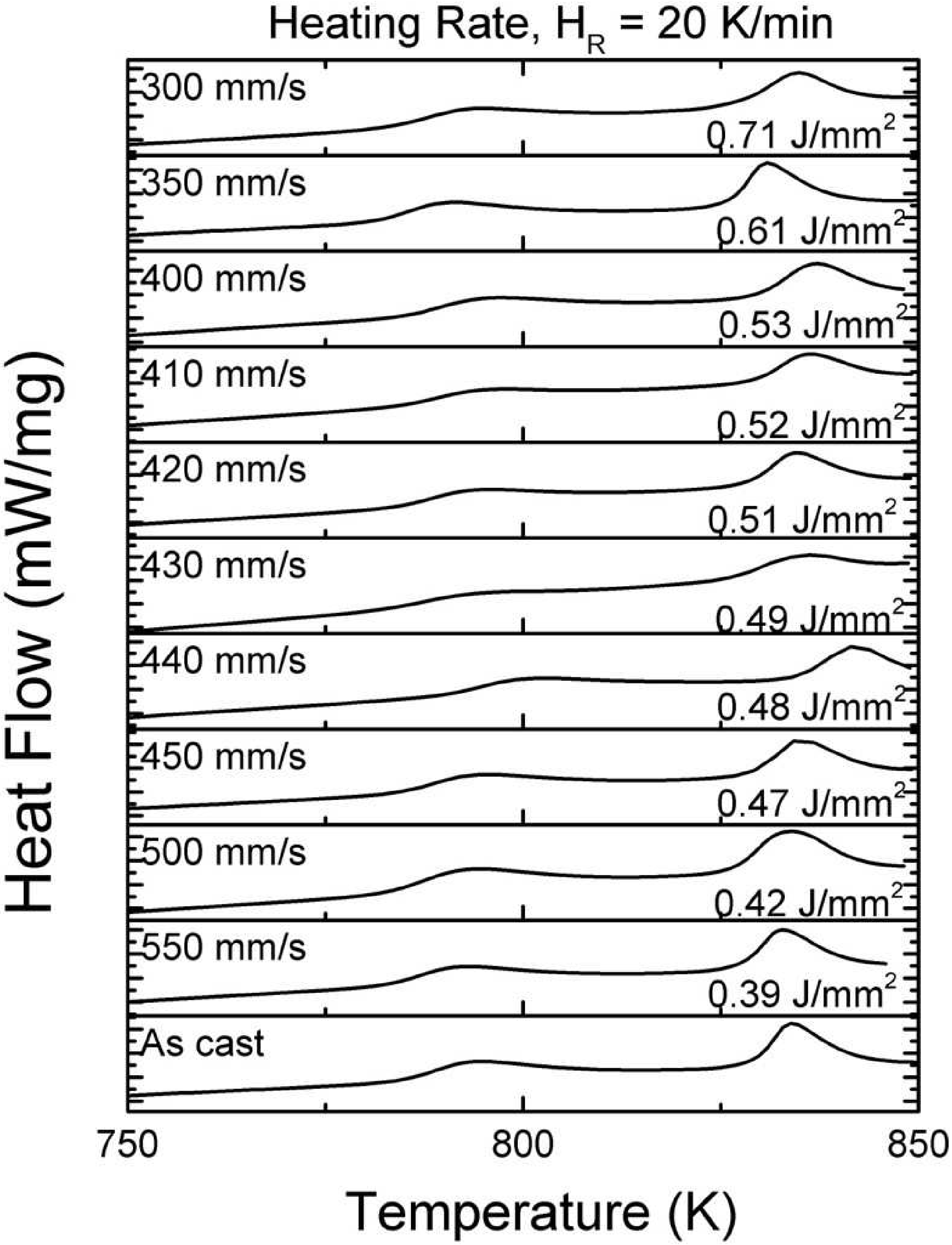

FIGURE 4.17. DSC curves for Fe-Si-B metallic glass foils treated with various laser fluences investigated during study on tensile behavior.

the third regime, the total fraction of crystallization increased substantially (11-37%) with recognizable fraction of Fe_2B (2-6%) phase (Table 4.2). Among all laser fluences, for the laser fluence of 0.71 J/mm^2, the total crystallization fraction reached the highest value with the volume fraction of α-(Fe,Si) and Fe_2B phases as 31% and 6 %, respectively. Also, the average grain/crystallite size of 30±6 nm was much coarser for the laser fluence of 0.71 J/mm^2 compared to all other fluences.

Higher shear modulus of such crystallized phases in comparison to the amorphous matrix are expected to lead to a severe embrittlement in crystallized metallic glasses [25, 26]. Iron and Fe_2B phase have shear moduli of 80 GPa [145] and 140 GPa [146], respectively. The shear modulus of Fe-B based metallic glasses is within the range of 70-75 GPa [147]. Therefore, an embrittlement failure is more pronounced for the laser treated foils with a considerable amount of crystallized Fe_2B phase. Hence, in the second regime, the reduction in strength was likely to be dominated by the crystallization of α-(Fe,Si) phase and the overall increase in the crystallization fraction. In the third regime, however, the presence of hard Fe_2B phase even in small fractions (2-6%) predominantly governed the reduction in strength in combination with the increase in the grain/crystallite size. The hard phases within the amorphous matrix have been reported to act as the crack initiation sites [25, 26] leading to a brittle failure at much lower strengths. Furthermore, the average UTS/fracture strength values along with the are also enlisted in Table 4.2 along with the phase fractions to realize the effects of microstructure evolution on strength of laser treated Fe-Si-B metallic glass samples.

Thus, relaxation and crystallization in small amounts (3.75%) and the grain/crystallite size of the order of 10 nm had a least adverse effect on the tensile behavior of Fe-Si-B metallic glass. Increased volume fraction of the crystallized phases along with the coarsening of grains/crystallites played a dominant role in reducing the strength for the higher laser fluence conditions explored within the current work. Furthermore, the current Section demonstrated ability of coupling processing with statics based RSM algorithms. The predictions made by the RSM desirability function (Fig. 4.14) based on initial quick

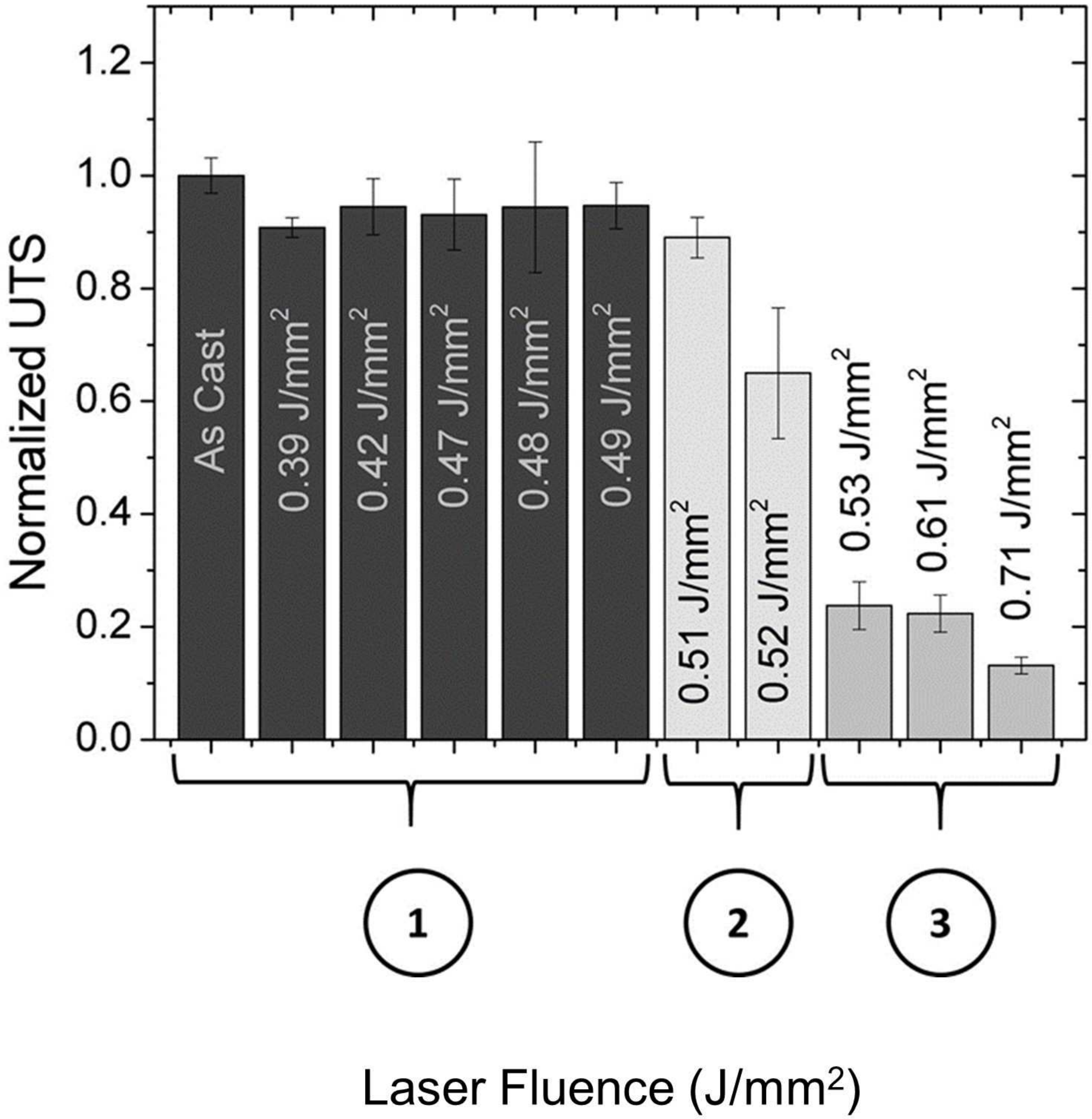

FIGURE 4.18. Normalized UTS/fracture strength values for the Fe-Si-B foils as a function of laser fluence.

qualitative analysis of electrical resistivity measurements (Fig. 4.11) indeed pointed towards a laser processing condition which would lead to crystallization yet retain a high mechanical strength in the laser treated Fe-Si-B metallic glass (Fig. 4.18 and Table 4.2). In addition to assessment and optimization of microstructure-tensile strength relationship, detailed

Table 4.2. Microstructure Development and Tensile Properties of Laser Treated Fe-Si-B Metallic Glass

Laser Fluence J/mm^2	**Scanning Speed** (mm/s)	**α-(Fe,Si) Crystallized Fraction** Vol%	**Fe$_2$B Crystallized Fraction** Vol%	**Average UTS (Fracture Strength)** MPa
Relaxed Metallic Glass Foils (Except as-cast foil)				
0	- (as-cast foil)	-	-	2310±70
0.39	550	-	-	2100±40
0.42	500	-	-	2185±115
0.47	450	-	-	2155±145
0.48	440	-	-	2183±260
Crystallized Metallic Glass Foils				
0.49	430	3.6	0.15	2190±95
0.51	420	5.5	0.17	2050±80
0.52	410	8	0.6	1510±270
0.53	400	9	2	550±100
0.61	350	18	3	515±75
0.71	300	31	6	300±30

fractographic analyses were performed on the tensile tested samples. The following sections presents the findings of fracture behavior and effects of tensile loading on crystallization behavior of laser treated Fe-Si-B metallic glass.

4.3. Effects of Tensile Loading on Crystallization of Laser Treated Fe-Si-B Metallic Glass [3]

The current section explores effects of tensile loading on structural changes within as-cast, laser treated structurally relaxed, and laser treated partially crystallized Fe-Si-B metallic glass. Observations of fracture surfaces for these various conditions have been presented. Moreover, site specific TEM studies of the fracture surface have been performed to realize effects such as localized crystallization and crystallite/grain growth within the fracture region. These observations have been analyzed in light of combined effect of stress and temperature developed at the region of fracture.

The results presented here are for the representative samples from the previous Section. As discussed, three distinct regimes of UTS/fracture strength were observed as

---

[3] The content of this section has been previously published in part in author's publication: Joshi, Sameehan S., et al. "Crystallisation behaviour during tensile loading of laser treated Fe–Si–B metallic glass." Philosophical Magazine 97.7 (2017): 497-514. (Reproduced with permission from Taylor & Francis.)

a function of laser fluence in case of laser thermal treated Fe-Si-B metallic glass. In the first regime (laser fluence of 0.39-0.48 J/mm^2), Fe-Si-B metallic glass foils were structurally relaxed while retaining amorphous structure, whereas in the second regime (laser fluence of 0.49-0.52 J/mm^2) they were partially crystallized with α-(Fe,Si) as the predominant phase, and in the third regime (laser fluence of 0.53-0.71 J/mm^2) they were partially crystallized with α-(Fe,Si) as the major phase along with considerable amounts of brittle Fe_2B phase. As a result, the value of UTS/fracture strength remained close to the as-cast Fe-Si-B metallic glass foil in the first regime, followed by a slight decrease in the second regime, and severe loss of the UTS/fracture strength value in the third regime. The investigation in this Section was mainly focused on the overall effect of the tensile loading on the secondary crystallization and crystal growth/coarsening behavior of the laser treated Fe-Si-B metallic glass with and without pre-existing crystallization. Hence, the samples representing each regime of the microstructure development from the previous Section were taken into consideration during the present effort and were compared against the as-cast Fe-Si-B metallic glass foil. The summary of microstructure and tensile behavior corresponding to these three samples is presented in Table 4.3. The results about effect of tensile loading on structural changes within these samples have been presented in the upcoming subsections.

TABLE 4.3. Summary of Microstructure and Tensile Behavior of Laser Treated Fe-Si-B Metallic Glass Foils Selected for Investigating Effects of Loading on Crystallization.

Laser Fluence (F) J/mm^2	Scanning Speed (V) mm/s	α-(Fe,Si) Crystallized Fraction Vol%	Fe_2B Crystallized Fraction Vol%	Total Crystallized Fraction Vol%	Nature of Stress Strain Curve	Ultimate Tensile Strength MPa
as-cast foil	-	-	-	-	Linear	2310 ± 70
0.42	500	-	-	-	Linear	2185 ± 115
0.49	430	3.6	0.15	3.75	Linear	2190± 100
0.71	300	31	6	37	Linear	320 ± 30

4.3.1. Fracture Behavior

The current subsection explores effect of laser treatments on fracture surface morphology and in turn the crystallization. On a side note, as a starter Fig. 4.19 represents

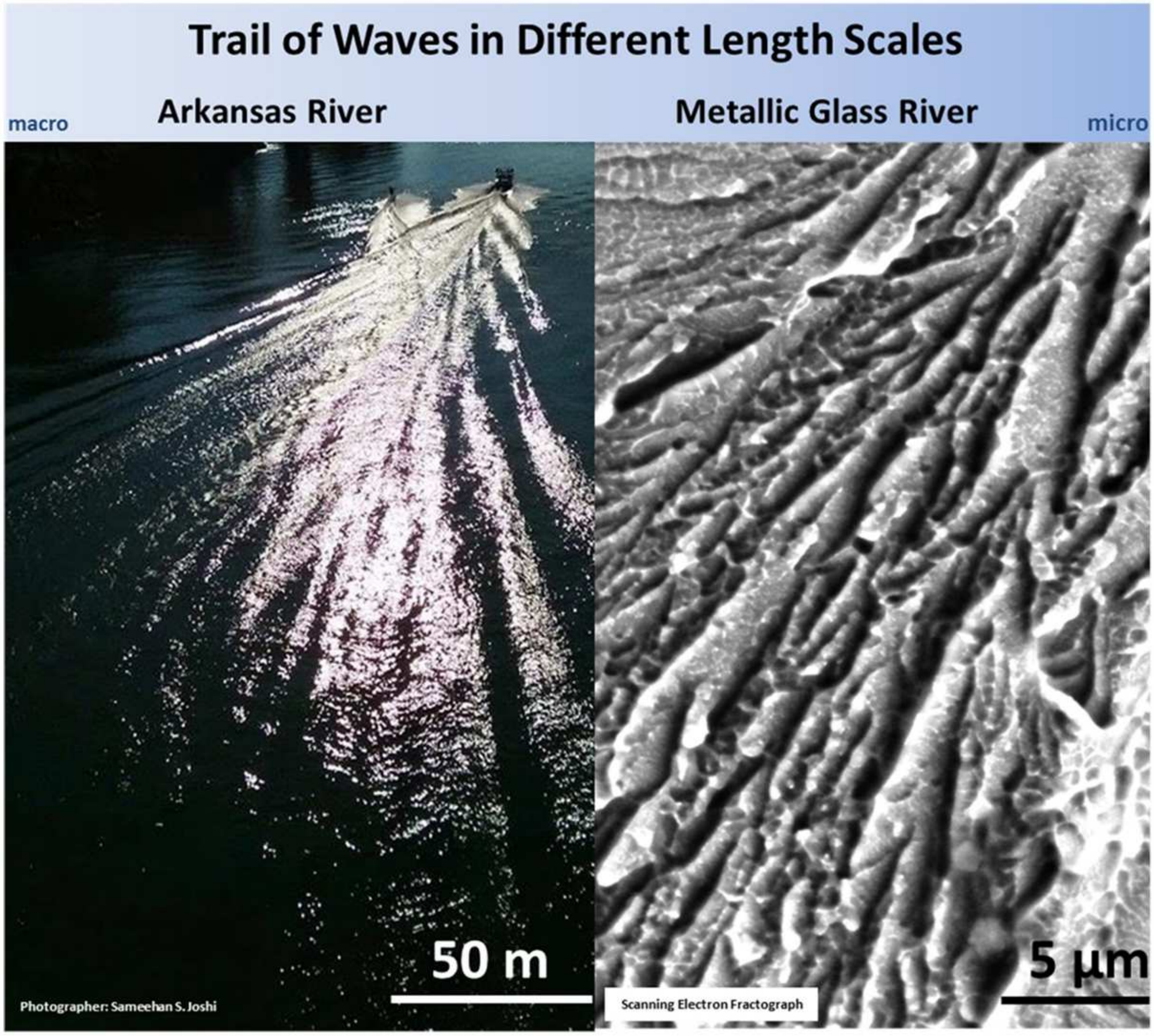

FIGURE 4.19. Set of images showing trail of waves in different length scales. Image on the left is a photo of trails/pattern created by a boat and a surfer traveling on water surface. Correspondingly, image on the right shows the pattern created by crack traveling within metallic glass during fracture.

the love of nature towards fractal patterns. Image on the left is a photograph of Arkansas River taken using a cell phone camera by the author. Moving boat and a surfer act like stress concentrators to create the trail of waves in water. Image on the right is a scanning electron microscope micrograph of a fracture surface of a metallic glass. The localized temperature rise and stress concentration at the crack tip during the fracture produce a pattern similar to the trail of waves at micro-scale.

4.3.1.1. Microscopic Features of Fractured Region

4.3.1.1.1 Surface Morphology

The fractured surface observation using secondary electron detector of SEM revealed a vein pattern for the as-cast foil with an average vein spacing of 1 ± 0.2 μm (Fig. 4.20 a). Such a pattern has been attributed to local softening within the shear bands [20, 148]. Because of the applied stress, shear-induced structural disordering of the localized volume takes place on the shear plane [20]. Furthermore, temperature rise also contributes towards softening of the material on the shear plane [148]. This softening was considered to be instrumental for rapid initiation and propagation of crack resulting in vein like features on the fractured surface of a metallic glass.

The tensile fractograph of the sample corresponding to laser fluence of 0.42 J/mm^2 also indicated the presence of vein pattern (Fig. 4.20 b). However, the spacing between the veins reduced (average vein spacing of 0.45 ± 0.09 μm) indicating reduction in toughness [149, 150] and UTS/fracture strength values compared to the as-cast metallic glass (from ∼2310 MPa to ∼2185 MPa) (Table 4.3). The structural relaxation of metallic glass has been reported to redistribute and decrease the free volume (the excess atomic scale voids in the glassy material compared to its crystalline counterpart) within the relaxed region [151]. This fact results in increased resistance to the nucleation of shear bands leading to the embrittlement of the material while at the same time indicating the presence of shear deformation [31, 152–156]. Moreover, as the structurally relaxed volume in the laser treated region of 0.6 mm width and 50 mm length was much smaller than the entire bulk of the amorphous sample of 90 mm length and 12 mm width. Therefore, even though the fracture surface observations indicated embrittlement upon structural relaxation, the overall UTS/fracture strength of the structurally relaxed laser treated Fe-Si-B metallic glass foils still remained closer to the UTS/fracture strength of the as-cast metallic glass foil.

With an increase in laser fluence to 0.49 J/mm^2, the fracture surface morphology changed to a mixture of chevron and vein pattern (Fig. 4.20 c) indicating further embrittlement [157, 158]. The spacing between the veins within this pattern appears much

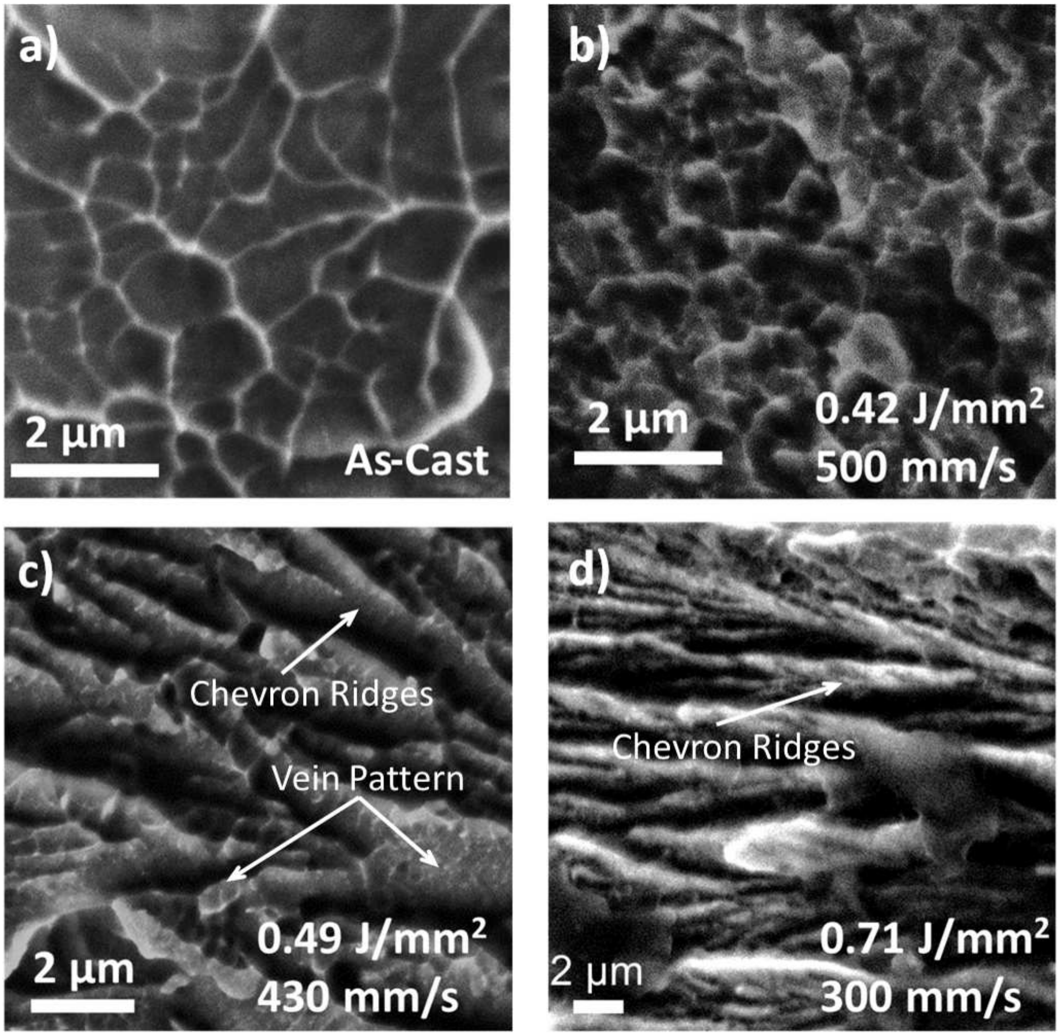

FIGURE 4.20. SEM fractographs recorded at the operating voltage of 15 keV using Everhart-Thornley secondary electron detector showing fracture surface of (a) as-cast foil revealing a vein pattern and (b) 0.42 J/mm^2 (500mm/s), (c) 0.49 J/mm^2 (430 mm/s), and (d) 0.71 J/mm^2 (300 mm/s) laser treated metallic glass foils revealing a variation in fracture surface morphology.

less (0.25 ± 0.08 μm) compared to the vein spacing obtained in as-cast and 0.42 J/mm^2 laser treated sample (Fig. 4.20 a, b, and c). This indicates the presence of shear deformation but at a much finer scale. Such fine veins along with chevron ridges are the signature of embrittlement. With further increase in the laser fluence to 0.71 J/mm^2 the fracture surface revealed a pure chevron pattern (Fig. 4.20 d) which is an indication of a severe embrittlement of the sample. This is clearly manifested in substantial drop in the UTS/fracture strength value (~320 MPa) (Table 4.3) which was attributed to secondary crystallization of hard Fe_2B phase leading to crack initiation [150]. The chevron ridges in this sample are much thicker (2.3 ± 0.6 μ m) compared to the sample treated with 0. 49 J/mm^2 (which is 1.3 ± 0.2 μm).

4.3.1.1.2 Structural Changes Evolved upon Tensile Loading

As mentioned in Chapter 2, the thin foils for TEM studies were lifted out using FIB from the site specific locations within the fracture region and a region away from the fracture of the tensile loaded as-cast and laser treated metallic glass samples. The locations of lift out in the case of laser treated samples are represented by regions I and II, respectively in (Fig. 3.6 a). The exact sites of these locations for preparation of FIB lift out samples are presented in the high magnification views in (Fig. 3.6 b and c). In the case of as-cast Fe-Si-B metallic glass sample, TEM micrographs from the location away from the fractured region completely lack diffraction contrast (Fig. 4.21 a). The SAD ring pattern corresponding to this region is indicative of the retention of amorphous structure (inset of Fig. 4.21 a). Similarly, the TEM observation corresponding to the fractured region revealed an absence of diffraction contrast (Fig. 4.21 b). The ring SAD pattern corresponding to this region further confirmed the retention of amorphous structure even after undergoing fracture under tensile loading (inset of Fig. 4.21 b). Although the sample corresponding to laser fluence of 0.42 J/mm^2 underwent structural relaxation due to laser thermal treatment (drop in UTS/fracture strength of nearly 5% compared to as-cast sample, Table 4.3), it appeared to retain the amorphous structure upon laser thermal treatment. The TEM analyses of this sample corresponding to both the region away from the fracture (Fig. 4.21 c) and within the fracture of laser thermal treated volume (Fig. 4.21 d) confirmed the complete absence of crystallization.

Furthermore, with an increase in laser fluence within the range of 0.49-0.71 J/mm^2, the laser thermal treatment resulted in crystallization of the metallic glass foils (Fig. 4.21 e-h). In several earlier works, similar observations for crystallization in laser thermal treated Fe-Si-B metallic glasses were made [1, 42, 43]. Similarly in the present study, the SAD pattern indicated the evolution of α-(Fe,Si) as the major crystalline phase in case of the

0.49 J/mm^2 laser fluence condition both in the fracture region and the region away from the fracture within the laser treated volume (inset of Fig. 4.21 e and f). However, the TEM analyses also indicated that the crystallite/grain size within the fractured region experienced significant coarsening (40 ± 11 nm, Fig. 4.21 f) compared to the crystallites/grains (11 ± 3 nm) in the region away from fracture (Fig. 4.21 e). The sample corresponding to 0.71 J/mm^2 also followed the same trend as that for 0.49 J/mm^2 with a significant crystallite/grain growth/coarsening (76 ± 21 nm) within the fractured region (Fig. 4.21 h) compared to the crystallites/grains (29 ± 6 nm) in the region away from fracture (Fig. 4.21 g). However, under a higher laser fluence (0.71 J/mm^2) treatment, in addition to α-(Fe,Si) crystallite phase, Fe_2B crystallite phase separation also occurred (inset of Fig. 4.21 g and 4.21 h). Furthermore, the process of grain size measurement is also illustrated on micrographs in Fig. 4.21 g and h. These observations emphasize the significant effect of the tensile loading on the evolution of type and size of the crystallite/grain within the fractured region of the partially crystallized laser thermal treated Fe-Si-B metallic glass foils.

4.3.2. Thermomechanical Effects Induced during Tensile Loading

The effects of generation of stress and temperature during tensile loading on the crystallite/grain size and its growth/coarsening can be distinctly realized through comparison of TEM observations of 1) laser thermal treated region of the sample that was not subjected to tensile loading, 2) laser thermal treated region away from the fracture of the sample which was subjected to tensile loading, and 3) fracture region of laser thermal treated sample that was subjected to tensile loading. Both the laser thermal treated region of the sample that was not subjected to tensile loading (0.71 J/mm^2, Fig. 4.22) and the laser thermal treated region away from the fracture of the sample that was subjected to tensile loading (0.71 J/mm^2, Fig. 4.21 g) contained the crystallites/grains of nearly the same size (∼29 nm). This is an indication of the fact that even though stress (thermal) and temperature developed in these regions caused crystallization and crystallite/grain growth/coarsening to a certain size (∼29 nm), additional global mechanical stresses generated during tensile loading in this region were not high enough to trigger further growth/coarsening of these crystallites/grains.

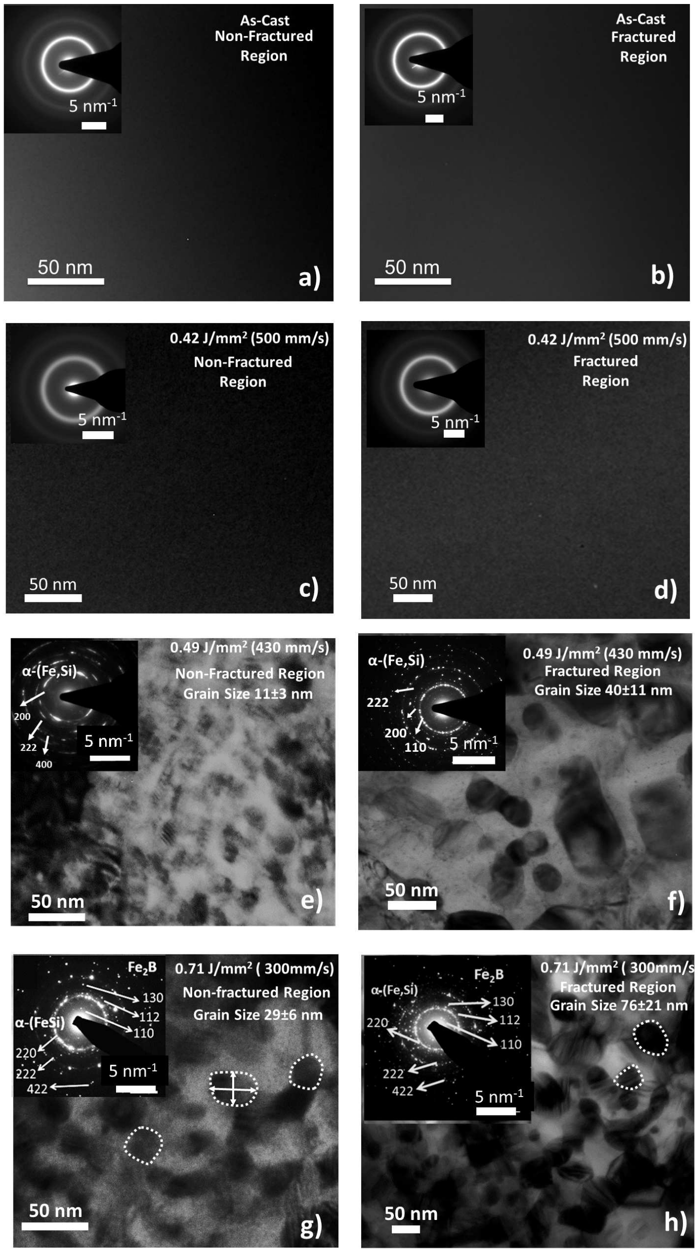

Figure 4.21. Set of TEM micrographs and the SAD patterns in the inset showing microstructures of (a) - (b) as-cast Fe-Si-B metallic glass foil, (c) -(d) Structurally relaxed laser treated Fe-Si-B metallic glass foil, and (e) - (h) partially crystallized laser treated Fe-Si-B metallic glass foils. The images on the left column represent the microstructure from the location away from the fractured surface, whereas images on the right column correspond to the microstructure at the fractured surface of these samples. In addition, the process of grain size determination has been depicted in Fig. 3(g) and (h) where few grains are marked by a dotted boundary. Further, the linear measurement for grain size determination in horizontal and vertical directions has been illustrated using arrowed lines in one of the grains.

On the contrary, as stated earlier, TEM observation of the fracture region of the same laser thermal treated sample that was subjected to tensile loading (0.71 J/mm^2) indicated the presence of crystallites/grains with the average grain size of 76 ± 21 nm (Fig. 4.21 h) that are nearly 2.5 fold larger than the crystallites/grains compared to both the laser thermal treated region of the sample that was not subjected to tensile loading (0.71 J/mm^2, Fig. 4.22) and the laser thermal treated region away from the fracture of the sample subjected to tensile loading (0.71 J/mm^2, Fig. 4.21 g).

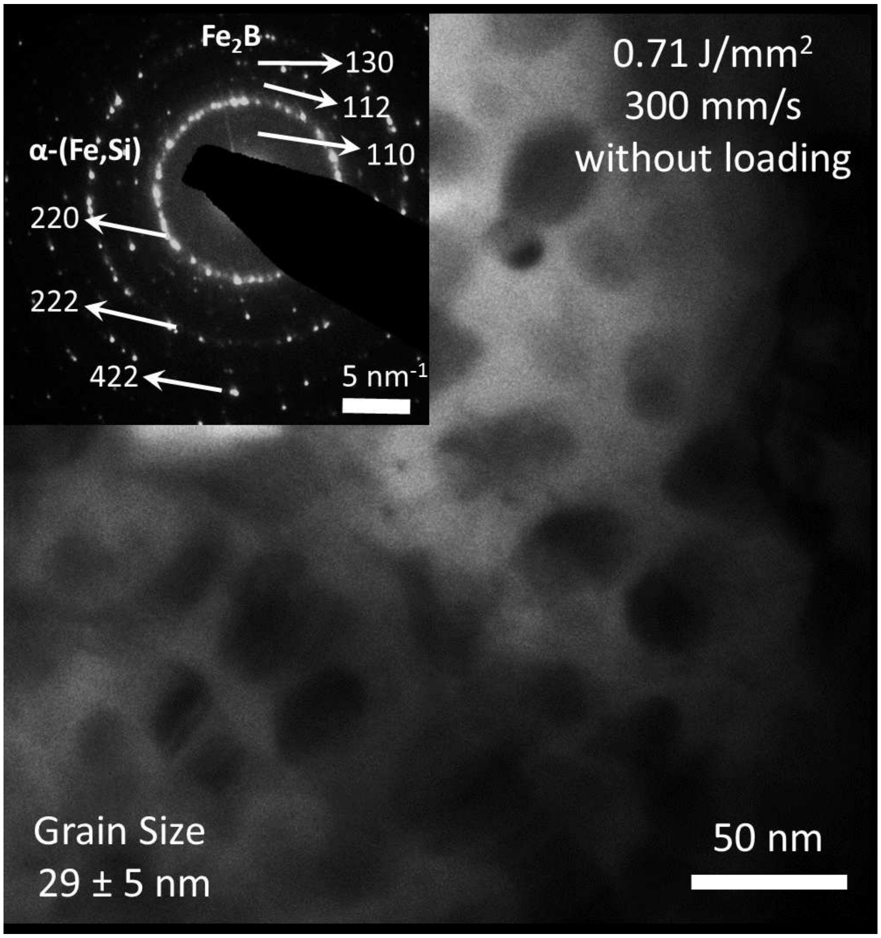

FIGURE 4.22. TEM micrograph of laser thermal treated Fe-Si-B metallic glass foil corresponding to laser fluence of 0.71 J/mm^2 without any loading.

This observation clearly points toward the fact that localized stress and temperature developed in the fracture region reached the magnitudes which support further growth/coarsening of the crystallites/grains in that region. It has been reported in the case of nanocrystalline alloys that the applied stress can cause a stress assisted grain growth

[159–162]. Such observations have been made in the case of tensile loading [162, 163], compressive loading [164, 165], and indentation experiments [159, 166]. However, the testing conditions employed during present tensile loading experiments apparently lacked any significant effect on growth/coarsening of the average crystallite/grain size within the region away from the fracture area of the laser treated partially crystalline Fe-Si-B metallic glass foils.

The above observations tend to indicate that the current tensile loading conditions exerted minimal or no direct effect on crystallization and/or crystallite/grain growth/coarsening of as-cast, structurally relaxed, and the partially crystallized Fe-Si-B metallic glass. On the contrary, fracture process exerted a significant influence on crystal/grain growth/coarsening within the fracture region of partially crystallized metallic glass. This situation can be evaluated on the basis of two possible secondary effects induced by tensile loading on Fe-Si-B metallic glass: (i) temperature rise within the fracture region and (ii) fracture induced stress assisted grain growth. During tensile loading, shear band transition zones form on a shear plane which is usually at 45° to the loading axis (Fig. 4.23 a). This fact leads to the formation of shear bands (10-20 nm thick [16]) followed by a single shear band extending throughout the cross section leading to crack formation (Fig. 4.23 b) [26]. A significant heating has been reported during such a fracture process. The temperature rise during fracture was estimated using Eq. 2.4 and presented as a function of time at distance x = 1 nm along the centerline of the shear band (x axis) (Fig. 4.23 c) , and as a function of distance orthogonal to the centerline of the shear band (y-axis) at time = 1 ns (Fig. 4.23 d). The values of thermophysical properties employed for performing these calculations using Eq. 2.4 were ρ= 7180 kg/m^3 [42] and C$_p$= 500 J/(kgK) [108]. The value of parameter H for the present Fe based metallic glass was 1000 J/m^{-2} which was based on yield strength and shear offset (the relative movement between two sides of the shear band) of the metallic glass [167]. The value of α was calculated using $\alpha = \frac{k}{\rho C}$, where k was the thermal conductivity. The value of k for the present composition has been reported as 9 W/(mK) [42, 101, 102].

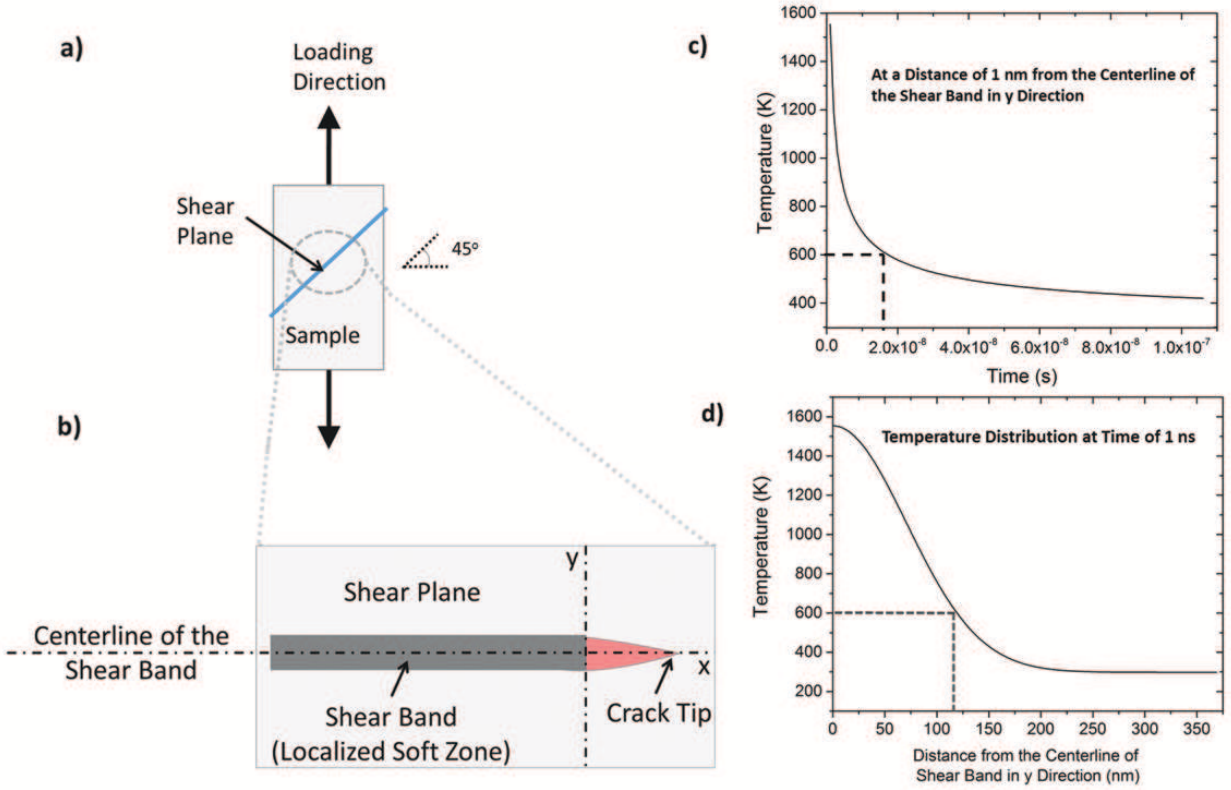

FIGURE 4.23. Set of figures showing (a) schematic of a Fe-Si-B metallic glass sample undergoing tensile loading, (b) schematic of shear band extending into a crack, (d) temporal distribution of temperature from the center of a shear band at distance of 1 nm, and (c) spatial distribution of temperature time of 1 ns from the center of the shear band.

Both the temporal (Fig. 4.23 c) and spatial distribution (Fig. 4.23 d) of the temperature indicated instantaneous maximum temperatures of the order of 1500 K. However, the time frames were of the order of tens of nanoseconds before it dropped to room temperature as a result generating cooling rates of the order of 10^8 K/s. At the same time, it has also been estimated that heating rates would also be extremely rapid and of the same order as the cooling rates during such laser thermal treatment. The crystallization of amorphous materials is a heating rate dependent process [45, 124, 125]. In addition, the temperature rise during fracture is dynamic in nature and the material undergoes extremely rapid heating and cooling cycles through a peak temperature attained only for an extremely short duration (fraction of nanosecond). In light of this, in the case of as-cast and structurally relaxed Fe-Si-B metallic glass foils, even though the instantaneous peak temperatures reached were significantly high ($\sim$ 1500 K), the extremely rapid temperature variation prevented the crystallization of Fe-Si-B metallic glass to be observable within the resolution of few nanometers. Notably, SEM observations of fracture surface revealed the localized plasticity in the form of vein patterns (Fig. 4.24 a).

In the case of partially crystallized Fe-Si-B metallic glass foils, apart from temperature rise, stress also played a key role in determining the response of the material. The average plastic strain experienced by the crystallites/grains within the fractured regions can be estimated according to Eq. 4.11

$$\epsilon = \left(\frac{X_f - X_i}{X_i}\right) \tag{4.11}$$

where X_f is the final grain size, X_i is the initial grain size.

As only the samples laser heat treated with fluences of 0.49 and 0.71 J/mm^2 indicated localized crystallite/grain growth/coarsening within the fractured region, the values of localized strain corresponding to these fluences calculated from Eq. 4.11 have been tabulated in Table 4.4. The computed values of localized strain (Table 4.4) indicate that at localized level the material underwent extensive plastic deformation (165-263 %). Some of the crystallites/grains also indicated signs of preferential elongation as clearly detected during TEM observations in Fig. 4.24 b and Fig. 4.24 c. Furthermore, these crystallites/grains revealed the presence of twin like features within them. It is interesting to note here that the presence of shear localization has also been reported in the case of body centered cubic (bcc) nanocrystalline alloys [168, 169]. The shear bands form by sliding between several aligned grain boundaries [159]. This shear gets extended to the crystallites/grains within the propagation path of the shear bands by inter-granular slip. Furthermore, this slip has been reported to emit partial dislocations which leave extended stacking faults along their propagation path and may also lead to twinning [159]. In the case of bcc iron, it has been reported that twinning occurs when there is a stress concentration at the head of piled up dislocations [170]. Furthermore, a minor twinning activity has been observed for Fe-5wt%

Si alloys at room temperature and strain rate of 10^{-3}/s (similar to the present investigation) [171]. The observed twin system was {112} [111]. Thus, even though the SAD patterns obtained during TEM observations of the fractured regions of laser thermal treated partially crystallized Fe-Si-B metallic glass did not reveal the presence of twins at the length scales involved in the present work, the visual observations coupled with findings in the literature [171] do support formation of twins in some of the crystallites/grains within the fractured regions of these foils.

Table 4.4. Estimated Localized Strain and Activation Energy of Crystallite/Grain Growth

Laser Fluence (F) J/mm^2	Scanning Speed (V) mm/s	Initial Grain Size (X_i) nm	Final Grain Size (X_f) nm	Localized Strain %	Activation Energy kJ/mol
0.49	430	11 ± 3	40 ± 11	263	100
0.71	300	29 ± 6	76 ± 21	165	89

The observations noted above suggested the role of stress along with the temperature in crystallite/grain growth/coarsening within the fractured region of the partially crystallized laser thermal treated (0.49 and 0.71 J/mm^2) Fe-Si-B metallic glass. The kinetics of a crystallite/grain growth/coarsening is expressed according to Eq. 2.1 [69]. The value of n was assumed to be 0.5. It has been reported in the literature that $n = 0.5$ holds in good agreement for the iron based systems during crystallite/grain growth/coarsening in a sub hundred nanometer regime [7]. Furthermore, it has been reported in the case of nanocrystalline Fe that no significant crystallite/grain growth occurs below 600 K [69]. Thus, to estimate the effect of tensile loading on the activation energy of crystallite/grain growth in the present case, the temporal distribution of temperature in the neighborhood away from the shear band was considered. The average temperature between peak temperature ($\sim$ 1500 K) and 600 K was considered in the computations. As a first level of approximation, the total time of crystallite/grain growth/coarsening was considered as the time at which temperature was 600 K (1.8x10^{-8}s). Again, as only the samples laser heat treated with fluences of 0.49 and 0.71 J/mm^2 indicated localized crystal/grain growth/coarsening within the fractured region, the values of activation energy in the localized region of fracture corresponding to these fluences were computed using Eq. 2.1 and are presented in Table 4.4. The estimated values of the activation energy of grain growth for both fluences (Table 4.4) were much lower than the reported value of 248 kJ/mol [69]. Furthermore, these values were also lower than the activation energy of 222 kJ/mol for the diffusion of silicon in α iron [172]. However, these values are lower than but closer to the activation energy of 177 kJ/mol for grain boundary self diffusion of Fe [172]. This indicates that, grain boundary dependent diffusion (migration) play a critical role during crystallite/grain growth/coarsening during fracture of laser thermal treated partially crystalline Fe-Si-B metallic glass. Such a behavior is assisted by the application of stresses which further can reach much higher values at the crack tip [173]. As a result, the estimated activation energy values are much lower than the observed values for static grain growth/coarsening.

Thus, the localized plastic deformation in Fe-Si-B metallic glass was realized with the presence of vein pattern (Fig. 4.24 a). Upon partial crystallization induced by laser thermal treatment, the nanocrystals at the fracture surface experienced stress enhanced crystallite/grain growth/coarsening assisted by a rapid heating/cooling cycle. Some of the crystallites/grains also indicated preferential elongation demarcated by arrows and twin like deformation features presented in Fig. 4.24 b-c suggesting a favorable orientation of such grains with respect to the loading [161, 162]. Similar to the observations of the present work, stress induced lowering of the activation energy of crystallite/grain growth/coarsening was also observed before in the case of Fe-Si-B system [27, 94].

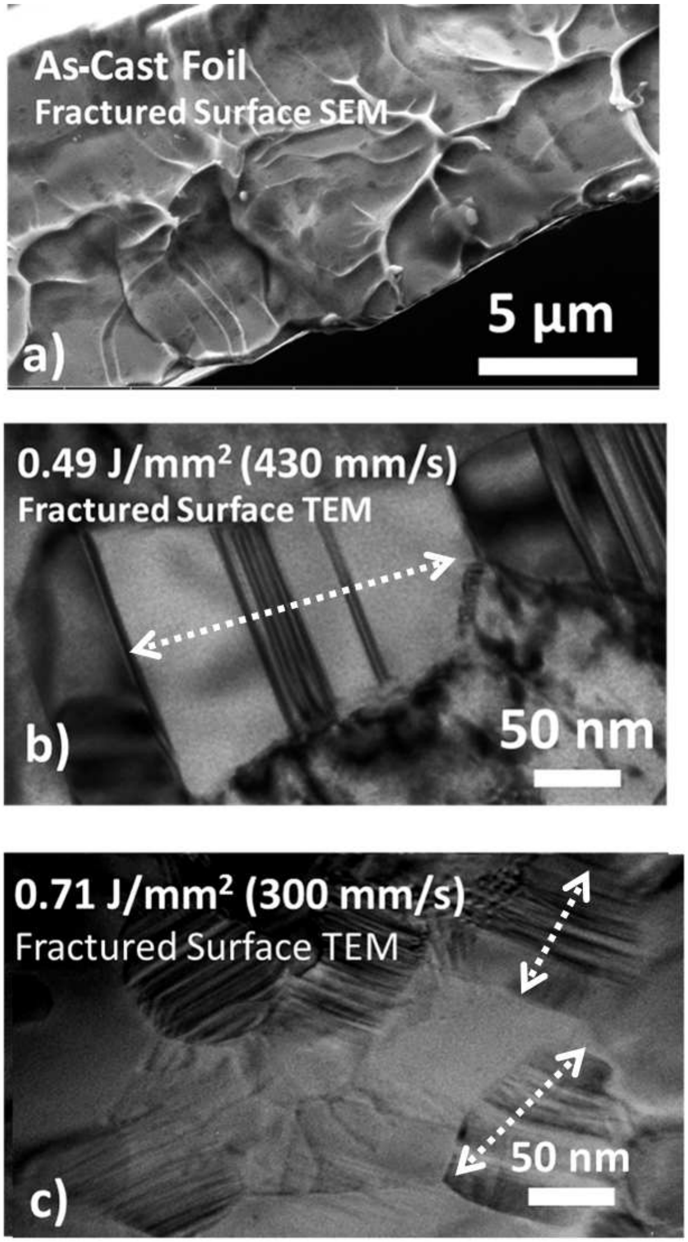

FIGURE 4.24. Illustration of localized plasticity in Fe-Si-B metallic glass foils showing (a) SEM micrograph of extended veins in as-cast Fe-Si-B metallic glass foil, (b), and (c) TEM micrographs corresponding to laser fluence of 0.49 and 0.71 J/mm^2 respectively showing step like features and elongated deformed grains as indicated by the arrow markers.

CHAPTER 5

CONCLUDING REMARKS

The current work explored influences of thermokinetic conditions imposed during laser thermal treatments on crystallization, microstructure evolution, and tensile behavior of Fe-Si-B metallic glass. Moreover, effects of tensile loading on crystallization of laser thermal treated Fe-Si-B metallic glass were also investigated. After comprehensively through results and discussions in Chapter 4, the current Chapter provides important conclusions of the work. The conclusions are also subdivided as per the objectives of the work defined in Chapter 1.

5.1. Structural Changes and Phase Evolution

- Fe-Si-B based metallic glass foils treated with the lower laser fluences in the range of 0.39–0.48 J/mm^2 (scanning speed 550-440 mm/s) underwent structural relaxation within the treated region.
- Fe-Si-B based metallic glass ribbons treated with laser fluence in the range of 0.43 - 0.9 J/mm^2 (scanning speed 430-235 mm/s) underwent crystallization.
- Formation of nano crystallites within the laser treated region was confirmed from XRD spectra and supported by TEM analysis. The crystallite size increased initially with laser fluences and stabilized at 32 nm for higher fluences.
- Crystallization led to formation of α-(Fe,Si) as the major component, and Fe_2B as the minor component. Fraction of crystallization steadily increased with increase in laser fluence.
- The behavior of crystallite formation and growth was influenced by dynamic nature of the laser processing. Faster heating rates of the order of 10^5 K/s resulted in shift in crystallization onset temperatures to much higher level (1089 to 1110 K as a function of scanning speed).
- An upward shift in crystallization temperature was followed by attainment of peak temperature (varying from 1460 to 1240 K with increase in scanning speed) and

termination of laser treatment.

- Rapid cooling of the similar order as that of heating rates, hereafter prematurely arrested the crystal growth.
- The predicted arrest temperature decreased from 950 to 913 K with increase in laser beam scanning speed.
- Temperature difference between peak temperature and arrest temperature, ΔT and total time of growth, Δt decreased with scanning speed as a result, giving much finer crystallite size (in the range of 11 to 32 nm) within the laser treated regions of the Fe-Si-B metallic glass foils .

5.2. Tensile Behavior

- The structural relaxation did not change the overall tensile behavior and the UTS/fracture strength values of the laser treated metallic glass foils.
- The total crystallization fraction of 3.75% and grain size of the order of 10 nm (corresponding to the laser fluence of 0.49 J/mm^2) did not affect/have significant impact on the tensile behavior of the foils.
- A further increase in laser fluences to 0.51 and 0.52 J/mm^2 marginally reduced the UTS/fracture strength of the foils owing to the total crystallization fractions of 5.6–8.6%.
- Laser treatments of the foils involving fluences of 0.53-0.71 J/mm^2 led to crystallization fractions of 11-37% comprising of minor amounts (2-6%) of hard Fe_2B phase resulting in severe reduction of the UTS/fracture strength of the laser treated foils.
- Grain size increase also contributed to this reduction in case of the foil treated with 0.71 J/mm^2.
- Although all the foils failed in a brittle manner, the fracture morphology in the laser treated region changed. The as cast foil possessed a characteristic vein pattern morphology within the fractured surface. The structurally relaxed samples also revealed the vein pattern, however, the spacing between veins were much smaller

compared to as cast foil.

- There was a transition from vein pattern to a mix of vein and chevron pattern and gradually to a complete chevron pattern for the partially crystallized samples as a function of laser fluence.

5.3. Effect of Loading on Crystallization

- Tensile loading had a minimal or no effect on the crystallization of as-cast and structurally relaxed (laser fluence = 0.41 J/mm^2) Fe-Si-B metallic glass.
- The average crystallite/grain size of a partially crystallized Fe-Si-B metallic glass foils remained unaltered after tensile loading.
- A significant grain growth was observed in the fractured region of these partially crystallized laser thermal treated metallic glass foils (from 11 ± 3 nm to 40 ± 11 nm in 0.49 J/mm^2 sample and from 29 ± 6 nm to 76 ± 26 nm in case of 0.71 J/mm^2 sample).
- Such a grain growth behavior in fractured region was attributed to the temperature rise during fracture of the Fe-Si-B metallic glass combined with the associated stress effects which resulted in localized lowering of the activation energy for grain growth.

CHAPTER 6

FUTURE SUGGESTIONS

In light of the current findings on evolution of crystallization during laser thermal treatments [42], tensile behavior [150, 174], and effects of loading on crystallization of laser treated Fe-Si-B metallic glass [175] coupled with previous findings about the magnetic response of the same material [1, 27, 43, 44]; the author would like to propose the following tasks as a future continuation of this work:

(1) *DSC Analysis using Various Heating Rates*: As discussed in Chapter 4, no clear glass transition was observed during DSC experiments on as-cast and laser treated metallic glass foils. Such a behavior was attributed to the closeness of glass transition and crystallization temperatures, thus, not capturing the event of glass transition at the heating rate of 20 K/min. In light of this, the author proposes a comprehensive DSC analyses at various heating rates (preferably lower than 20 K/min) to capture the event of glass transition during DSC runs. This will aid in quantification of structural relaxation in terms of relative fraction of free volume as well as estimation of activation energy of crystallization by suitable analysis methods such as Ozawa or Kissinger analysis.

(2) *Laser Patterning*: The author proposes exploration of laser patterning of Fe-Si-B metallic glass as a next natural step to the single linear laser track treatments from the manufacturing point of view. Such experiments will be able to synthesize flexibly the crystalline packets within the amorphous matrix. Especially, the laser treatments can be carried out with sufficient separation between the laser treated regions (to eliminate/minimize the reheating effects) and with laser processing parameters leading to predominant evolution of α-(Fe,Si) phase to avoid severe reduction in strength. It will be interesting to investigate and optimize magnetostriction and other magnetic properties along with the mechanical behavior of these laser synthesized soft magnetic metallic glass based composite materials.

(3) *Different Metallic Glass Compositions:* From the mechanical behavior point of view, the author suggests investigating laser treatments of other metallic glass compositions which yield softer phases upon crystallization. Examples include $Ti_{40}Zr_{30}Be_{30}$ which forms soft bcc phase dendrites in the amorphous matrix upon crystallization [26], and $Zr_{36.6}Ti_{31.4}Nb_7Cu_{5.9}Be_x$ which forms variable amounts of soft crystalline phase in the amorphous matrix based on Be content [26], and $Zr_{48}Cu_{46}Al_4Co_2$ which interestingly undergoes transformation of B2 CuZr precipitates to martensite through twinning thus inducing ductility via lowered stacking fault energy [176]. Design of laser treatments to evolve the required fraction of soft crystalline phase would provide a rapid structure-property optimization.

(4) *Laser Assisted Additive Manufacturing of Metallic Glass Based Composites:* The long term goal will be to laser additively synthesize metallic glass based composites in various shapes with tailored microstructures with respect to the concerned application.

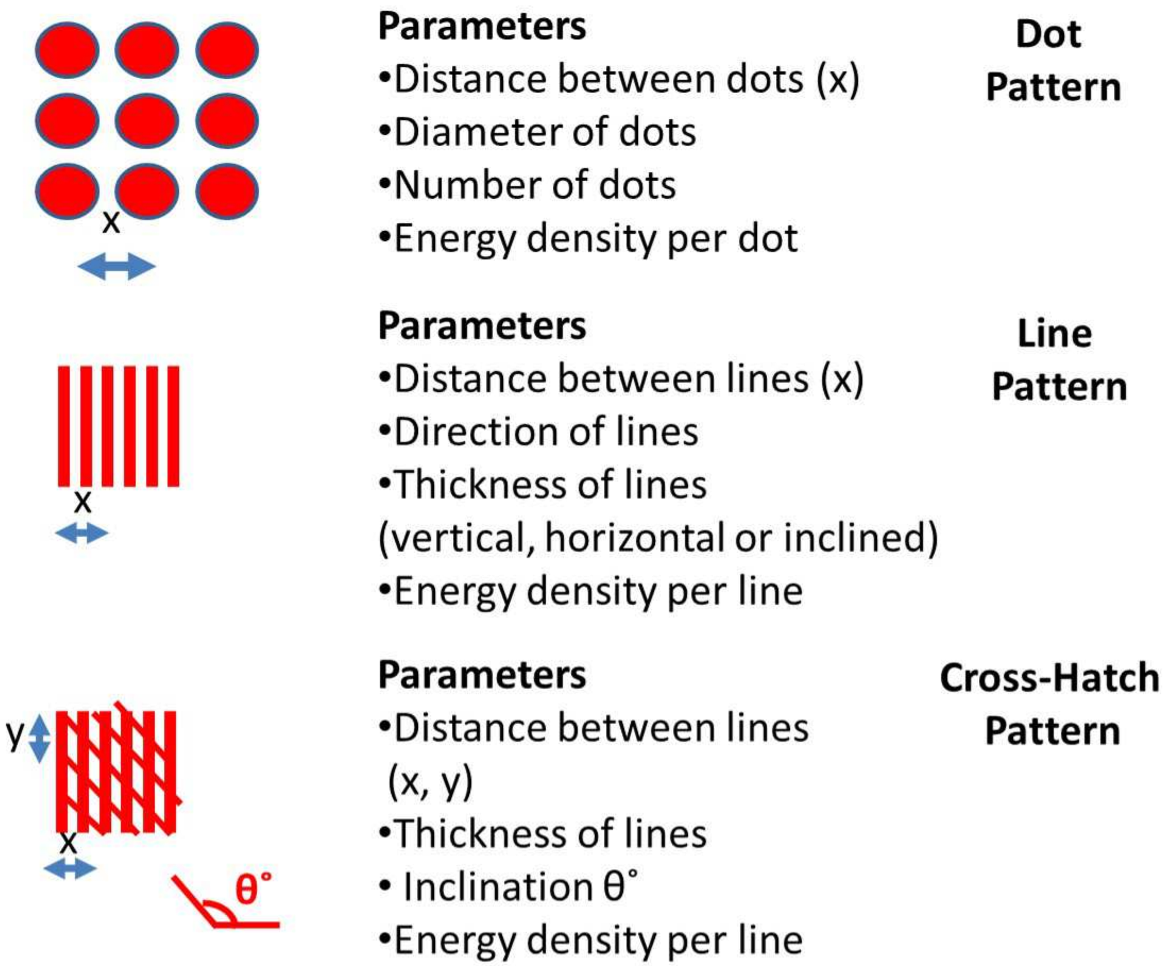

Figure 6.1. Schematic illustrating possible laser patterning treatments of Fe-Si-B metallic glass.

APPENDIX

LIST OF PUBLICATIONS

Related Papers

(1) **Sameehan S. Joshi**, Anna V. Gkriniari, Shravana Katakam, and Narendra B. Dahotre. "Dynamic crystallization during non-isothermal laser treatment of Fe–Si–B metallic glass." Journal of Physics D: Applied Physics 48, no. 49 (2015): 495501.

(2) **Sameehan S. Joshi**, Peyman Samimi, Iman Ghamarian, Shravana Katakam, Peter C. Collins, and Narendra B. Dahotre. "Tensile behavior of laser treated Fe-Si-B metallic glass." Journal of Applied Physics 118, no. 16 (2015): 164904.

(3) **Sameehan S. Joshi**, Jonathan Z. Lu, and Narendra B. Dahotre. "Optimization of laser thermal treatment of Fe–Si–B metallic glass." Journal of Manufacturing Processes 24 (2016): 31-37.

(4) **Sameehan S. Joshi**, Iman Ghamarian, Peyman Samimi, Shravana Katakam, Peter C. Collins, and Narendra B. Dahotre. "Crystallisation behaviour during tensile loading of laser treated Fe–Si–B metallic glass." Philosophical Magazine 97, no. 7 (2017): 497-514.

(5) **Sameehan S. Joshi**, Shravana Katakam, Harpreet Singh Arora, Sundeep Mukherjee, and Narendra B. Dahotre. "Amorphous coatings and surfaces on structural materials." Critical Reviews in Solid State and Materials Sciences 41, no. 1 (2016): 1-46.

Other Papers

(1) Katakam, Shravana, **Sameehan S. Joshi**, Sanghita Mridha, Sundeep Mukherjee, and Narendra B. Dahotre. "Laser assisted high entropy alloy coating on aluminum: Microstructural evolution." Journal of Applied Physics 116, no. 10 (2014): 104906.

(2) Shon, Youkang, **Sameehan S. Joshi**, Shravana Katakam, Ravi Shanker Rajamure, and Narendra B. Dahotre. "Laser additive synthesis of high entropy alloy coating on aluminum: Corrosion behavior." Materials Letters 142 (2015): 122-125.

(3) Alam, Talukder, Tushar Borkar, **Sameehan S. Joshi**, Shravan Katakam, X. Chen, Narendra B. Dahotre, Raju V. Ramanujan, and Rajarshi Banerjee. "Influence of

niobium on laser de-vitrification of Fe–Si–B based amorphous magnetic alloys." Journal of Non-Crystalline Solids 428 (2015): 75-81.

(4) Wu, Tso-Chang, Yee-Hsien Ho, **Sameehan S. Joshi**, Ravi S. Rajamure, and Narendra B. Dahotre. "Microstructure and corrosion behavior of laser surface-treated AZ31B Mg bio-implant material." Lasers in medical science 32, no. 4 (2017): 797-803.

Book Chapter

(1) **Sameehan S. Joshi** and Narendra B. Dahotre, "Laser Surface Engineering for Tribology" in ASM Handbook, Vol. 18: Friction, Lubrication, and Wear Technology, ASM International, Materials Park, OH (2017) (in press at the time of completion of dissertation).

Book

(1) Narendra B. Dahotre, and **Sameehan S. Joshi** "Machining of Bone and Hard Tissues." Springer, Cham Switzerland (2016).

REFERENCES

[1] Shravana Katakam, Arun Devaraj, Mark Bowden, S Santhanakrishnan, Casey Smith, Raju V Ramanujan, Suntharampillai Thevuthasan, Rajarshi Banerjee, and Narendra B Dahotre. Laser assisted crystallization of ferromagnetic amorphous ribbons: A multimodal characterization and thermal model study. *J. Appl. Phys.*, 114(18):184901, 2013.

[2] Mark Telford. The case for bulk metallic glass. *Materials today*, 7(3):36–43, 2004.

[3] AL Greer. Structural relaxation and atomic transport in amorphous alloys. *Rapidly Solidified Alloys, Marcel Dekker, Basel*, page 269, 1993.

[4] C Suryanarayana and Akihisa Inoue. *Bulk metallic glasses.* CRC Press, 2010.

[5] Yi Qun Gao and Wego Wang. On the activation energy of crystallization in metallic glasses. *Journal of non-crystalline solids*, 81(1):129–134, 1986.

[6] Douglas C Hofmann, Jin-Yoo Suh, Aaron Wiest, Mary-Laura Lind, Marios D Demetriou, and William L Johnson. Development of tough, low-density titanium-based bulk metallic glass matrix composites with tensile ductility. *Proceedings of the National Academy of Sciences*, 105(51):20136–20140, 2008.

[7] H Natter, M Schmelzer, M-S Löffler, CE Krill, A Fitch, and R Hempelmann. Grain-growth kinetics of nanocrystalline iron studied in situ by synchrotron real-time X-ray diffraction. *J. Phys. Chem. B*, 104(11):2467–2476, 2000.

[8] AS Argon. Plastic deformation in metallic glasses. *Acta metallurgica*, 27(1):47–58, 1979.

[9] AL Greer, YQ Cheng, and E Ma. Shear bands in metallic glasses. *Mater. Sci. Eng., R*, 74(4):71–132, 2013.

[10] http://tricliniclabs.com/directory/solid-state-development services/. 2015.

[11] http: //www.s-cool.co.uk/category/subjects/a-level/physics/stress-and strain. 2015.

[12] Christopher A Schuh, Todd C Hufnagel, and Upadrasta Ramamurty. Mechanical behavior of amorphous alloys. *Acta Materialia*, 55(12):4067–4109, 2007.

[13] Victor Koledov, Vladimir Shavrov, Alexey Zhikharev, German Martynov, Anna

Palicyna, Alexander Kamansev, Peter Lega, Maria Polupanova, AN Redkin, EE Yakimov, et al. Structure and morphology of the ZnxMg1-x nanowires studied using shape memory composite nano-tweezers. In *Manipulation, Manufacturing and Measurement on the Nanoscale (3M-NANO), 2015 International Conference on*, pages 64–67. IEEE, 2015.

[14] Anass Dakka, Jacques Lafait, Claude Sella, Serge Berthier, Mohammed Abd-Lefdil, Jean-Claude Martin, and Malik Maaza. Optical properties of Ag–TiO_2 nanocermet films prepared by cosputtering and multilayer deposition techniques. *Applied optics*, 39(16):2745–2753, 2000.

[15] William D Callister and David G Rethwisch. *Materials science and engineering*, volume 5. John Wiley & Sons NY, 2011.

[16] JJ Lewandowski and AL Greer. Temperature rise at shear bands in metallic glasses. *Nature Materials*, 5(1):15–18, 2006.

[17] HJ Leamy, TT Wang, and HS Chen. Plastic flow and fracture of metallic glass. *Metallurgical and Materials Transactions B*, 3(3):699–708, 1972.

[18] N Nagendra, U Ramamurty, TT Goh, and Y Li. Effect of crystallinity on the impact toughness of a la-based bulk metallic glass. *Acta Materialia*, 48(10):2603–2615, 2000.

[19] AS Argon and M Salama. The mechanism of fracture in glassy materials capable of some inelastic deformation. *Materials Science and Engineering*, 23(2-3):219–230, 1976.

[20] BA Sun, J Tan, S Pauly, U Kühn, and J Eckert. Stable fracture of a malleable Zr-based bulk metallic glass. *Journal of Applied Physics*, 112(10):103533, 2012.

[21] MF Ashby and AL Greer. Metallic glasses as structural materials. *Scripta Materialia*, 54(3):321–326, 2006.

[22] A Lindsay Greer. Metallic glasses. *Science*, 267(5206):1947, 1995.

[23] Sameehan S Joshi, Shravana Katakam, Harpreet Singh Arora, Sundeep Mukherjee, and Narendra B Dahotre. Amorphous coatings and surfaces on structural materials. *Critical Reviews in Solid State and Materials Sciences*, pages 1–46, 2015.

[24] Tadeusz Kulik. Nanocrystallization of metallic glasses. *Journal of Non-Crystalline*

Solids, 287(1):145–161, 2001.

[25] Douglas C Hofmann, Jin-Yoo Suh, Aaron Wiest, Gang Duan, Mary-Laura Lind, Marios D Demetriou, and William L Johnson. Designing metallic glass matrix composites with high toughness and tensile ductility. *Nature*, 451(7182):1085–1089, 2008.

[26] Douglas Clayton Hofmann. *Designing metallic glass matrix composites with high toughness and tensile ductility*. PhD thesis, California Institute of Technology, 2009.

[27] Shravana K Katakam. *Laser surface treatment of amorphous metals*. PhD thesis, University of North Texas, 2014.

[28] T Kulik, T Horubał, and H Matyja. Flash annealing nanocrystallization of Fe- Si-B-based glasses. *Mat. Sci. Eng.: A*, 157(1):107–112, 1992.

[29] R Nicula, M Stir, K Ishizaki, J-M Català-Civera, and S Vaucher. Rapid nanocrystallization of soft-magnetic amorphous alloys using microwave induction heating. *Scripta Mater.*, 60(2):120–123, 2009.

[30] Shravana Katakam, Jun Y Hwang, Hitesh Vora, Sandip P Harimkar, Rajarshi Banerjee, and Narendra B Dahotre. Laser-induced thermal and spatial nanocrystallization of amorphous Fe–Si–B alloy. *Scripta Mater.*, 66(8):538–541, 2012.

[31] P Murali and U Ramamurty. Embrittlement of a bulk metallic glass due to sub-T_g annealing. *Acta Materialia*, 53(5):1467–1478, 2005.

[32] Sameehan S Joshi, Shravana Katakam, Harpreet Singh Arora, Sundeep Mukherjee, and Narendra B Dahotre. Amorphous coatings and surfaces on structural materials. *Critical Reviews in Solid State and Materials Sciences*, 41(1):1–46, 2016.

[33] W. Klement and R. Willens and P. Duwez. Non-crystalline structure in solidified gold-silicon alloys. *Nature*, 187:869–870, 1960.

[34] Sameehan S Joshi, Shravana Katakam, Harpreet Singh Arora, Sundeep Mukherjee, and Narendra B Dahotre. Amorphous coatings and surfaces on structural materials. *Critical Reviews in Solid State and Materials Sciences*, pages 1–46, 2015.

[35] David Turnbull and Morrel H Cohen. Free-volume model of the amorphous phase:

glass transition. *The Journal of chemical physics*, 34(1):120–125, 1961.

[36] John C Mauro, Yuanzheng Yue, Adam J Ellison, Prabhat K Gupta, and Douglas C Allan. Viscosity of glass-forming liquids. *Proceedings of the National Academy of Sciences*, 106(47):19780–19784, 2009.

[37] Zi-Zhou Yuan, Xue-Ding Chen, Bing-Xia Wang, and Ying-Jun Wang. Kinetics study on non-isothermal crystallization of the metallic Co 43 Fe 20 Ta 5.5 B 31.5 glass. *Journal of Alloys and Compounds*, 407(1):163–169, 2006.

[38] Man Zhu, Junjie Li, Lijuan Yao, Zengyun Jian, Fang'e Chang, and Gencang Yang. Non-isothermal crystallization kinetics and fragility of (Cu 46 Zr 47 Al 7) 97 Ti 3 bulk metallic glass investigated by differential scanning calorimetry. *Thermochimica Acta*, 565:132–136, 2013.

[39] YX Zhuang, PF Xing, HY Shi, J Chen, PW Wang, and JC He. On the heating rate dependence of crystallization temperatures of metallic glasses. *Journal of Applied Physics*, 108(3):033515, 2010.

[40] RB Schwarz and WL Johnson. Formation of an amorphous alloy by solid-state reaction of the pure polycrystalline metals. *Physical Review Letters*, 51(5):415, 1983.

[41] H Schröder, K Samwer, and U Köster. Micromechanism for metallic-glass formation by solid-state reactions. *Physical Review Letters*, 54(3):197, 1985.

[42] Sameehan S Joshi, Anna V Gkriniari, Shravana Katakam, and Narendra B Dahotre. Dynamic crystallization during non-isothermal laser treatment of Fe–Si–B metallic glass. *Journal of Physics D: Applied Physics*, 48(49):495501, 2015.

[43] Shravana Katakam and Narendra Dahotre. Laser patterning of Fe–Si–B amorphous ribbons in magnetic field. *Appl. Phys. A*, 117(3):1241–1247, 2014.

[44] Talukder Alam, Tushar Borkar, Sameehan S Joshi, Shravan Katakam, X Chen, Narendra B Dahotre, Raju V Ramanujan, and Rajarshi Banerjee. Influence of niobium on laser de-vitrification of Fe–Si–B based amorphous magnetic alloys. *Journal of Non-Crystalline Solids*, 428:75–81, 2015.

[45] Atakan Peker and William L Johnson. A highly processable metallic glass: $Zr_{41.2}Ti_{13.8}$

$Cu_{12.5}Ni_{10.0}$ $Be_{22.5}$. *App. Phys. Lett.*, 63(17):2342–2344, 1993.

[46] Alan H Brothers and David C Dunand. Ductile bulk metallic glass foams. *Advanced Materials*, 17(4):484–486, 2005.

[47] KF Yao, F Ruan, YQ Yang, and N Chen. Superductile bulk metallic glass. *Applied Physics Letters*, 88(12):122106, 2006.

[48] T Egami. Structural relaxation in metallic glasses. *Annals of the New York Academy of Sciences*, 371(1):238–251, 1981.

[49] AL Greer. Atomic transport and structural relaxation in metallic glasses. *Journal of non-crystalline solids*, 61:737–748, 1984.

[50] SS Tsao and F Spaepen. Structural relaxation of a metallic glass near equilibrium. *Acta Metallurgica*, 33(5):881–889, 1985.

[51] N Morito and T Egami. Internal friction and reversible structural relaxation in the metallic glass $Fe_{32}Ni_{36}Cr_{14}P_{12}B_6$. *Acta Metallurgica*, 32(4):603–613, 1984.

[52] FE Luborsky. *Amorphous metallic alloys.* Butterworth and Co (Publishers): London, UK, 1983.

[53] HS Chen. The influence of structural relaxation on the density and young's modulus of metallic glasses. *Journal of Applied Physics*, 49(6):3289–3291, 1978.

[54] MG Scott and A Kuršumović. Short-range ordering during structural relaxation of the metallic glass Fe40Ni40B20. *Acta Metallurgica*, 30(4):853–860, 1982.

[55] Minoru Doi, Toshihiro Hanamura, Masaaki Matsui, and Toru Imura. Electric resistivity and cyclic deformation of liquid-quenched Fe-based and Co-based amorphous alloys. *Jpn. J. Appl. Phys.*, 19(3):449, 1980.

[56] KF Kelton and F Spaepen. Kinetics of structural relaxation in several metallic glasses observed by changes in electrical resistivity. *Physical Review B*, 30(10):5516, 1984.

[57] Raj Banerjee. Phase transformations in materials: Lecture notes. *Lecture 5*, 2014.

[58] David A Porter, Kenneth E Easterling, and Mohamed Sherif. *Phase Transformations in Metals and Alloys, (Revised Reprint).* CRC press, 2011.

[59] U Köster and U Herold. Crystallization of metallic glasses. *Glassy metals I*, pages

225–259, 1981.

[60] Uwe Köster and Jürgen Meinhardt. Crystallization of highly undercooled metallic melts and metallic glasses around the glass transition temperature. *Materials Science and Engineering: A*, 178(1-2):271–278, 1994.

[61] Casey Smith, Shravana Katakam, Soumya Nag, Xi Chen, Raju V Ramanujan, Narendra B Dahotre, and Rajarshi Banerjee. Improved soft magnetic properties by laser de-vitrification of Fe–Si–B amorphous magnetic alloys. *Mater. Lett.*, 122:155–158, 2014.

[62] Andrew J Detor and Christopher A Schuh. Tailoring and patterning the grain size of nanocrystalline alloys. *Acta Mater.*, 55(1):371–379, 2007.

[63] Giselher Herzer. Nanocrystalline soft magnetic materials. *Phys. Scripta*, 1993(T49A):307, 1993.

[64] Gerhard Wilde. *26 - Physical Metallurgy of Nanocrystalline Metals*. Elsevier, Oxford, fifth edition edition, 2014.

[65] C Suryanarayana. Nanocrystalline materials. *Int. Mater. Rev.*, 40(2):41–64, 1995.

[66] T Kulik, D Bucka, and H Matyja. Effect of flash annealing on the grain size and morphology of crystallization products of Co-Si-B glasses. *Journal of materials science letters*, 12(2):76–79, 1993.

[67] IV Okulov, IV Soldatov, MF Sarmanova, I Kaban, T Gemming, Kristina Edström, and J Eckert. Flash joule heating for ductilization of metallic glasses. *Nature communications*, 6, 2015.

[68] GL Whittle, A Calka, AP Radliński, and B Luther-Davies. Ultra short pulse laser annealing of FeB metallic glasses. *Journal of magnetism and magnetic materials*, 50(3):278–286, 1985.

[69] TR Malow and CC Koch. Grain growth in nanocrystalline iron prepared by mechanical attrition. *Acta Mater.*, 45(5):2177–2186, 1997.

[70] XY Jiang, ZC Zhong, and AL Greer. Particle-size effects in primary crystallization of amorphous Al-Ni-Y alloys. *Mat. Sci. Eng.: A*, 226:789–793, 1997.

[71] Casey Smith, Shravana Katakam, Soumya Nag, Xi Chen, Raju V Ramanujan, Narendra B Dahotre, and Rajarshi Banerjee. Improved soft magnetic properties by laser de-vitrification of Fe–Si–B amorphous magnetic alloys. *Mater. Lett.*, 122:155–158, 2014.

[72] M Gibbs, D-H Lee, and JEBC Evetts. Dc magnetic properties of metallic glasses after flash annealing. *IEEE transactions on magnetics*, 20(5):1373–1375, 1984.

[73] H Ma, J Xu, and E Ma. Mg-based bulk metallic glass composites with plasticity and high strength. *Applied physics letters*, 83(14):2793–2795, 2003.

[74] Ying-Kun Xu, Han Ma, Jian Xu, and En Ma. Mg-based bulk metallic glass composites with plasticity and gigapascal strength. *Acta Materialia*, 53(6):1857–1866, 2005.

[75] BE Schuster, Q Wei, TC Hufnagel, and KT Ramesh. Size-independent strength and deformation mode in compression of a Pd-based metallic glass. *Acta Materialia*, 56(18):5091–5100, 2008.

[76] J Eckert, J Das, KB Kim, F Baier, MB Tang, WH Wang, and ZF Zhang. High strength ductile cu-base metallic glass. *Intermetallics*, 14(8):876–881, 2006.

[77] Y He, GM Dougherty, GJ Shiflet, and SJ Poon. Unique metallic glass formability and ultra-high tensile strength in AlNiFeGd alloys. *Acta metallurgica et materialia*, 41(2):337–343, 1993.

[78] JH Yao, JQ Wang, and Yi Li. Ductile Fe–Nb–B bulk metallic glass with ultrahigh strength. *Applied Physics Letters*, 92(25):251906, 2008.

[79] Egon Orowan. Fracture and strength of solids. *Reports on progress in physics*, 12(1):185, 1949.

[80] WR Tyson. Theoretical strength of perfect crystals. *Philosophical magazine*, 14(131):925–936, 1966.

[81] Michael L Falk and James S Langer. Dynamics of viscoplastic deformation in amorphous solids. *Physical Review E*, 57(6):7192, 1998.

[82] Jun Yi, S Mohsen Seifi, Weihua Wang, and John J Lewandowski. A damage-tolerant bulk metallic glass at liquid-nitrogen temperature. *J. Mater. Sci. Technol.*,

30(6):627–630, 2014.

[83] Sandip P Harimkar, Sameer R Paital, Gangyao Wang, Peter K Liaw, and Narendra B Dahotre. Periodically laser patterned fe-b-si amorphous ribbons: Phase evolution and mechanical behavior. *Advanced Engineering Materials*, 13(10):955–960, 2011.

[84] J-J Kim, Y Choi, S Suresh, and AS Argon. Nanocrystallization during nanoindentation of a bulk amorphous metal alloy at room temperature. *Science*, 295(5555):654–657, 2002.

[85] YQ Cheng, Z Han, Y Li, and E Ma. Cold versus hot shear banding in bulk metallic glass. *Physical Review B*, 80(13):134115, 2009.

[86] Bing Yang, Mark L Morrison, Peter K Liaw, Raymond A Buchanan, Gongyao Wang, Chain T Liu, and Mitsunori Denda. Dynamic evolution of nanoscale shear bands in a bulk-metallic glass. *Applied Physics Letters*, 86(14):141904, 2005.

[87] Frans Spaepen. A microscopic mechanism for steady state inhomogeneous flow in metallic glasses. *Acta metallurgica*, 25(4):407–415, 1977.

[88] DTA Matthews, V Ocelik, PM Bronsveld, and J Th M De Hosson. An electron microscopy appraisal of tensile fracture in metallic glasses. *Acta Materialia*, 56(8):1762–1773, 2008.

[89] Michael C Gao, Robert E Hackenberg, and Gary J Shiflet. Deformation-induced nanocrystal precipitation in al-base metallic glasses. *Materials Transactions*, 42(8):1741–1747, 2001.

[90] P Rizzi and L Battezzati. Mechanical properties of al based amorphous and devitrified alloys containing different rare earth elements. *Journal of Non-crystalline Solids*, 344(1):94–100, 2004.

[91] Ajay Gupta. Nanocrystalline soft-magnetic alloys produced by controlled crystallization of amorphous alloys. *Proceedings-Indian National Science Academy Part A*, 67(1):31–46, 2001.

[92] Akihiro Makino, Takeshi Kubota, Chuntao Chang, Masahiro Makabe, and Akihisa Inoue. Fesibp bulk metallic glasses with high magnetization and excellent magnetic

softness. *J. Magn. Magn. Mater.*, 320(20):2499–2503, 2008.

[93] JC Foley, DR Allen, and JH Perepezko. Strategies for the development of nanocrystalline materials through devitrification. *Mater. Sci. Engg., A*, 226:569–573, 1997.

[94] Shravana Katakam, S Santhanakrishnan, Hitesh Vora, Jun Y Hwang, Rajarshi Banerjee, and Narendra B Dahotre. Stress-induced selective nano-crystallization in laser-processed amorphous Fe–Si–B alloys. *Philosophical Magazine Letters*, 92(11):617–624, 2012.

[95] Eric W Lee. Magnetostriction and magnetomechanical effects. *Reports on progress in physics*, 18(1):184, 1955.

[96] Giselher Herzer. Modern soft magnets: amorphous and nanocrystalline materials. *Acta Materialia*, 61(3):718–734, 2013.

[97] Paola Tiberto, Marcello Baricco, Elena Olivetti, and Rafael Piccin. Magnetic properties of bulk metallic glasses. *Advanced Engineering Materials*, 9(6):468–474, 2007.

[98] Ana C de AZEVEDO, AC Delaiba, José C de OLIVEIRA, BC Carvalho, and H de S Bronzeado. Transformer mechanical stress caused by external short-circuit: a time domain approach. In *International Conference on Power Systems Transients, Lyon France*, 2007.

[99] E Billig. Mechanical stresses in transformer windings. *Electrical Engineers-Part II: Power Engineering, Journal of the Institution of*, 93(33):227–243, 1946.

[100] M Wang, AJ Vandermaar, and K D_ Srivastava. Review of condition assessment of power transformers in service. *Electrical Insulation Magazine, IEEE*, 18(6):12–25, 2002.

[101] http://www·metglas·com/faq/?cat=Alloys. 2015.

[102] Brian C Sales, Olivier Delaire, Michael A McGuire, and Andrew F May. Thermoelectric properties of Co-, Ir-, and Os- doped FeSi alloys: Evidence for strong electron-phonon coupling. *Phys. Rev. B*, 83(12):125209, 2011.

[103] L Costa, R Vilar, T Reti, and AM Deus. Rapid tooling by laser powder deposition:

Process simulation using finite element analysis. *Acta Mater.*, 53(14):3987–3999, 2005.

[104] George E Totten and Maurice AH Howes. *Steel heat treatment handbook.* CRC Press, 1997.

[105] Soundarapandian Santhanakrishnan, Fanrong Kong, and Radovan Kovacevic. An experimentally based thermo-kinetic hardening model for high power direct diode laser cladding. *J. Mater. Process Tech.*, 211(7):1247–1259, 2011.

[106] Elijah Kannatey-Asibu Jr. *Principles of laser materials processing*, volume 4. John Wiley & Sons, 2009.

[107] Shravana Katakam. *Laser Surface Treatment of Amorphous Metals.* PhD thesis, University of North Texas, 2014.

[108] Ke Lu. Nanocrystalline metals crystallized from amorphous solids: nanocrystallization, structure, and properties. *Mat. Sci. Eng.: R*, 16(4):161–221, 1996.

[109] Iman Ghamarian, Yue Liu, Peyman Samimi, and Peter C Collins. Development and application of a novel precession electron diffraction technique to quantify and map deformation structures in highly deformed materials-as applied to ultrafine-grained titanium. *Acta Materialia*, 79:203–215, 2014.

[110] RC Hugo, H Kung, JR Weertman, R Mitra, JA Knapp, and DM Follstaedt. In-situ tem tensile testing of dc magnetron sputtered and pulsed laser deposited ni thin films. *Acta Materialia*, 51(7):1937–1943, 2003.

[111] M Jin, AM Minor, EA Stach, and JW Morris. Direct observation of deformation-induced grain growth during the nanoindentation of ultrafine-grained Al at room temperature. *Acta Materialia*, 52(18):5381–5387, 2004.

[112] YH Zhao, YT Zhu, XZ Liao, Z Horita, and TG Langdon. Tailoring stacking fault energy for high ductility and high strength in ultrafine grained cu and its alloy. *Applied physics letters*, 89(12):121906, 2006.

[113] Paul Scherrer. Bestimmung der inneren struktur und der größe von kolloidteilchen mittels röntgenstrahlen. In *Kolloidchemie Ein Lehrbuch*, pages 387–409. Springer, 1912.

[114] TR Malow, CC Koch, PQ Miraglia, and KL Murty. Compressive mechanical behavior of nanocrystalline Fe investigated with an automated ball indentation technique. *Materials Science and Engineering: A*, 252(1):36–43, 1998.

[115] Holger Borchert, Elena V Shevchenko, Aymeric Robert, Ivo Mekis, Andreas Kornowski, Gerhard Grübel, and Horst Weller. Determination of nanocrystal sizes: a comparison of TEM, SAXS, and XRD studies of highly monodisperse $CoPt_3$ particles. *Langmuir*, 21(5):1931–1936, 2005.

[116] Alicia Weibel, Renaud Bouchet, F Boulc', and Philippe Knauth. The big problem of small particles: a comparison of methods for determination of particle size in nanocrystalline anatase powders. *Chemistry of materials*, 17(9):2378–2385, 2005.

[117] Atul Sharma, Takashi Kyotani, and Akira Tomita. Comparison of structural parameters of pf carbon from xrd and hrtem techniques. *Carbon*, 38(14):1977–1984, 2000.

[118] Hao-Ying Lu, Sheng-Yuan Chu, and Soon-Seng Tan. The characteristics of low-temperature-synthesized zns and zno nanoparticles. *Journal of Crystal growth*, 269(2):385–391, 2004.

[119] Alicja Załuska and Henryk Matyja. Crystallization characteristics of amorphous Fe-Si-B alloys. *J. Mater. Sci.*, 18(7):2163–2172, 1983.

[120] AP Wang, XC Chang, WL Hou, and JQ Wang. Preparation and corrosion behaviour of amorphous ni-based alloy coatings. *Mat. Sci. Eng.: A*, 449:277–280, 2007.

[121] Min Tao. *High temperature deformation of Vitreloy bulk metallic glasses and their composite*. PhD thesis, California Institute of Technology, 2006.

[122] ASM Handbook - Alloy phase diagrams, vol. 3, 1992.

[123] XY Jiang, ZC Zhong, and AL Greer. Particle-size effects in primary crystallization of amorphous Al-Ni-Y alloys. *Mat. Sci. Eng.: A*, 226:789–793, 1997.

[124] Y. X. Zhuang, P. F. Xing, H. Y. Shi, J. Chen, P. W. Wang, and J. C. He. On the heating rate dependence of crystallization temperatures of metallic glasses. *J. Appl. Phys.*, 108(3):–, 2010.

[125] K Matusita and S Sakka. Kinetic study of the crystallization of glass by differential scanning calorimetry. *Phys. Chem. Glasses*, 20(4):81, 1979.

[126] Homer E Kissinger. Reaction kinetics in differential thermal analysis. *Analytical chemistry*, 29(11):1702–1706, 1957.

[127] Tadeusz Kulik. Nanocrystallization of metallic glasses. *J. Non-Cryst. Solids*, 287(1):145–161, 2001.

[128] S.F. Guo, L. Liu, N. Li, and Y. Li. Fe-based bulk metallic glass matrix composite with large plasticity. *Scripta Mater.*, 62(6):329 – 332, 2010.

[129] DH Kim, WT Kim, ES Park, N Mattern, and J Eckert. Phase separation in metallic glasses. *Prog. Mater Sci.*, 58(8):1103–1172, 2013.

[130] T Egami. Structural relaxation in metallic glasses. *Ann. N.Y. Acad. Sci.*, 371(1):238–251, 1981.

[131] EP Donovan, F Spaepen, D Turnbull, JM Poate, and DC Jacobson. Calorimetric studies of crystallization and relaxation of amorphous Si and Ge prepared by ion implantation. *J. Appl. Phys.*, 57(6):1795–1804, 1985.

[132] Gregor Diezemann. A free-energy landscape model for primary relaxation in glass-forming liquids: Rotations and dynamic heterogeneities. *J. Chem. Phys.*, 107(23), 1997.

[133] Komatsu T. Structural relaxation and related processes in metallic glasses. *Res. Mechanica*, 31(3):263, 1990.

[134] E Jakubczyk, A Krajczyk, and M Jakubczyk. Crystallization of amorphous $Fe_{78}Si_9B_{13}$ alloy. *J. Phys.: Conference Series*, 79(1):012008, 2007.

[135] JC Oh, T Ohkubo, YC Kim, E Fleury, and K Hono. Phase separation in Cu 43 Zr 43 Al 7 Ag 7 bulk metallic glass. *Scripta Materialia*, 53(2):165–169, 2005.

[136] KF Kelton, TK Croat, AK Gangopadhyay, L-Q Xing, AL Greer, M Weyland, X Li, and K Rajan. Mechanisms for nanocrystal formation in metallic glasses. *Journal of non-crystalline solids*, 317(1):71–77, 2003.

[137] KF Kelton. A new model for nucleation in bulk metallic glasses. *Philosophical magazine*

letters, 77(6):337–344, 1998.

[138] X-L Wang, J Almer, CT Liu, YD Wang, JK Zhao, AD Stoica, DR Haeffner, and WH Wang. In situ synchrotron study of phase transformation behaviors in bulk metallic glass by simultaneous diffraction and small angle scattering. *Physical review letters*, 91(26):265501, 2003.

[139] Hitesh D Vora, Ravi Shanker Rajamure, Santhanakrishnan Soundarapandian, SG Srinivasan, and Narendra B Dahotre. Design and optimization of microstructure for improved corrosion resistance in laser surface alloyed aluminum with molybdenum. *Int. J. Precis. Eng. Man.*, 14(8):1421–1432, 2013.

[140] Mark J Anderson and Patrick J Whitcomb. *DOE simplified: practical tools for effective experimentation.* CRC Press, Boca Raton, FL, USA, 2015.

[141] George C Derringer. A balancing act-optimizing a products properties. *Quality Progress*, 27(6):51–58, 1994.

[142] Nuno R Costa, João Lourenço, and Zulema L Pereira. Desirability function approach: a review and performance evaluation in adverse conditions. *Chemometrics and Intelligent Laboratory Systems*, 107(2):234–244, 2011.

[143] Raymond H Myers, Douglas C Montgomery, and Christine M Anderson-Cook. *Response surface methodology: process and product optimization using designed experiments.* John Wiley & Sons, New Jersey, 2016.

[144] C Suryanarayana and Akihisa Inoue. *Bulk metallic glasses.* CRC Press, 2010.

[145] GR Speich, AJ Schwoeble, and Wo C Leslie. Elastic constants of binary iron-base alloys. *Met. Trans.*, 3(8):2031–2037, 1972.

[146] B Xiao, JD Xing, J Feng, CT Zhou, YF Li, W Su, XJ Xie, and YH Cheng. A comparative study of Cr_7C_3, Fe_3C and Fe_2B in cast iron both from ab initio calculations and experiments. *J. Phys. D: Appl. Phys.*, 42(11):115415, 2009.

[147] C Suryanarayana and A Inoue. Iron-based bulk metallic glasses. *Int. Mater. Rev.*, 58(3):131–166, 2013.

[148] BA Sun and WH Wang. The fracture of bulk metallic glasses. *Progress in Materials*

Science, 74:211–307, 2015.

[149] XK Xi, DQ Zhao, MX Pan, WH Wang, Yue Wu, and JJ Lewandowski. Fracture of brittle metallic glasses: brittleness or plasticity. *Physical review letters*, 94(12):125510, 2005.

[150] Sameehan S Joshi, Peyman Samimi, Iman Ghamarian, Shravana Katakam, Peter C Collins, and Narendra B Dahotre. Tensile behavior of laser treated Fe–Si–B metallic glass. *J. Appl. Phys.*, 118(16):164904, 2015.

[151] T Egami. Structural relaxation in amorphous alloys-compositional short range ordering. *Materials Research Bulletin*, 13(6):557–562, 1978.

[152] U Ramamurty, ML Lee, J Basu, and Y Li. Embrittlement of a bulk metallic glass due to low-temperature annealing. *Scripta Materialia*, 47(2):107–111, 2002.

[153] G Kumar, D Rector, RD Conner, and J Schroers. Embrittlement of Zr-based bulk metallic glasses. *Acta Materialia*, 57(12):3572–3583, 2009.

[154] Chris H Rycroft and Eran Bouchbinder. Fracture toughness of metallic glasses: annealing-induced embrittlement. *Physical review letters*, 109(19):194301, 2012.

[155] A Concustell, G Alcala, S Mato, TG Woodcock, A Gebert, J Eckert, and MD Baró. Effect of relaxation and primary nanocrystallization on the mechanical properties of Cu 60 Zr 22 Ti 18 bulk metallic glass. *Intermetallics*, 13(11):1214–1219, 2005.

[156] Weidong Li, Yanfei Gao, and Hongbin Bei. On the correlation between microscopic structural heterogeneity and embrittlement behavior in metallic glasses. *Scientific reports*, 5:14786, 2015.

[157] D Szewieczek, J Tyrlik-Held, and S Lesz. Changes of mechanical properties and fracture morphology of amorphous tapes involved by heat treatment. *J. Mater. Process. Technol.*, 109(1):190–195, 2001.

[158] CA Pampillo and DE Polk. The strength and fracture characteristics of Fe, Ni-Fe and Ni-base glasses at various temperatures. *Acta Metallurgica*, 22(6):741–749, 1974.

[159] F Sansoz and V Dupont. Grain growth behavior at absolute zero during nanocrystalline metal indentation. *Applied physics letters*, 89(11):111901, 2006.

[160] IA Ovid'ko, AG Sheinerman, and EC Aifantis. Stress-driven migration of grain boundaries and fracture processes in nanocrystalline ceramics and metals. *Acta Materialia*, 56(12):2718–2727, 2008.

[161] Sandeep Kumar, Tarek Alam, and Aman Haque. Quantitative in-situ tem study of stress-assisted grain growth. *MRS Communications*, 3(02):101–105, 2013.

[162] Marc Legros, Daniel S Gianola, and Kevin J Hemker. In situ tem observations of fast grain-boundary motion in stressed nanocrystalline aluminum films. *Acta Materialia*, 56(14):3380–3393, 2008.

[163] Weichang Xu, Pinqiang Dai, and Xiaolei Wu. Effect of stress-induced grain growth during room temperature tensile deformation on ductility in nanocrystalline metals. *Bulletin of Materials Science*, 33(5):561–568, 2010.

[164] GJ Fan, LF Fu, DC Qiao, H Choo, PK Liaw, and ND Browning. Grain growth in a bulk nanocrystalline co alloy during tensile plastic deformation. *Scripta materialia*, 54(12):2137–2141, 2006.

[165] Ravi S Kottada and Atul H Chokshi. Low temperature compressive creep in electrodeposited nanocrystalline nickel. *Scripta materialia*, 53(8):887–892, 2005.

[166] MJNV Prasad and AH Chokshi. Deformation-induced thermally activated grain growth in nanocrystalline nickel. *Scripta Materialia*, 67(2):133–136, 2012.

[167] DB Miracle, A Concustell, Y Zhang, AR Yavari, and AL Greer. Shear bands in metallic glasses: Size effects on thermal profiles. *Acta Materialia*, 59(7):2831–2840, 2011.

[168] KS Kumar, H Van Swygenhoven, and S Suresh. Mechanical behavior of nanocrystalline metals and alloys. *Acta Materialia*, 51(19):5743–5774, 2003.

[169] D Jia, KT Ramesh, and E Ma. Effects of nanocrystalline and ultrafine grain sizes on constitutive behavior and shear bands in iron. *Acta Materialia*, 51(12):3495–3509, 2003.

[170] Raymond E Smallman and Ray J Bishop. *Modern Physical Metallurgy and Materials Engineering*. Butterworth-Heinemann, 1999.

[171] Takashi Mizuguchi, Kento Ikeda, and Naoki Karasawa. Effects of temperature and

strain rate on deformation twinning in Fe–Si alloy. *ISIJ International*, 55(7):1496–1501, 2015.

[172] Helmut Mehrer. *Diffusion in solids: fundamentals, methods, materials, diffusion-controlled processes*, volume 155. Springer Science & Business Media, Berlin, 2007.

[173] Todd C Hufnagel, Uday K Vempati, and Jonathan D Almer. Crack-tip strain field mapping and the toughness of metallic glasses. *PloS one*, 8(12):e83289, 2013.

[174] Sameehan S Joshi, Jonathan Z Lu, and Narendra B Dahotre. Optimization of laser thermal treatment of Fe–Si–B metallic glass. *Journal of Manufacturing Processes*, 24:31–37, 2016.

[175] Sameehan S Joshi, Iman Ghamarian, Peyman Samimi, Shravana Katakam, Peter C Collins, and Narendra B Dahotre. Crystallisation behaviour during tensile loading of laser treated Fe–Si–B metallic glass. *Philosophical Magazine*, 97(7):497–514, 2017.

[176] Y Wu, DQ Zhou, WL Song, H Wang, ZY Zhang, D Ma, XL Wang, and ZP Lu. Ductilizing bulk metallic glass composite by tailoring stacking fault energy. *Physical review letters*, 109(24):245506, 2012.